PhD Thesis

Ocean Velocities as Inferred from Argo Floats: Methodology and Applications

Miquel Rosell-Fieschi

Institut de Ciències del Mar, CSIC

May 28, 2014

Ocean Velocities as Inferred from Argo Floats: Methodology and Applications

Miquel Rosell-Fieschi

Institut de Ciències del Mar, CSIC

Dissertation submitted to the Universitat Politècnica de Catalunya as a requirement for the Doctoral degree. Speciality: Marine Sciences

Advised by Dr. Josep Lluís Pelegrí i Llopart and Dr. Jerôme Gourrion

Cover: Miquel Rosell-Fieschi

Barcelona May 28, 2014

Dedico questo lavoro al nonno Roberto, che risveglià da bambino la mia curiosità scientífica, essendo in gran parte responsabile del mio fascino per la scoperta.

"...l'arte di scriver storie sta nel saper tirar fuori
da quel nulla che si è capito della vita tutto il resto;
ma finita la pagina si riprende la vita e ci s'accorge
che quel che si sapeva è proprio un nulla."
(Italo Calvino, il Cavaliere Inestistente)

Contents

List of Figures

List of Tables

Preface

The present work has been developed in the frame of the MOC2 project (Ocean Climate Memory: fluxes of intermediate waters in the Southern Atlantic and their transformation into surface waters in the equatorial Atlantic, reference number CTM2008-06438), which was carried out between January 2009 and December 2011 with funding from the Ministerio de Educación y Ciencia of the Spanish Government. The project consisted of two subprojects, being the present PhD thesis part of the first subproject: Ocean Climate Memory: mechanisms and paths of surface water formation in the equatorial Atlantic (reference number CTM2008-06438-C02-01). The main objective of this subproject was to study the processes and velocity of incorporation of the Intermediate Waters towards the superficial ocean in the equatorial Atlantic. The project was funded by the Spanish Government, and carried out at the Physical Oceanography Department of the ICM-CSIC (Institut de Ciències del Mar de Barcelona). Josep Lluís Pelegrí was the project coordinator and PI of the first subproject. He and Jerome Gourrion are the directors of this PhD thesis.

The original aim of this PhD thesis was to explore and develop a novel method to study the paths and rates of transformation of Antarctic Intermediate Water (AAIW) in the equatorial Atlantic Ocean by using the information contained in the floats of the Argo program. In particular, the ocean velocities at the sea surface and the parking depth are inferred from the Argo float trajectories; when combined with the salinity and temperature data, this gives information not only on the paths of the water parcels but also on their transformations. During the last years other authors have explored how to extract the velocity field from the Argo float trajectories and have produced velocity data sets that are regularly updated. Having our own method, however, lets us to control the parameters required by the method to produce the velocity fields, hence allowing us to carry numerous sensitivity studies. Other advantages

are the generation of the velocity fields with all the available Argo data and the possibility of setting particular configurations of the method for regional studies. Finally, future tests and developments of the method can be planned and executed with relatively minor efforts. In this dissertation the method is first presented, and it is later used to examine the statistics of the ocean horizontal velocities and to explore the dynamics of the currents south of Australia and in the equatorial Atlantic Ocean. The dissertation ends up with a description of several ongoing developments that should lead to a future improvement of the method and its applications.

Acronyms List

AAIW : Antarctic Intermediate Water

AABW : Antarctic Bottom Water

sAMW : Subantarctic Mode Water

ACC : Antarctic Circumpolar Current

ADCP : Acoustic Doppler Current Profiler

CLT : central limit theorem

CSIC : Consejo Superior de Investigaciones Científicas

CSIRO : Commonwealth Scientific and Industrial Research Organization

CW : central waters

DAC : Data Acquisition Centre

DWBC : Deep Western Boundary Current

EAC : East Australian Current

EDJ : Equatorial Deep Jets

EEJ : Extra Equatorial Jets

EIC : Equatorial Intermediate Current

EUC : Equatorial Under Current

FC : Flinders Current

GAB : Great Australian Bight

GDAC : Global Data Acquisition Centre

GOC : Global Overturning Circulation

GODAE : Global Data Assimilation Experiment

ICM : Institut de Ciències del Mar

ITCZ : Inter Tropical Convergence Zone

LADCP : Lowered Acoustic Doppler Current Profiler

ME : maximum entropy

MLD : Mixed Layer Depth

MOC : Meridional Overturning Circulation

NADW : North Atlantic Deep Water

NBC : North Brazil Current

NBUC : North Brazil Under Current

NECC : North Equatorial Counter Current

NEIC : North Equatorial Intermediate Current

NEUC : North Equatorial Under Current

NICC : Northern Intermediate Counter Current

uNADW : Upper North Atlantic Deep Water

PDF : probability density function

SEC : South Equatorial Current

sSEC : South South Equatorial Current

cSEC : Central South Equatorial Current

eSEC : Equatorial South Equatorial Current

nSEC : North South Equatorial Current

SEIC : South Equatorial Intermediate Current

SEUC : South Equatorial Under Current

SICC : Southern Intermediate Counter Current

Sv : Sverdrup (10^6 m^3 s^{-1})

TL : Tasman Leakage

WMO : World Meteorological Organization

WOCE : World Ocean Circulation Experiment

ZC : Zeehan Current

Chapter 1

Introduction

1.1 The Argo program

The Argo program started in the early 2000s with the objective of real-time monitoring the upper oceans of the planet. The goal was to set a global array of 3000 simultaneous profiling floats, implying a mean distance between floats of about 3°. The aim was achieved in November 2007 and the array has been maintained since by deploying approximately 800 floats per year to replace the old ones (Fig. 1.1). A float has an average life of approximately 3.3 years. The global array provides over 100,000 CTD profiles and velocity measurements per year.

The Argo program was set to monitor the upper and intermediate ocean. The name Argo reflects the strong complementarity of the global float array with the altimetry satellite called Jason, by recalling the Greek myth where Jason sailed a ship called Argo seeking for the golden fleece. Both datasets (Argo and Jason altimetry data) are being assimilated into computer models developed by the project GODAE (Global Data Assimilation Experiment), allowing to improve our weather and climate forecast.

The Argo objectives, as drawn from the Coriolis Global Data Acquisition Centre (GDAC), are as follows:

- It will provide a quantitative description of the changing state of the upper ocean and the patterns of ocean climate variability from months to decades, including heat and freshwater storage and transport.
- The data will enhance the value of the Jason altimeter through measurement of subsurface temperature, salinity, and velocity, with sufficient coverage and resolution to permit interpretation of altimetric sea surface height variability.
- Argo data will be used for initializing ocean and coupled ocean-atmosphere forecast models, for data assimilation and for model testing.
- A primary focus of Argo is to document seasonal to decadal climate variability and to aid

our understanding of its predictability. A wide range of applications for high-quality global ocean analyses is anticipated.

Figure 1.1: Argo floats distribution for the 8th of February 2014, 3616 active floats.

1.2 Argo velocities

One principal aim of the Argo program was to provide an extensive array of conductivity-temperature-depth (CTD) data to monitor the upper ocean and improve the meteorological forecasts. This CTD data set has proven great potential to determine the current state of the ocean, as shown by numerous studies (Roemmich et al., 2009; Souza et al., 2011; Dong et al., 2008; Sokolov et al., 2009). However, the floats array also provides secondary data that have been less explored. The trajectory data provides all the consecutive positions registered by the float during its lifetime. This positioning data can be used to reconstruct the velocity of the float during the displacement from one point to another.

Several previous studies have used Argo float trajectories to infer current velocities (Davis, 1998; Schmid et al., 2001; Park et al., 2005; Nuñez-Riboni et al., 2005; Ollitrault et al., 2006; Lankhorst, 2009). Lebedev et al. (2007) were the first to release a complete dataset: YoMaHa'07. This dataset is regularly updated and it is now possible to have quasi real time data; this was not the case when the dataset was first released.

More recently, Ollitrault et al. (2013) have released a complete dataset (ANDRO2013) which contains data up to 2010. ANDRO2013 is a very accurate database, where the data has been reconstructed from the row files, correcting some decoding and data errors. There are two main differences between YoMaHa'07 and ANDRO2013:

- Almost 10% of the parking pressures in YoMaHa'07 differ from those of ANDRO2013. This is due to erroneous parking depths in the meta-

files or from floats that do not stabilize at their nominal parking depths.
- YoMaHa'07 calculates a single surface velocity vector for each cycle, whilst ANDRO2013 splits the 12h surface displacement into two 6h displacements and calculates two surface velocity vectors for each cycle.

One first question might be why to put a considerable effort in developing a method that has already been explored and applied by others? At the time when this thesis began the only publically available dataset was YoMaHa'07. It contained a first complete description of the available velocity data and the actual velocity vectors inferred from the Argo trajectories, but did not release the actual method to calculate the velocities. This was a limitation due to the impossibility of a continuous update in a context where the global Argo array provides over 100,000 profiles (and the corresponding velocity vectors) per year. Developing an independent method to estimate the velocities inferred from the Argo floats' trajectory would have given us the chance of a more flexible database –allowing, for example, to decide how to process the data and which values to keep or neglect- and the opportunity of a continuous update.

The task to generate an ocean velocity dataset has proven to be far more complicated than initially expected, but it has also proven to be an effective way to achieve the full availability of the latest velocity data and thus be able to increase the data density to generate more consistent velocity fields, with a higher resolution. We have been able to continuously update our own dataset, and use it to study different ocean regions, as well as for the analysis of the statistical distribution of ocean velocities.

The present thesis does not pretend to replace any of the database that have been released by other research groups, but rather to develop a simple and controlled way to be able to work with all the available data, without the necessity of waiting for the data to be processed by others and being able to intervene in the generation and analysis of the velocity vectors.

1.3 Structure of the manuscript

This thesis aims at releasing a simple method that may be useful to other researchers willing to use, at any time, all available Argo data in order to infer the velocity fields at the floats' parking depths and the sea surface. The power of the

method is illustrated by generating the velocity fields worldwide and for several regional applications.

The second chapter of this thesis is dedicated to explain the method used to infer the velocities from the Argo trajectories. It addresses the error sources intrinsic in the method as well as the limitations in generating the velocity fields. A critical comparison with the methodology developed by other authors allows assessing the goodness and limitations of the method.

In the third chapter the statistics of the velocity fields are examined. During the development of this thesis several questions about the velocities distribution arose: How many individual velocity vectors do we need to produce a reliable mean value? Can we assume the velocity components to follow a Gaussian distribution? Which threshold should be considered to eliminate high spurious velocities? The non-Gaussian distribution of the ocean velocities, the high kurtosis and the long tails have some implications that are important to be taken into account when generating mean velocity fields.

The fourth chapter focuses on the application of the method to the equatorial Atlantic Ocean, generating annual mean velocity fields at all depths where the profiler's density allows to do so (surface, 200 dbar, 1000 dbar and 1500 dbar), and studying the seasonal variation for the surface and 1000 dbar, where there is enough data to generate monthly velocity fields as a 3-month running mean. The results will be linked to the atmospheric dynamics, examining what drives the observed seasonal variations, giving a broader explanation to the observed phenomena. A more detailed focus is dedicated to the North Equatorial Countercurrent (NECC) in the chapter, this current has a strong seasonal cycle, and appears to feed from the Northern South Equatorial Current (nSEC). The NECC appears to show a double core in some regions that has been explained as a consequence of the position of the ITCZ (Urbano et al., 2006; Urbano et al., 2008). This hypothesis will be discussed, and a different explanation will be given on the light of the Argo velocities.

The fifth chapter was born as part of an international stage at Hobart Marine Laboratories (CSIRO), in Tasmania, Australia. The opportunity to apply the method to a different region, in a totally different context, was an exceptional opportunity to validate the method, and to develop new ways to obtain additional information

from the Argo data. The flow south of Tasmania has been monitored with the World Ocean Circulation Experiment (WOCE) section SR3, a repeat hydrographic section between Tasmania and Antarctica (Rintoul and Sokolov, 2001). The hydrographic observations show a westward subsurface flow south of Tasmania but do not allow the continuity of the pathway to the Indian Ocean to be explored. Model studies and observations suggest the Tasman Leakage provides the Pacific-to-Indian connection in a "Supergyre" linking the subtropical gyres of the three southern hemisphere basins (Speich et al., 2002; Ridgway and Dunn, 2007). We showed the Argo-inferred velocity field to become a very powerful tool to assess the flow of intermediate waters from the Pacific to the Indian Ocean. The Argo velocities were complemented with the information contained in the Argo CTD profiles to quantify the water transport by the Tasman Leakage.

The thesis ends with a chapter dedicated to summarize the main results and to point several ongoing and future developments. The method has proved to be a very powerful tool for many applications. As the amount of available data increases, the method will be able to assess the temporal and spatial variability of the velocity fields at shorter and faster scales, and the physical processes that control this variability will be unveiled. Further methodological developments are still possible, some of them currently underway, that will likely extend the potential of this methodology.

Several appendixes, which contain some methodological details as well as the scripts used in this thesis, are incorporated. Appendix A explores the possibility of the maximum entropy as a possible explanation to the Gaussian behaviour of the ocean velocity components. Appendix B is an essay that examines how this work projects beyond the current research, discussing the underlaying scientific methodology, and contrasting it to the scientific method enunciated by Karl Popper in 1934. Appendix C illustrates the basics of the harmonic analysis. Finally, a complementary CD contains Appendix C: the basic method scripts. All interested researchers are encouraged to use and improve them, and to correct any possible error, under their own responsibility.

Chapter 2

Data and Methods

The second chapter aims at giving a detailed explanation of the methodolgy that infers ocean velocities from the Argo floats' positions. The gridding process, error sources and possible error corrections are discussed. Despite a variety of possible errors, we show the Argo float trajectories to be a reliable source for estimating the ocean velocity fields. The overall relative error remains small for most of the velocity estimates, setting the basis for the application of the method to characterize different ocean regions.

2.1 Data description

All the available data up to September 2013 are used. The data are downloaded from the Coriolis Global Data Assembly Center site (ftp://ftp.ifremer.fr/ifremer/argo/). Four different kind of files are provided for each float: the profile file (wmo_prof.nc) which contains all profiles done by a certain float; the trajectory file (wmo_traj.nc) contains the data corresponding to the cycles repetition, this is, the consecutive positions of the float while at surface, and all the associated variables; the metadata file (wmo_meta.nc) contains the float and sensor characteristics, as well as some cycle parameters; and the technical file (wmo_tech.nc) where the technical variables of the instrument are stored (e.g. battery voltages and intensities). All files are identified by the number assigned to each float by the World Meteorological Organization (WMO). A detailed list of the variables found in each file can be found in the Argo user manual (version 2.1, 9 June 2008).

The coexistence of different float models leads to inhomogeneity in the floats' stored variables; thus, there are variables that are sampled only by some floats, depending on model and software version. Ollitrault et al. (2013) present a detailed description of the different kinds of existent floats and their characteristics. This happens, for example, for the variables that should store the arrival and departure times at the sea

surface which, if available, would allow estimating the surface drift before the first and after the last position transmission.

Only data flagged as 1 (good data) in the JULD_QC variable are considered. For the POSITION_QC we only keep the data with an accuracy better than 1500 m, including both Argo and GPS positioning (this is POSITION_QC = 1, 2, 3 or G).

The floats that performed less than three cycles in their lifetime are completely neglected. A very short life can be indicative of malfunction or damage during the release.

As in Ollitrault et al. (2013), surface velocities estimated to be larger than 3 m s^{-1} are discarded. The same is done for the deep velocities estimates, but using a 2 m s^{-1} threshold. Further discussion on these thresholds will be presented in next chapter, when we calculate the velocity probability density functions.

To calculate the Argo velocities the data contained in the trajectory file (wmo_traj.nc) is used. Many variables are stored in this file, but only a few are needed: LATITUDE (contains the latitudes corresponding to all consecutive positions of the float), LONGITUDE (contains the longitudes corresponding to all consecutive positions of the float), JULD (contains all the dates corresponding to the consecutive positions of the float expressed in Julian Days since 1st of January 1950), CYCLE_NUMBER (contains the number of the cycle in which the data have been collected, being 1 the release cycle), POSITION_QC (contains the quality control of the position data), JULD_QC (contains the quality control of the time data). All these variables contained in the trajectory file are enough to calculate the surface and deep velocities, but the PARKING_PRESSURE (containing the pressure at which the float is parked) has to be taken from the metadata file (wmo_meta.nc).

2.2 Velocity calculation

The principle behind the velocity estimation is very simple: we calculate the distance between two points and, knowing the time lapse between these two positions, it is possible to calculate the velocity. The cycle of an Argo float can be divided in five phases (Fig. 2.1):

1-. The cycle starts when the float arrives to the sea surface, being the first phase the surface drift (12 hours approximately for ARGOS transmission, 15 min for Iridium), when the float

transmits the data and positioning.

2-. The second phase starts with the descent from the surface to the parking depth.

3-. The third phase is the 10-day drift at the parking depth. The parking depth can be set by the operator who releases the float. It is generally set at 1000 dbar (approximately 79% of the floats), but other depths (mainly 200, 750, 1100 and 1500 dbar) have been employed (Fig. 2.2). This allows, in some cases when the number of float transmissions per area (hereafter float density) is large enough, to study the mean flow at other depths.

4-. The fourth phase corresponds to the descent from the parking depth to 2000 dbar, where the float will start the vertical profile.

5-. The fifth phase is the actual phase for which the Argo program was originally designed: the performance of a vertical CTD profile in the upper 2000 dbar of the water column. When the float arrives to the sea surface, a new cycle starts.

During the first phase the float is positioned several times by the satellites. The first position marked after surfacing is the position that will be assigned to the last T-S profile, but more positions will be given during the surface drift and

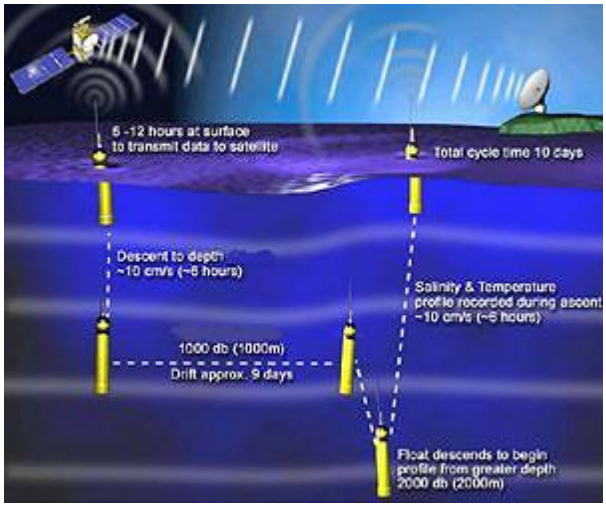

Figure 2.1: Argo floats' cycle scheme.

before descending again to the parking depth. These positions can be used to determine the surface displacement and, furthermore, to estimate the displacement in depth, in the time lapse between transmissions of consecutive cycles.

YoMaHa'07 use only the first and last position to generate a single surface velocity vector. In ANDRO2013 the surface velocity is split in two, providing two surface velocity vectors for each cycle. This doubles the available surface vectors, but reduces the accuracy (it actually doubles the error due to the positioning

accuracy) of the so calculated velocity, because the positioning error may account for a greater proportion of each displacement. ANDRO2013 splits the surface displacement in two periods; there are approximately 10 surface positions per cycle for the ARGOS positioning system, and Ollitrault et al. (2013) considered the resolution to be enough to provide two surface velocity vectors, despite a loss of accuracy.

Other options are possible (see chapter 6). For example, during the elaboration of the dataset an attempt to calculate a velocity vector for every pair of positions was carried on, but the instrumental resolution was not enough to estimate the distance between two consecutive positions with an acceptable accuracy.

In this work only the first and the last transmitted positions during a cycle are used to estimate the surface velocity. Even if several positions are provided during the transmission time, only the first and the last ones are used in order to maximize the distance and time, and thus to minimize the relative error due to instrumental limitations. The distance corresponds to the mean surface float displacement. This displacement value has no instrumental error beyond the positioning and data errors. The displacement may certainly be influenced by other factors, such as the wind drift, the drift associated to the surface gravity waves, and displacements caused by tidal and inertial frequencies, but the positions do provide an actual instrumental measurement.

For the deep displacement it is necessary to consider two cycles: we use the last position of one cycle as the first position of the deep displacement and the first position of the next cycle as the last position of the deep displacement. This procedure uses several approximations that lead to a greater velocity error than the one for the surface velocity estimation.

The overall velocity dataset calculated as mentioned above provides a total of 780809 surface velocity vectors, and 795719 deep velocity vectors. The larger number of deep velocities may be due to the increasing presence of floats equipped with Iridium positioning system, which is more reliable, but reduces the surface time transmission to approximately 15 minutes, excluding the possibility of estimating the surface velocity.

2.3 Filtering and gridding

The Argo sampling is very exhaustive but also uneven. For most applications, once the velocity for every single displacement is calculated, it is necessary to project the data on a regular grid. This requires specifying the desired temporal and spatial resolution. The better the spatial resolution the lower the temporal resolution will be.

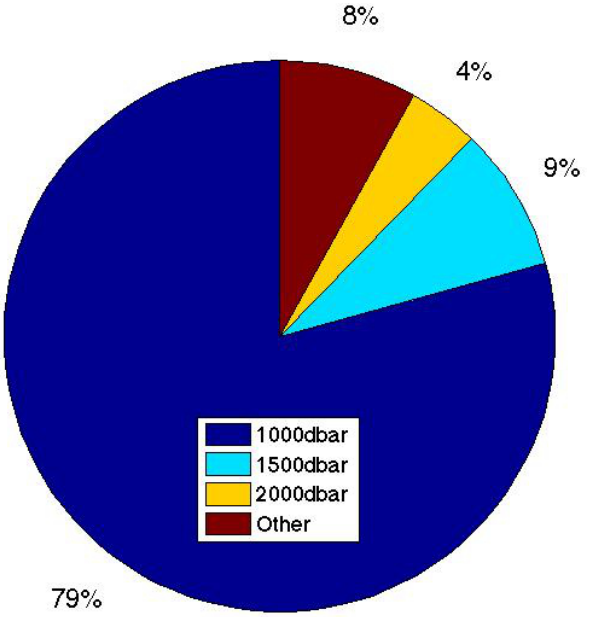

Figure 2.2: Parking depth distribution pie.

The gridding process will obviously depend on the available data density but it will also respond to the zonal and meridional dynamic correlations. For example, when working in the equatorial ocean, where the dynamic zonal correlation is much larger than the latitudinal one, it would be coherent to integrate a wider range in the zonal than in the meridional direction. Instead, if we want to study a boundary current, the opposite option would possibly be a good choice; and if the target region contains both meridional and zonal structures, no priority should be given to any of the directions. Therefore, depending on the regional dynamics we may end up using an ellipse rather than a circle, or rectangular cell elements instead of squared elements. In the present work the gridding process will be chosen to match the requirements of the different regions displayed, with different approaches as described in each chapter.

The temporal average also depends on the data availability. There are enough data to calculate the annual mean fields at spatial resolutions of $1° \times 1°$ both for the surface and at 1000 dbar all around the globe. However, in order to calculate monthly mean fields we would

need to either decrease the spatial resolution or to carry out some sort of temporal overlap, possibly a 3-5 months running filter; otherwise the calculated fields would often be very noisy and produce inconsistent velocity fields.

2.4 Sources of error and possible solutions

The vast majority of the floats up to 2010 have been equipped with the ARGOS transmission system, which has many transmission errors and needs an extended surface time (12 h) in order to calculate the surface velocities. Some of the recently deployed floats use Iridium positioning which gives good positioning accuracy during a very short stay at the sea surface (15-30 minutes). This can possibly lead to an improved estimation of the deep velocities but it certainly limits the accuracy of the surface velocity calculations because, despite the gain in position accuracy, the time at surface is drastically reduced, and often only one surface position is available.

Whilst the error in surface velocity depends only on the positioning accuracy -and the stokes drift and wind drogue-, the horizontal currents influencing the float during its vertical migration lead to an increased error when estimating the deep velocity vectors. The YoMaHa'07 dataset contained a detailed statistical study of velocity errors at the parking depth (Lebedev et al., 2007). The authors concluded that deep velocities have a most probable relative error at the parking pressure of 3%, with 54% of the deep velocities having a relative error less than 10%, and 97.6% of the velocities having an error smaller than the velocity value itself (Lebedev et al., 2007). We repeated the error calculation using the same method applied to our dataset, and obtained that the most probable error is less than 3%, with 58% of the deep velocity estimates having a relative error less than 10%, and 93.7% of the velocity estimates having an absolute error smaller than the velocity value itself.

When estimating the deep velocities we use the first and last surface transmissions while the float drifts at the surface. This involves several approximations that induce errors beyond the instrumental limitations:

1. We neglect the drift that takes place during the vertical migration of the floats. Additional to the sinking and surfacing to the parking positions, there is also a migration down to 2000 dbar previous to the start of the vertical

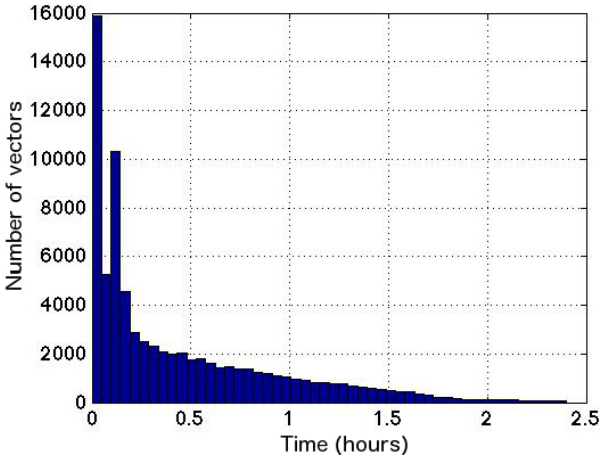

Figure 2.3: Histogram of the delay in positioning after arrival to the sea surface, as determined from those floats using the ARGOS transmission system and containing information on the surfacing time.

conductivity-temperature full profile. The total vertical migration time, comprising the descent from the surface to the parking depth, the ultimate descent and the profile execution, is about 40000 seconds (some 12 hours). During this time the float migrates 4000 meters in depth while exposed to all possible currents between the surface and 2000 meters depth, distorting the measurement of the real drift at the parking depth. Nevertheless, this happens only for about 5% of the total cycle time (typically about 0.5 days out of 10 days), thus usually it is a relatively low contribution to the total drift.

There is no real solution in the Argo profiler data "per se". Error estimates can be obtained on the basis of the water speed difference between the surface and the parking depth and the time spent during the migration. This is just a rough estimation of the magnitude of the error because it assumes a regular variation in the vertical distribution of the horizoantal velocity and neglects the migration to the maximum depth. It is however a reasonable estimation of the size of the error due to the horizontal drift during the vertical migration. This error estimation was first given in the YoMaHa'07 dataset by Lebedev et al. (2007).

2. There is a time gap between the actual arrival of the float to the surface and the positioning time through the satellites (Fig. 2.3). This leads to an additional error in the determination of the real emerging point.

This problem would have a partial solution if the trajectory file always stored the variable JULD_ASCENT_END of the trajectory file. This variable corresponds to the time when the float arrives to the surface. By knowing this time, we could extrapolate the emersion position from the surface velocity as estimated from

the surface drift. Unfortunately, this variable is empty most of the time.

3. There is also a gap between the last positioning and the actual immersion position (Fig. 2.4).

This could also be partly solved, as for the emersion position, if the value of the variable JULD_DESCENT_START was available; unfortunately, this is empty in the majority of the cases.

4. An additional difficulty comes from the fact that the parking pressure contained in the metadata file is the programmed parking pressure. The real drift depth may vary a little from cycle to cycle, and there are a few instances that have been found to contain an error in the nominal parking depth.

As in YoMaHa'07, we choose to set the nominal parking depth as the real parking depth. The recently published ANDRO2013 reports an error in the parking depth for approximately 6% of the time; these have not been corrected in our data set.

The errors associated to the above issues usually cannot be corrected, as the necessary data for this correction is absent in the majority of the cases. Even though, the number of displacements containing all the data necessary to estimate the real positions of the deep displacement is large enough to give an estimate of the error caused by the surface drift (Fig. 2.5).

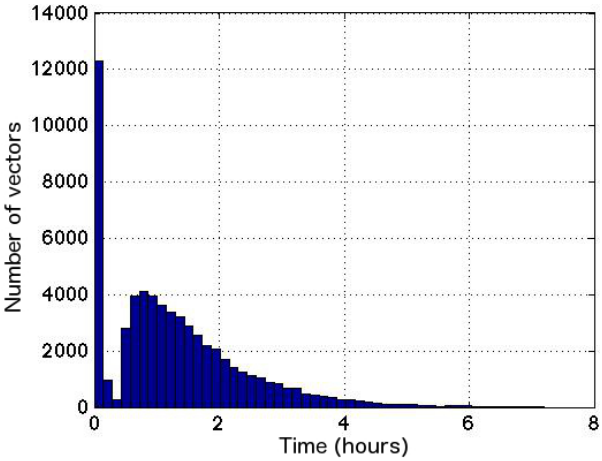

Figure 2.4: Histogram of the delay between the last position and the beginning of the descending profile, as determined from those floats using the ARGOS transmission system and containing information on the plunging time.

2.5 Surface drift error estimation

The estimation of the error due to the surface drift, before the first position and after the last one, can be done only for those floats containing all the necessary data. This is just an estimation of the error, it cannot be used to correct

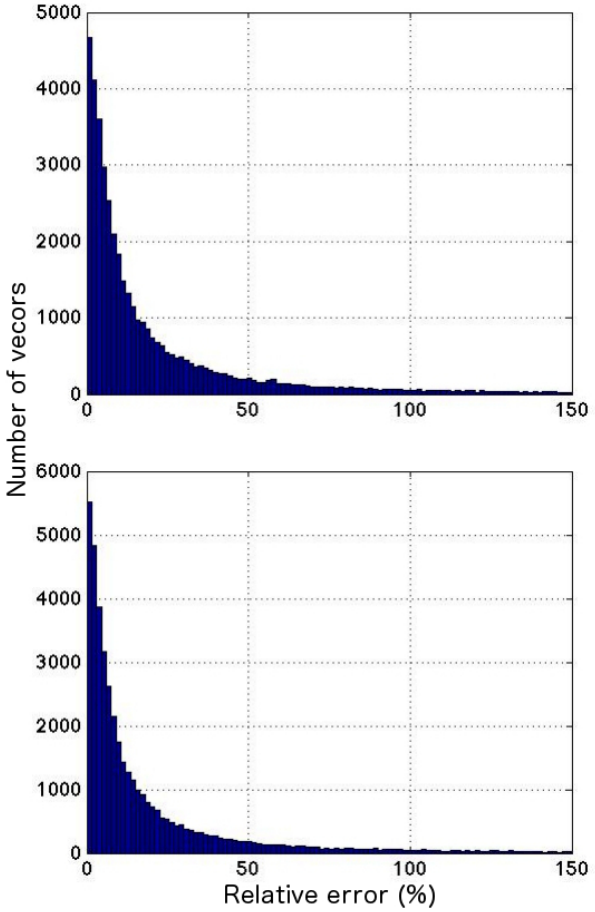

Figure 2.5: Histogram of the relative error in the deep velocity estimate due to the combination of the untracked surface drift and the horizontal drift during the float's vertical migration. The top and bottom panels respectively show the zonal and latitudinal velocity components.

the original data.

To estimate the real position when the float arrives to the sea surface, we calculate the time between the surface arrival and the first transmitting position, and assume that during that time lapse the float moves with the same mean velocity calculated from the first and the last surface positions at surface. Subtracting this displacement from the first position, we can estimate the position where the float actually arrived to the sea surface.

The method to estimate the real sinking position is similar, but using the time lapse between the last position and the start of the descending profile. Assuming again that, during this time interval, the float moved with the calculated mean surface speed, and adding this displacement to the last position, we can reconstruct the actual position where the descending profile started.

The difference between the velocity calculated from the original and corrected positions is assumed to be the error introduced in the deep velocity calculation by the surface drift of the float during the interval between the arrival to the surface and the first transmission position, and between the last transmission position and

the start of the descending profile.

In addition, not all the available data is valid: the status of the dates is flagged depending on whether the date has been estimated, extracted from the metadata, transmitted by the float, or is unknown. For our purposes only those dates which have been transmitted by the floats can be used. Therefore, we keep only those data with values flagged as "2" in the STATUS variable. The presence of correct data, both for JULD_ASCENT_END and JULD_DESCENT_START, is confirmed for only 75066 cycles of the total 780809 surface velocity data values. Therefore, only 9.6% of the total velocity data contains enough information to estimate the error due to surface drifting that cannot be tracked. The mean time gap between the arrival to the sea surface and the first position (Fig. 2.3) is 31 minutes (less than 1 hour in 84% of the profiles), and the mean time gap between the last float's position and the immersion time (Fig. 2.4) is 1 hour 21 minutes (less than 2 hours in 77% of the profiles). An analogous procedure can be followed to correct the parking depth velocities. The first step is to correct the error associated to the untracked surface drift; knowing the duration of the surface drifts and assuming the float moves with the mean surface velocity before the first transmission and after the last one, we can estimate the real emersion and immersion positions and recalculate the floats deep velocity. The difference between this corrected velocity and the previous velocity estimate is considered as an estimate of the deep-velocity error due to the surface drift. This surface drift introduces a small error which in approximately 70% of the cases is less than 10% of the deep velocity value, and in 95% of the cases is less than the deep velocity value, this result applying for both velocity components.

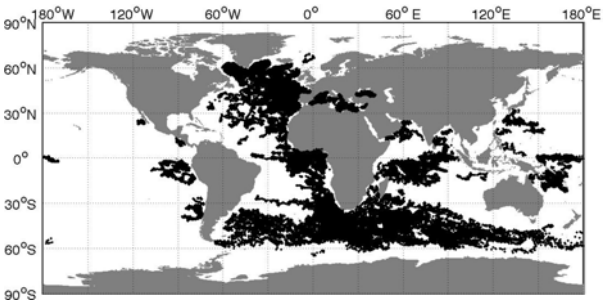

Figure 2.6: Geographical distribution of the profiles containing all the necessary variables to estimate the surface drift error.

To have an estimation of the total error, we add the error caused by the untracked surface drift to the error associated to the horizontal

drift during the vertical migration (Lebedev et al., 2007). The overall error appears to be less than 10% of the deep velocity value in approximately 50% of the profiles, and in 92% of the profiles it is smaller than the deep velocity value for both components of the deep velocity (Fig. 2.5). In particular, the mean error contribution due to the surface drift is much smaller than the error due to the horizontal drift during the vertical migration.

The calculation of the surface drift error is possible only for those profiles where the previously mentioned variables are present, Figure 2.6 shows the distribution of the profiles where this is possible. Despite there is no global coverage, the distribution is wide enough to confirm that our estimates are reliable for the whole data set. It is important to remember that these estimations are only for a relative small number of vectors; they provide an estimate of the error but cannot be used for correcting the velocity fields.

2.6 Non-instrumental error sources

Beyond the error sources associated to the positioning limitations, the codification process, and the instruments behaviour, there are some factors that may affect the calculation of ocean velocities.

Argo profilers have not been designed to track the ocean currents, so it is natural to expect they are not the optimal instruments for velocity measurements. This is especially relevant at the sea surface, where the floats are exposed to the wind stress and the Stokes drift due to the waves. Surface drifters are usually equipped with a large drogue to meet the World Ocean Circulation Experiment (WOCE) standards (Niiler et al., 1987). The drogue has to be large enough, typically a 40:1 drag area ratio (drogue area as compared with area of all other elements), to guarantee that the drifter follows closely the sea currents, i.e. the direct effect of the winds over the exposed portion of the drifter and the currents over the subsurface parts of the buoy (the surface buoy itself and cable between the surface buoy and the drogue) is relatively small.

Argo floats, however, are cylinders with varying length; the length changes depending on the model, but always between 1 and 2 m long. While drifting at the sea surface they are almost totally immersed in the water, with only

a few centimetres of the sensor and the antenna emerging, therefore the wind drag may be safely neglected. The resulting wave-induced drift, on the other hand, depends mostly on the amplitude of the locally-generated wave field, as swell appears to induce no net drift because of compensating effects between the Stokes and the Stokes-Coriolis effects (Rascle et al., 2006; Rascle and Ardhuin, 2009). In the tropical Atlantic Ocean, for example, the wave field is moderately low all year long, with annual-mean significant-wave heights that do not exceed 2.5 m, with contributions of about 1 m from the wind sea and 2 m from swell (Gulev et al., 2011). Considering solely the local wind sea, we may use annual-mean typical values of wave amplitude (0.5 m), wave length (100 m) and wave period (10 s) for the tropical Atlantic to calculate a Stokes drift velocity of about 1 cm s^{-1}; if the wave amplitude is chosen to be 1 m then the drift rises to 4 cm s^{-1}. The Stokes drift will thus vary depending on the region under consideration.

Despite the direct wind drogue is very small, the displacements and velocities experienced by the Argo floats at the sea surface have to be considered as only representative of the uppermost water layer. For example, a diurnal layer is formed during periods of intense diurnal warming. In these circumstances the Argo-inferred velocities might not be the best choice to estimate the transport in the whole surface mixed layer.

Finally, it is important to consider that the actual velocity estimates are contaminated by the existence of high-frequency motions such as the semidiurnal and diurnal tides and the inertial motions. During its 12-hours surface stay, the float has enough time to describe a large portion of these cycles. In the open ocean an inertial oscillation describes a circle with a radius of the order of several kilometres; therefore, if the surfacing time coincides with half an inertial period (as it happens at 30° of latitude), the collocation error may be of the order of twice this radius. Tides, on the other hand, bring relatively small oscillations in the open ocean (just a few hundred meters) which may increase largely near the coast, easily by a factor of 10 in the along-shore direction.

Chapter 3

Argo-Inferred Velocity Probability Density Functions

In this chapter we turn to the statistical description of the Argo-inferred ocean velocity distributions, and in the following chapters we will present several specific applications. The non-Gaussian behaviour of the ocean velocity probability density functions (PDFs) was first remarked by Lilly (1969). Since then, other studies have looked at the ocean velocities PDFs, calculated either from Lagrangian floats, altimetry, or current-meter measurements (Jimenez, 1996; Minh et al., 1996; Stammer, 1997; Weiss et al., 1998; Llewellyn Smith and Gille, 1998; Bracco et al., 2000; Gille et al., 2000; Isern-Fontanet et al., 2006). The principal aim of these studies has been to determine if the ocean velocity PDFs can be considered to follow a Gaussian distribution: Are the ocean velocities locally Gaussian? And what does local mean? It has been demonstrated that lateral and temporal inhomogenities can lead to non-Gaussian distributions, with exponential-like tails, but can we consider these deviations from Gaussianity to arise because of geographical and temporal data integration? Or the exponential tails are indeed an intrinsic property of the ocean velocity PDFs? In this chapter we address these questions using the ocean velocities as inferred from the Argo floats.

In the first part of this chapter (sections 3.1 through 3.4) we apply the same normalization method used by Bracco et al. (2000), based on the results of Swenson and Niiler (1996), to different ocean regions; these authors reported an artefact non-Gaussian behaviour which increased with the size of the considered area, ascribed to the appearance of lateral inhomogeneities. Our results indeed show the relevance of data homogeneity for reducing the kurtosis of the PDFs. In the second part of this chapter (sections 3.5 and 3.6) we build an ocean velocity model that reproduces the PDF distribu-

Rosell-Fieschi, M., Gourrion, J., Pelegrí, J.L., 2013. Ocean velocities PDFs from Argo's inferred velocities. Submitted to Ocean Modelling.

tions as obtained from the Argo velocities. The results are very good for the surface velocities, closely reproducing the original PDF; the deep velocities, however, are more difficult to reproduce but yet a fairly good agreement is achieved. The possibility of varying the parameters of the models, such as the local kurtosis or the mean-variance correlation, shall help us better understand how the ocean velocities are distributed. A potential link between the observed distributions and those that would arise from maximum entropy (ME) considerations is explored in appendix A.

3.1 Normalized velocity PDF

3.1.1 Normalization and bin size

Following Bracco et al. (2000). a normalization process is introduced aimed at correcting the lateral inhomogeneities. The procedure consists in (a) dividing the ocean domain in bins of equal size, (b) calculating the mean and standard deviation for each bin, and (c) normalizing the data for each bin with these local values (subtract the mean and divide by the standard deviation). In Bracco et al. (2000) the normalization was explored for three different bin sizes: 1, 2 and 3° square bins. These authors eventually chose 2° square boxes (bins with less than 25 realizations were neglected) as a compromise between a reasonably good local normalization and a sufficiently large number of data (the greater the amount of data the less noisy the distributions). Using these normalized PDFs, they calculated the kurtosis of both the zonal and meridional velocity components and found that it decreased proportional to bin size. This suggested that, despite the nomalization of the velocity values, part of the observed local kurtosis may still be caused by the presence of lateral inhomogeneities at scales smaller than the bin size.

So what should the box size be to eliminate the lateral inhomogenities? We have repeated the normalization process with the Argo-inferred data for different box sizes (1/2°, 2/3°, 1°, 3/2°, 2°, 3°, 4°, 5°, 6°, 8°, 10°, 12°, and 15°) in order to quantify the variation of the local kurtosis values with box size. Figure 3.1 shows the results for the zonal and latitudinal components at both the surface and 1000 dbar. The solid lines show the kurtosis of the whole velocity data after carrying out, for each bin element, the local normalization procedure. In this calcula-

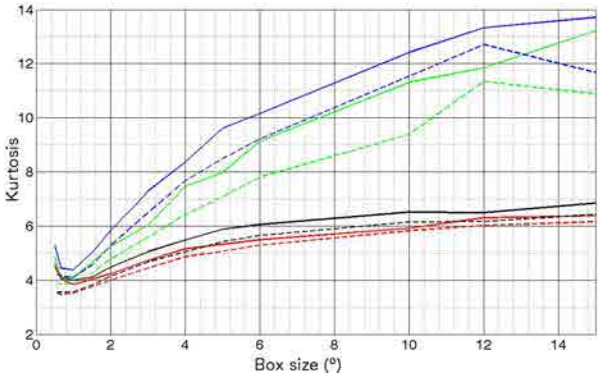

Figure 3.1: Mean kurtosis as a function of normalization box size. Dashed lines: mean kurtosis is calculated as the average of the kurtosis values for all boxes with the same size. Solid lines: mean kurtosis is calculated using the whole data set, put together after normalizing the velocity fields within each box. The analyzed velocities correspond to surface meridional (black), surface zonal (red), 1000 dbar meridional (green), and 1000 dbar zonal (blue).

tion a local normalization is carried out for each bin element but then all normalized velocity values are put together in order to obtain the mean kurtosis. The dashed lines, on the other hand, show the mean of the kurtosis values calculated locally for each bin element. The kurtosis calculated using the whole (normalized) data is always higher than the mean of the local kurtosis values. The absolute difference between both numbers gets smaller as the size of the bin is reduced, down to a bin side of 1°, but the relative difference remains approximately constant. The difference suggests that, for all bin sizes down to 1°, there are limitations in the normalization process, possibly because of lateral or temporal inhomogeneities associated to spatial and temporal variability of the "local" mean and variance.

The results also show that deep velocities have kurtosis values which are always higher than the kurtosis of the surface velocities, and the kurtosis of the zonal velocity is always slightly higher than the one for the meridional velocity. Additionally, the kurtosis decreases proportional to bin size, reaching a value about 3.5/4.0 for boxes with sides of 1° for the surface/deep velocities, fairly close to the theoretical expected value (3) for Gaussian distributions (DeCarlo, 1997). The stabilization of the kurtosis could indicate the scale at which the turbulence is more isotropic, and the lateral inhomogeneities have a smaller effect. However, the number of available velocity vectors decreases sharply as the side of the box becomes less than 2° (Fig. 3.2); this is because boxes with less than 25 velocity vectors are discarded. As a result, the number of available boxes increases with decreasing box size up to a maximum value

of 1300 boxes at the surface and 1000 boxes at depth for boxes sized between 1.5° and 2°. Because of this reduction in the number of available velocity vectors, and despite it appears that 1° -side boxes brings the kurtosis values to a minimum, which is close to the expected value for a Gaussian distribution, in the remaining of this section we will normalize the velocity vectors using 2° boxes (for applications in other sections we will also use smaller boxes to test the difference).

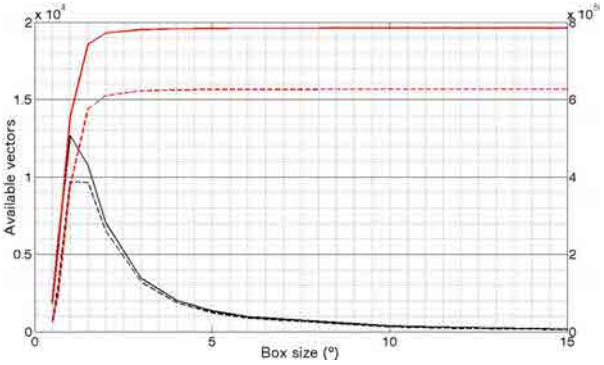

Figure 3.2: Number of boxes and available normalized velocity vectors as a function of normalization box size. Dashed lines: Deep velocities. Solid lines: Surface velocities. Red: Number of available normalized velocity vectors. Black: Number of boxes in the domain (global).

In our previous analysis we have carried out space partitions but have not done any time splitting, which would be necessary if there are significant temporal changes in the dynamic character of the geophysical flows. Therefore, (1) likely the spatial scale of our bins is not small enough to differentiate between distinct adjacent dynamic regimes and, equally important, (2) the lack of a temporal partition may group data from different dynamic regimes (e.g. the boxes comprise velocities from all seasons, from approximately 10 years of data). As a result, we recognize it is probable that our analyses include lateral and/or temporal inhomogeneities that do not allow for a fully correct normalization, leading to an artificially high kurtosis. Nevertheless, the relatively low kurtosis values for 2°-side boxes (values between 4 and 5, depending on the depth level and the velocity component) grants us some confidence.

3.1.2 Highly energetic events

Bracco et al. (2000) presented the PDFs accompanied by a map showing the position of the most energetic events. This is especially meaningful as, once the velocities have been demeaned and normalized by the standard deviation, those values located in the tails of the

normalized PDF are locally high velocities but do not necessarily represent extreme events at a regional or global scale. For example, in a box where the velocities are large but periodically experience direction reversals, the standard deviation will be high; in contrast, in a box with weak currents the standard deviation is likely to be much lower. The first case would lead to relatively small normalized high velocities while the second one will yield much higher normalized extreme values. Therefore, the distribution of the mean values and standard deviations may not be a very good indicative to locate the most energetic events.

An alternative is to compare the individual values within the global distribution. In Figure 3.3 we show the location of those velocity vectors that differ more than 3.5 times the standard deviation from the global mean. We may observe that the most energetic regions are located in western boundary regions, the equatorial ocean and the Antarctic Circumpolar Current (ACC). All these regions comprise the most energetic currents found around the globe.

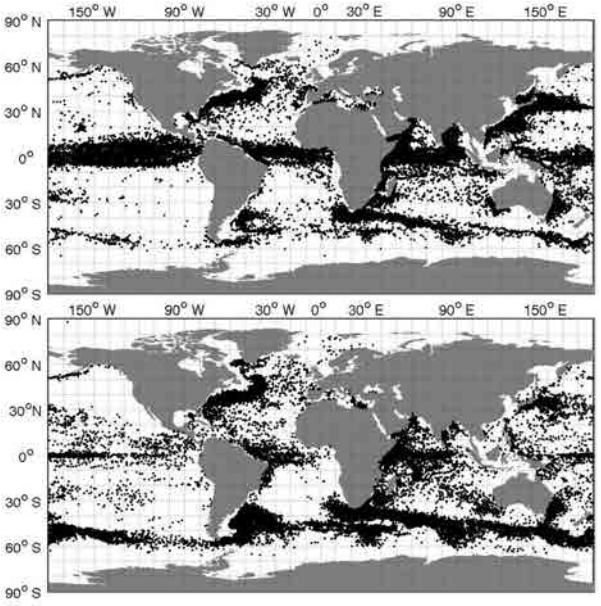

Figure 3.3: Geographical distribution of the highly energetic events (over 3.5 sigma from the global mean), both at the sea surface (upper panel) and at 1000 dbar (lower panel).

3.2 Regional and global distributions

3.2.1 Global PDFs

Let us first consider the global velocity dataset; later on we will look at PDFs for different areas and will relate their particular deviations from Gaussian behaviour in terms of the dynamics of the considered particular area.

After demeaning and normalizing in boxes of

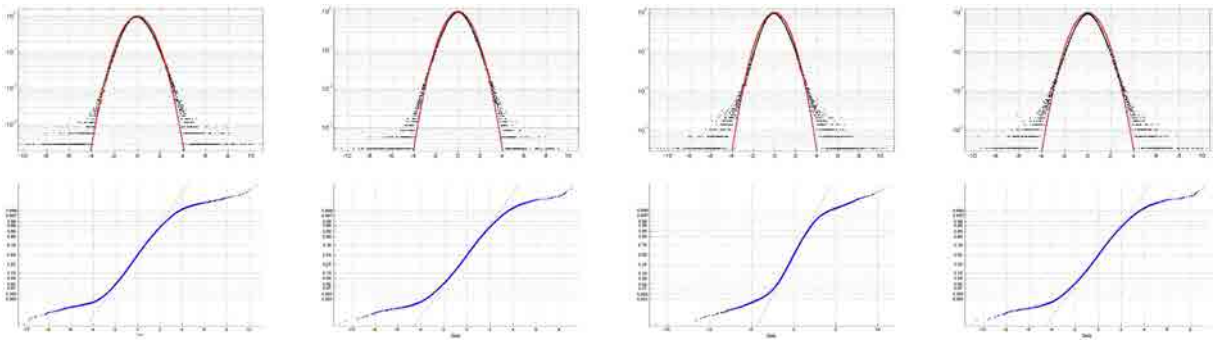

Figure 3.4: Analysis of PDFs using the normalized global velocities. The upper panels show semi-log plots of the empirical PDF, with the best-fit Gaussian distribution overlapped in red. The lower panels show the normal cumulative PDFs as deduced from the data (dotted blue points) and the best-fit Gaussian distribution (dotted gray line). From left to right: Surface zonal, surface meridional, deep zonal and deep meridional velocities.

2°, we have a total of 771.485 surface realizations and 610.270 realizations at 1000 dbar.

The top panels of Figure 3.4 show a semi-log representation of the PDFs, together with the overlapped Gaussian fits, for the zonal and latitudinal components of the global set of locally normalized velocities. The bottom panels show a normal cumulative representation of the same data set, helpful to assess whether the data comes close to a normal distribution, i.e. any deviation of the data from the theoretical line indicates a deviation from the Gaussian distribution. We may appreciate that all four variables display PDFs with energetic normalized events substantially away from the Gaussian distribution, something quite clear for the most energetic 5% events. These distributions resemble those presented by Bracco et al. (2000), as obtained from either real ocean data or numerical simulations of freely evolving barotropic turbulence (Fig. 3.5).

The kurtosis values derived from the global data, as obtained using the 2°-bin normalized velocities, are shown in the top two lines of Table 3.1. At the sea surface the kurtosis lay between 4.24 (latitudinal component) and 4.49 (zonal component); at 1000 dbar they range between 5.22 (latitudinal component) and 5.81 (zonal component). These values are significantly greater than the Gaussian expected value

of 3, indicating a substantial departure from this distribution. These departures may either indicate a real non Gaussian distribution or correspond to an artefact situation, caused by an improper removal of lateral or temporal inhomogeneities.

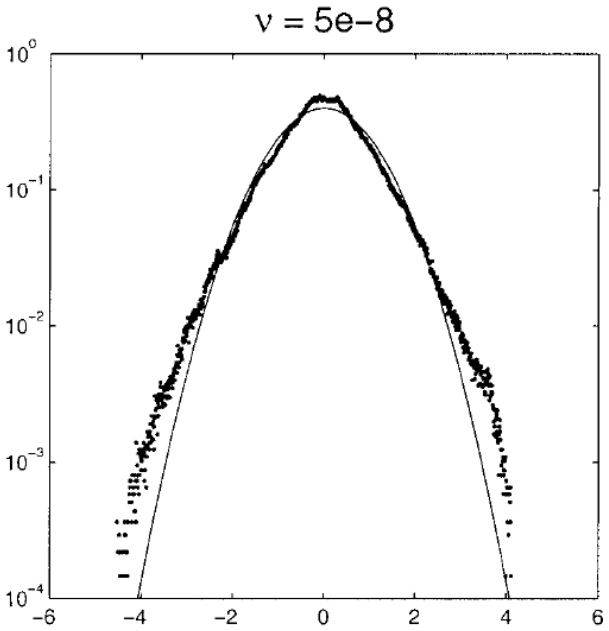

Figure 3.5: Distribution of a simulation of passively advected particles in freely evolving barotropic turbulence.Reproduced from Bracco et al., 2000

3.2.2 Regional variation

In order to assess the possible influence of different dynamical regions on the resulting distributions, the kurtosis has been calculated for five distinct geographical locations. The five selected areas are (1) a very intense and zonally coherent ACC, (2) the relatively weak center of the South Atlantic subtropical gyre, (3) an intense but intermittent system of equatorial currents, (4) the intense eddies regularly detaching from the Agulhas Current, and (5) a transatlantic section which encompasses a variety of dynamic regimes; Figure 3.6 shows the location of these different regions on a map.

We use the Kolmogorov–Smirnov (K–S) test to assess how close the observed PDF is to the Gaussian distribution. The statistics is calculated under the hypothesis that the sample is drawn from the reference distribution: the higher the p-value, the more likely the observations will follow a Gaussian distribution; in this case the two distributions are related and the null hypothesis (the two distributions bear no relationship), rejected. Results are presented in Table 3.1. The corresponding PDFs and normal-cumulative plots, in Fig. 3.7.

Antarctic Circumpolar Current

The Antactic Circumpolar Current (ACC) region is here located in a latitudinal band comprised between 56°S and 60°S (Fig. 3.6). The ACC has been chosen as to represent an extense energetic region, characterized by a dominant zonal flow both at the surface and at depth (Richardson, 2008). The kurtosis is reasonably low for both components at surface and depth. Nevertheless, the K-S test only allows rejecting the null hypothesis for the zonal velocity component. For the latitudinal velocity component (both at the sea surface and at 1000 dbar) the null hypothesis cannot be rejected, indicating that the distribution of the meridional components for the ACC is close to a Gaussian distribution.

South Atlantic subtropical gyre

The South Atlantic subtropical gyre is a region expected to have relatively weak currents (Stramma and Schott, 1999). We characterize it geographically by a box comprised between 40°S-20°S and 0°-30°W (Fig. 3.6). The kurtosis at the sea surface is close to 3.5 for both components, and the K-S test cannot reject the null hypothesis for both the zonal and latitudinal components. The deep velocities are apparently less homogeneous, as reflected both by the relatively high kurtosis values and the acceptance of the null hypothesis through the K-S test.

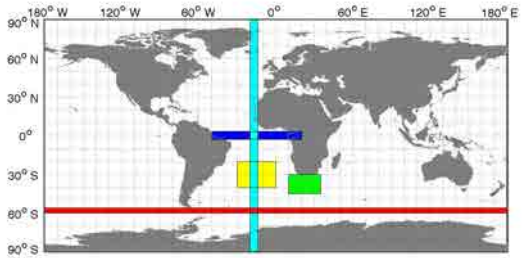

Figure 3.6: Geographical situation of the studied regions: ACC (red), the center of the South Atlantic subtropical gyre (yellow), the Agulhas Leakage (green), the Atlantic Ocean equatorial band (blue) and the transatlantic section (cyan).

Equatorial band

The equatorial band is selected here to comprise all velocity vectors between 3° S and 3° N (Fig. 3.6). It represents an area with high dominance of the zonal currents. Near the sea surface these currents are fairly

Table 3.1: Ocean velocities regional kurtosis and skewness

	Data Points	Zonal K	Merid K	Zonal Sk	Merid Sk	p-value Zonal	p-value Merid
Global Surf	771485	4.49	4.24	0.1301	-0.0162	0	0
Global Deep	610270	5.81	5.22	0.0839	-0.0026	0	0
ACC Surf	10348	3.48	3.51	0.1325	0.0298	4.1e-06	**0.0888**
ACC Deep	12568	3.30	3.20	-0.0736	0.2842	2.93e-12	**0.0657**
Gyre Surf	12568	3.53	3.32	0.1064	0.1353	**0.0410**	**0.0239**
Gyre Deep	13125	3.85	4.01	-0.1346	0.2010	8.81e-05	1.95e-12
Equat Surf	33951	3.45	3.72	0.0584	0.0041	0.0104	1.96e-05
Equat Deep	18488	5.24	4.15	-0.0580	0.2972	2.51e-15	1.86e-07
Agulhas Surf	7380	4.91	4.40	0.1060	-0.1038	1.89e-08	3.08e-07
Agulhas Deep	6543	4.84	4.19	-0.0316	-0.3593	6.46e-04	4.06e-07
Transatlan Surf	19155	8.71	6.24	-0.0315	-0.0851	8.57e-13	4.66e-11
Transatlan Deep	13283	5.11	3.95	0.0700	0.0221	3.04e-06	1.05e-04

stable throughout the year whilst at 1000 dbar the currents experience substantial reversals as a consequence of eastward and westward propagating waves (see chapter 4). At the sea surface the kurtosis values are close to 3.5 for either component; nevertheless, the K-S test cannot confirm the PDFs to have a Gaussian behaviour. At 1000 dbar the distributions are substantially different from Gaussian (large kurtosis values and very low p-values that confirm the null hypothesis).

Agulhas Leakage

The Agulhas Leakage is here chosen to correspond to the region running between 45°S-30°S and 10°E-35°E. It is a relatively small and highly dynamic area (Boeble et al., 2003; Richardson et al., 2003), which includes only a few boxes and should lead to a more Gaussian distribution. The kurtosis values range between 4 and 5 for either component, both at surface and depth, suggesting a departure from the Gaussian distribution; this is confirmed by the rejection of the null hypothesis in the K-S test.

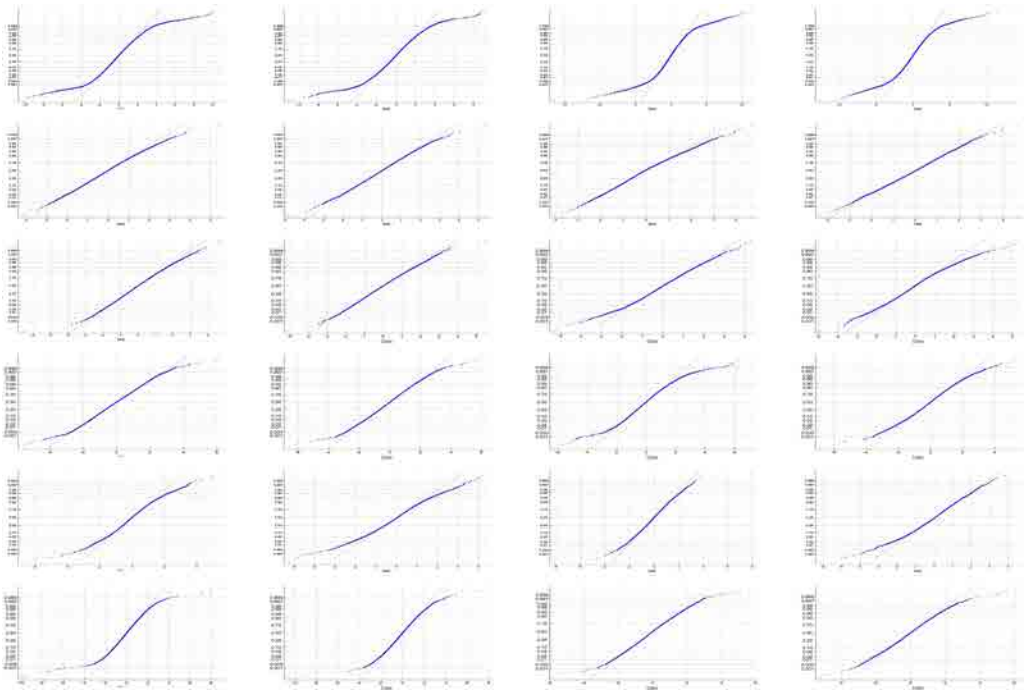

Figure 3.7: Normal cumulative PDFs for different regions. The columns, from left to right, correspond to the different velocity components at surface and 1000 dbar: zonal surface, meridional surface, zonal 1000 dbar, meridional 1000 dbar. The rows correspond to different geographic domains, from top to bottom: Global, ACC, Southern Atlantic subtropical gyre, equatorial band, Agulhas Leakage, transatlantic section (see Fig. 3.6 for the precise geographical boundaries of each region).

Transatlantic section

A full transatlantic section, chosen to lay between 14°W and 20°W, represents an area crossing very different dynamic structures (interior gyres, zonal equatorial jets, western and eastern boundary currents). Among the selected regions, it presents the highest kurtosis values for the surface distributions; for the deep velocities the kurtosis values are also substantially away from the (expected Gaussian) value of 3. In all cases the null hypothesis is rejected through the K-S test.

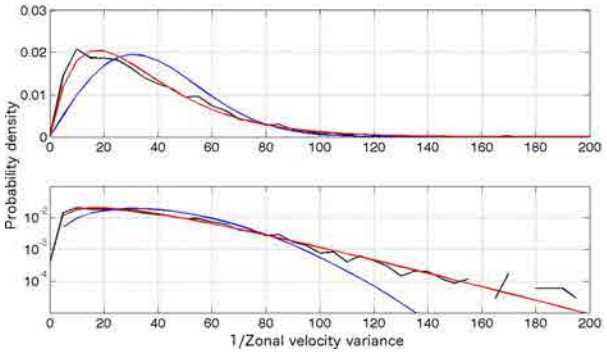

Figure 3.8: Inverse of the empirical variance of the surface zonal velocity (black). The best-fit Rayleigh (blue line) and gamma (red line) distributions are shown.

3.3 Modelling the ocean velocity PDF

3.3.1 The model

Our results have shown that the more homogeneous is an area the lower the kurtosis will be and the more Gaussian-like its behaviour. This is attained by selecting sufficiently small regions: we have seen that 2°-boxes have a fairly good Gaussian behaviour. Therefore, we expected the 2°-box normalization procedure to allow the comparison of velocities from different areas, i.e. if the ocean velocities were locally Gaussian and the normalization procedure was effective the global array of normalized velocities should also be Gaussian. However, we have seen that this is not the case, when combined over larger regions the ocean velocity PDFs have (most of the time) a substantial departure from Gaussianity, i.e. the lateral and/or temporal inhomogeneities are not properly corrected by the normalization procedure.

In this section we introduce a simple model aimed at exploring the local Gaussian behaviour of the ocean velocity PDFs, and the way these may be combined to produced global PDFs. We will illustrate the application of the model to the zonal velocity component; however, the results are extensive, with minor modifications, to the latitudinal component.

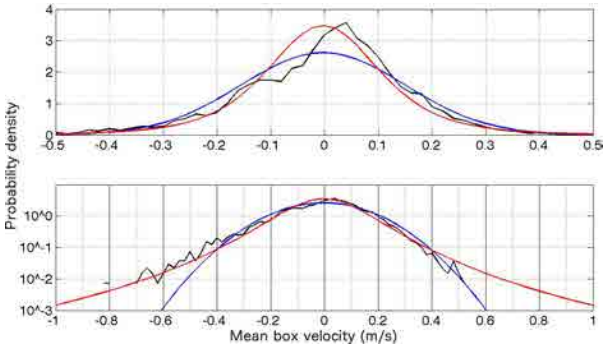

Figure 3.9: Distribution of the local mean velocities (black) together with its Gaussian fit (blue) and the fit using a t-Student distribution with 4 degrees of freedom (bllue).

To model the ocean velocities we generate 10000 virtual boxes, each containing 1000 velocity vectors generated following a properly specified Gaussian distribution. The Gaussian distribution of each box is progressively modified as further parameters, representing more complex conditions, are considered. The results of the model will be compared with the distributions arising from the global velocity data, after normalization in 2°-boxes.

The basic model considers the ocean velocities to be locally Gaussian, each box with constant mean velocity and standard deviation values, taken as equal to the corresponding values of the global distribution.

The first modification is on the variance of the variance: we still consider that the velocities are locally Gaussian with constant mean but choose a variance distribution such that the inverse of the variance follows a gamma distribution. This is motivated by the observation that, in Bayesian probability theory, the inverse-gamma distribution may arise as the marginal posterior distribution for the unknown variance of a normal distribution (Raiffa and Schlaifer, 1961). The improved match between the data and modelled variance confirms the adequacy of the approximation (Fig. 3.8).

The second improvement is to model the distribution of the mean, either using a Gaussian or a t-Student distribution (Fig. 3.9), still maintaining a local Gaussian behaviour. The degrees of freedom for the t-Student distribution are adjusted for an optimal fit to the data, which implies a compromise between fitting the central values and the long tails.

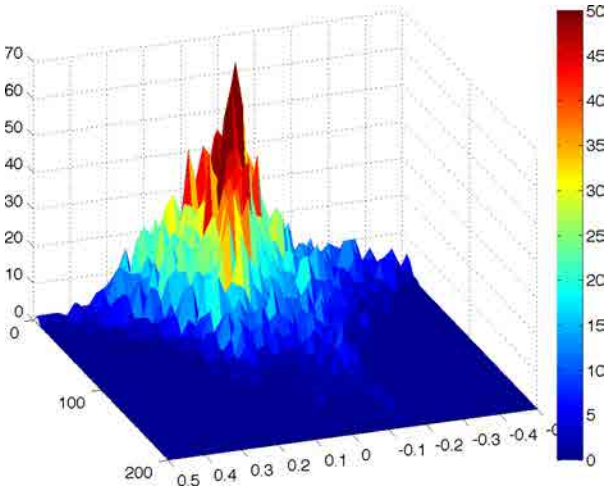

Figure 3.10: 2D PDF of the surface velocities: Mean (x axis) - Inverse Variance (y axis)

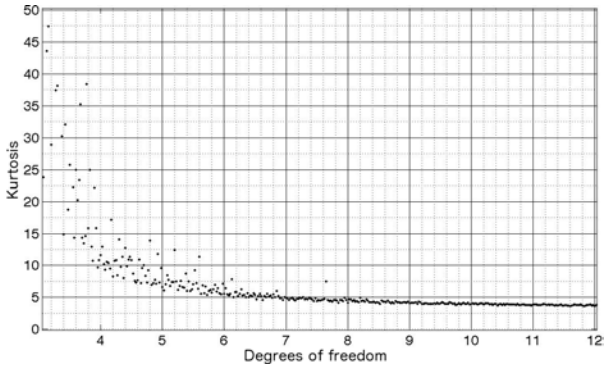

Figure 3.11: Kurtosis for t-Student distributions randomly generated with different degrees of freedom.

We find that 4 degrees of freedom generate a t-Student distribution that properly fits the local mean velocity distribution at the sea surface.

The next change is to introduce a correlation between the mean and the variance, as larger variances are expected for high velocities. We do so through the analysis of the two-dimensional PDF (Fig. 3.10), as a function of both mean and variance: this specifies the probability associated to a given pair of mean and variance values, maintaining the condition of local Gaussian distributions.

Finally, we explore further this last case but force the velocities to be locally non-Gaussian. Specifically, we use a t-Student distribution to simulate the effect of local kurtosis: with 9 degrees of freedom for a kurtosis of approximately 4, and with 4 degrees of freedom for a kurtosis of about 15. The relation between kurtosis and the number of degrees of freedom for the t-Student distributions is extracted from the analysis of a random generation of PDF distributions (Fig. 3.11).

3.3.2 Model results

Surface

The baseline Gaussian behaviour does not properly fit the real distribution (Fig. 3.12) but can be used to appreciate the evolution of the modelling process. The results of the model change drastically as we introduce the first modification (the inverse variance is selected to follow a gamma distribution, Fig. 3.8): the distribution tails fall much closer to the real distributions (Fig. 3.12). The peak value is too high but yet it is a much better approximation to the real distribution, suggesting the long tails (observed when studying the ocean velocities distribution at a regional or global scale) to be generated by the variance distribution.

Introducing the second change (the mean is modelled to follow a Gaussian distribution. Fig.

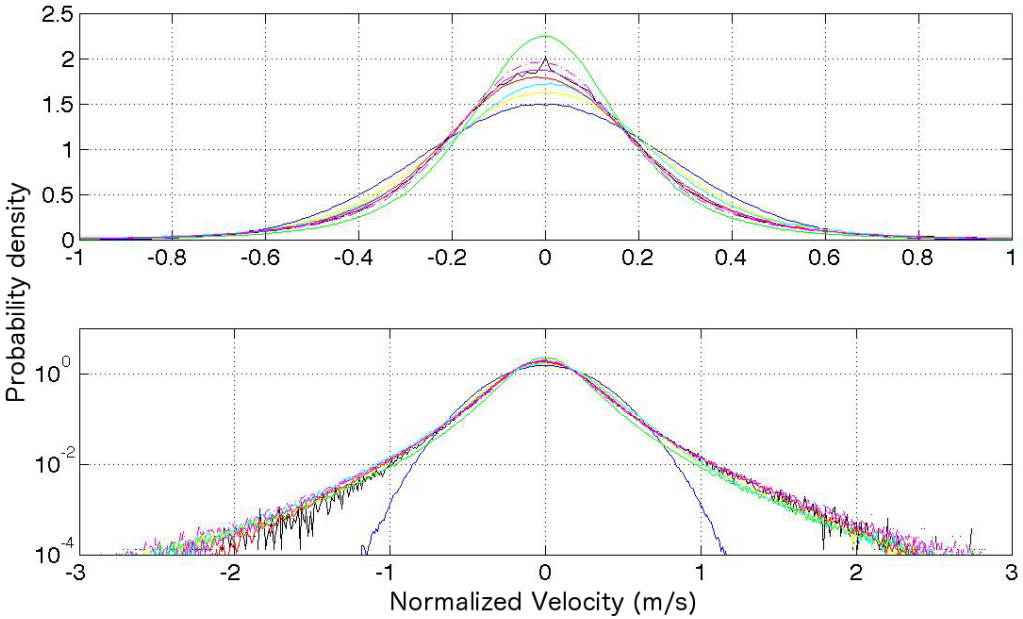

Figure 3.12: Distributions generated by the different configurations of the model for the surface zonal velocity, overlapped to the empirical distribution plotted in black. Velocities normalized in 2° square boxes. The following conditions are represented: local Gaussian velocities with mean and STD values equal to the global values (blue); inverse of the variance as a gamma function (green); Gaussian mean distribution (yellow); t-student mean distribution (cyan); introduction of the mean-variance correlation (red); local kurtosis = 4 (magenta); local kurtosis = 15 (magenta dashed). Modifications are additive to improve the model at each step.

3.9) leads to further improvements: the peak value is greatly reduced, reaching well below the observed values, and the adjustment to the tails improves slightly (Fig. 3.12).

The next step is to simulate the mean distribution by a t-Student with only 4 degrees of freedom (Fig. 3.9), with the purpose of increasing the kurtosis of the model mean distribution. This modification increases the PDF peak value, remaining smaller but closer to the real distribution (Fig. 3.12).

The next improvement is to use the empirical two-dimensional PDF, as a function of mean values and variance, to model the velocities

(Fig. 3.10). When this is introduced, the model distribution becomes very similar to the real distribution: The peak is a little low, but the tails have a really good fit (Fig. 3.12).

The last modification considers the local velocities to adjust to a t-Student distribution; by decreasing the number of degrees of freedom we increase the kurtosis and obtain a greater departure from Gaussianity (Fig. 3.11). In Figure 3.12 we include the results corresponding to two different t-Student distributions (9 degrees of freedom, kurtosis of about 4; 4 degrees of freedom, kurtosis of approximately 15). Raising the local kurtosis elevates the central part of the distribution, the best adjustment corresponding to 9 degrees of freedom. Despite the improved central fit, an increase in the local kurtosis also elevates the tails, leading to an overall reduced fit; actually, the best fit for the tails is achieved considering a local Gaussian distribution.

1000 dbar

We repeat the calculations for the parking velocities at 1000 dbar, maintaining the same configurations used for the sea surface (Fig. 3.13). The model does not get close to the real distribution until we establish a correlation between the local mean and the local variance, independently of the degrees of freedom chosen to model the distribution of the local mean. The fitting, however, is not as good as the one achieved for the sea surface velocities.

The local Gaussian assumption gives a reasonably good fit between the model and the data PDFs, especially when looking at the tails. It may be improved, however, if we replace the Gaussian distribution by a t-Student distribution with a low number of degrees of freedom. Choosing 2.4 degrees of freedom, which is equivalent to substantially increasing the local kurtosis (in the range of the hundreds), leads to an improved peak value but raises the tails. It is difficult to establish which case provides the best fit for the tails. In particular, the Gaussian assumption gives a reasonably valid approximation that cannot to be discarded.

The fact that a really high kurtosis is needed in the simulation for the 1000 dbar velocities to achieve a better fit may be due to noisier data in depth, but it might also be indicative of higher residual lateral inhomogeneities due to a lower turbulence spacial scale. Because

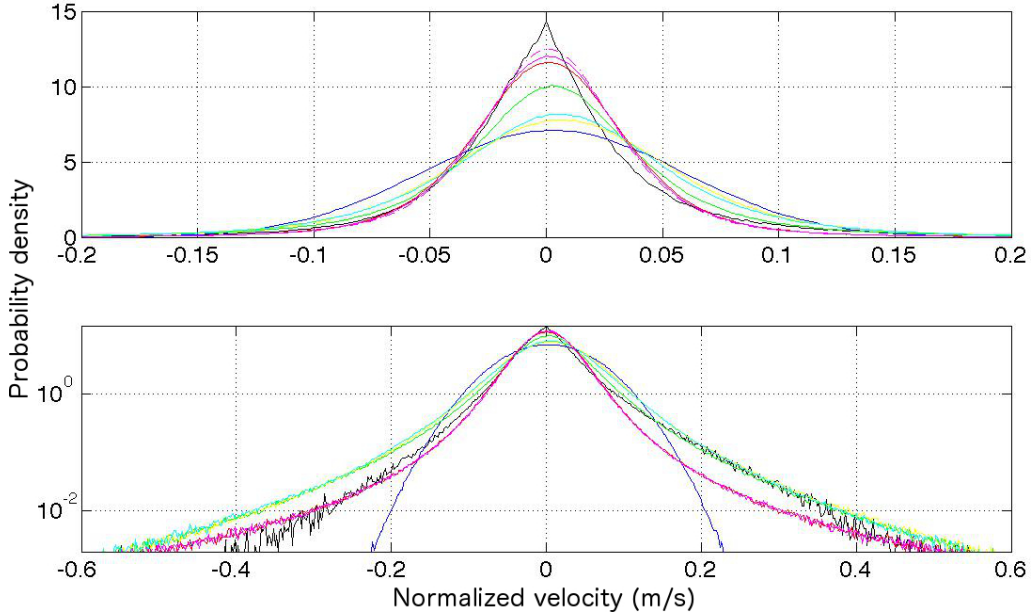

Figure 3.13: Distributions generated by the different configurations of the model for the 1000 dbar zonal velocity, overlapped to the empirical distribution (black line). The velocities correspond to the values locally normalized using 2°square boxes. The following conditions are represented: local Gaussian velocities with mean and STD values equal to the global values (blue); inverse of the variance as a gamma function (green); Gaussian mean distribution (yellow); t-student mean distribution (cyan); introduction of the mean-variance correlation (red); local kurtosis = 4 (magenta); local kurtosis = 15 (magenta dashed). Modifications are additive to improve the model at each step.

we have no data density enough to increase the resolution, we cannot explore the problem further. We expect as the data density will increase to be able to increase the resolution beyond 2°, and thus be able to further explore the local Gaussianity of the velocities at 1000 dbar.

The above considerations assume that the data has no instrumental error or bias. However, the observed PDFs may not be fully realistic because of sampling limitations; for example, it may be excessively peaked because of an overestimation of the low velocities related to limited spatial resolution associated

to satellite positioning.

3.4 Conclusions

Our initial analysis shows an important effect of bin size on the kurtosis of the global PDF distribution, the larger the region the greater the kurtosis as a result of lateral inhomogenities. Nevertheless, the global empirical distribution can be closely reproduced by assuming local Gaussian distribution for the ocean velocities, when parameters are properly chosen.

Our results show that, because of the contamination of the temporal variation and the residual lateral inhomogeneities, it is difficult to firmly conclude whether the ocean velocities are or are not locally Gaussian. In contrast with previous studies, our results suggest no evident departure from Gaussianity, as it depends on the spatial and temporal observational windows. The hypothesis of local Gaussian processes would be in agreement with the hypothesis of entropy maximization (Conrad, 2004; Lyon (2013), explored in appendix A.

Chapter 4

Zonal Jets in the Equatorial Atlantic Ocean

This chapter presents the study of the equatorial Atlantic Ocean based on the velocities inferred from Argo floats. We use position data from the Argo float program projected on a 1/2° grid, and smoothed out over 400 km × 200 km longitude-latitude domains, to investigate the zonal jet structure of the flow field at the sea surface and at three subsurface levels in the equatorial Atlantic Ocean. These levels correspond to Central Waters (CW, 200 m), Antarctic Intermediate Waters (AAIW, 1000 m) and upper North Atlantic Deep Waters (uNADW, 1500 m). At all levels the annual-mean fields exhibit narrow zonal jets (typically 3° wide), with directions that alternate in latitude and with maximum speeds about 0.5 m s^{-1} at the surface, 0.1 m s^{-1} at CW and uNADW, and 0.03 m s^{-1} at AAIW.

The amount of available data also allows exploring the seasonal variability of the zonal jets at the sea surface and AAIW levels. We find a dominant annual cycle at both depth levels, with the sea surface jets changing intensity and the AAIW ones reversing direction at any given latitude. At the sea surface the annual and monthly averaged jets display similar gross characteristics but at the AAIW level the seasonal anomalies predominate. Time-averaging of the AAIW seasonally reversing currents leads to annual jets much thinner (about 2° instead of 4° in latitude) and slower (about 0.03 m s^{-1} instead of 0.05 m s^{-1}) than the seasonal ones. The intense seasonal AAIW anomalies appear to be associated to westward propagating planetary waves centred at about 3°S, 0°, 3°N.

The concept of a Global Overturning Circulation (GOC) is reviewed in section 4.1 and the state of the art for the equatorial Atlantic Ocean is presented in section 4.2. In section 4.3 we briefly refer to the data sets used for our study, including a brief description of the method used

Rosell-Fieschi, M., Pelegrí, J.L., Gourrion, J., 2013. Zonal Jets in the equatorial Atlantic Ocean. Submitted to Progress in Oceanography.

to infer the velocity fields from the Argo float data. Section 4.4 presents the annual-mean velocity fields at four different depths. The core of the chapter refers to the seasonally and spatially varying currents at the sea surface (section 4.5) and near the AAIW level (section 4.6). Both these sections present a harmonic analysis at annual and semi-annual frequencies; at the surface the currents are compared with the evolving spatial and temporal patterns of atmospheric forcing, at the AAIW level the analysis focuses on the presence of westward propagating Rossby waves. We wrap up with the most relevant conclusions in section 4.7.

4.1 The Global Overturning Circulation

Density-driven deep water formation at high latitudes sets the start of the GOC; other common names for the GOC are the Meridional Overturning Circulation (MOC), the global thermohaline circulation and the conveyor belt (after Broecker, 1991) (Fig. 4.1). The GOC is responsible for the recirculation of waters along the global ocean. It begins when the cold and saline surface waters sink during their respective winter time in both subpolar regions of the Atlantic Ocean, and ends as old intermediate waters reach back to the surface of the ocean, either through upwelling of Southern Ocean waters near the Antarctic continent or as these waters approach the surface equatorial Atlantic Ocean. The initial stages of the GOC are relatively well studied; contrarily, its ending is a more subtle and poorly understood process.

The Argo salinity and temperature data along 30°W may be used to illustrate the principal near-surface and intermediate water masses present in the tropical Atlantic, in particular the way the Antarctic waters reach back into the Atlantic Ocean towards the equatorial region. Figure 4.2 illustrates the raising of subAntarctic Mode Waters (sAMW) and AAIW in the tropical Atlantic, identified as waters of relatively low salinity (Talley, 1996; Schmid et al., 2001, 2003).

In this chapter we will use the Argo data to infer the horizontal velocity fields at different depths in the equatorial Atlantic Ocean. This will not give information about the vertical motions but it will indeed illustrate the sort of horizontal recirculation paterns the water parcels undergo before reaching the sea surface and, once there, before arriving to the western

boundary currents, which are the only effective way for inter-hemispheric water transport.

The signal of AAIW weakens beyond the equator and becomes most diluted between 12°N and 17°N. Most AAIW is found along the western margin, where it reaches beyond 25°N (Talley, 1996), although a more diluted form has also been detected to propagate until relatively high latitudes (beyond 30°N) along the eastern margin (Machín and Pelegrí, 2009). The existence of wind-induced equatorial divergence helps to sustain the mixing and upwelling of intermediate waters at the equator (Gouriou and Reverdin, 1999; Castellanos et al., 2014).

As Antarctic waters reach the equatorial Atlantic Ocean, they become trapped by an intense system of zonal jets. These jets take place at all depths, with different intensity and variability, and constitute the main mechanism for the distribution of water masses, in particular the connection of subsurface and surface waters in the central and eastern equatorial Atlantic Ocean with the western boundary region; only there, initially through the North Brazil Current (NBC), may the waters of Antarctic origin eventually reach back through the North Atlantic subtropical gyre and into the subpolar regions before being susceptible to be deep-convected, once again, as NADW.

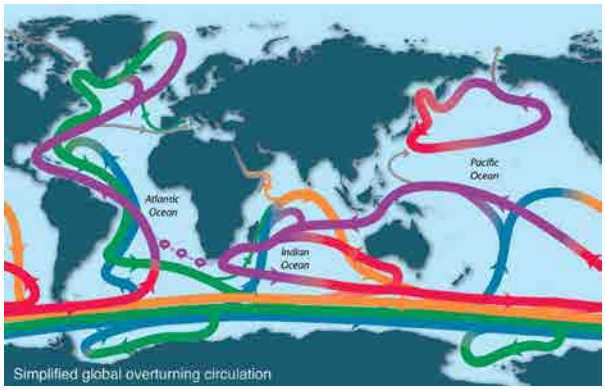

Figure 4.1: Schematics of the Global Overturning Circulation. Purple = upper ocean and thermocline. Red = denser thermocline and intermediate water. Orange = Indian Deep Water and Pacific Deep Water. Green = North Atlantic Deep Water. Blue = Antarctic Bottom Water. Gray = Bering Strait components and Mediterranean and Red Sea inflows. Updated from Talley et al. (2011), based on Schmitz (1995), Rahmstorf (2002), and Lumpkin and Speer (2007).

4.2 The equatorial Atlantic Ocean

The equatorial oceans are characterized by the vertical and latitudinal staggering of eastward-westward currents. The presence of a complex pattern of alternating zonal currents, at surface and subsurface depths, was first observed through acoustic dropsondes in

the Indian (Luyten and Swallow, 1976) and Pacific (Eriksen, 1981; Hayes and Milburn, 1981) oceans, and later in the Atlantic Ocean (Ponte et al., 1990; Send et al., 2002). The Atlantic equatorial system has been studied assuming near-geostrophic balance (Eriksen, 1982) but near the equator geostrophy fails and the description requires direct velocity measurements, such as from instrumented moorings (Send et al., 2002; Brandt et al., 2006; Bunge et al., 2006, 2008), ship-borne Acoustic Doppler Current Profilers (ADCP) and Lowered-ADCP (LADCP) (Send et al., 2002; Gouriou et al., 1999, 2001; Brandt et al., 2006), acoustically tracked buoys (Richardson and Fratantoni, 1999), profiling floats (Schmid et al., 2001), and a combination of both acoustic buoys and profiling floats (Ollitrault et al., 2006; Lankhorst et al., 2009).

The first descriptions of zonal jets in the equatorial Atlantic dealt with the near-surface structures. The predominant surface current is the westward flowing Southern Equatorial Current (SEC), the rather wide northern branch of the South Atlantic subtropical gyre. This current is reported to be composed of several, poorly differentiated, branches: the central (cSEC, about 3 to 5°S), equatorial (eSEC,

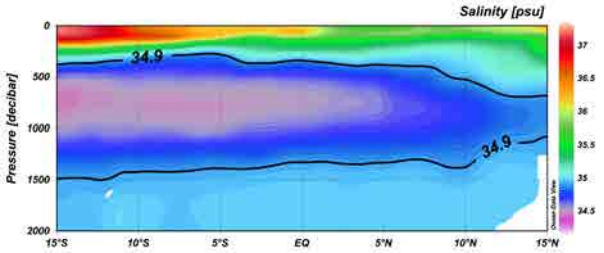

Figure 4.2: Salinity distribution on a meridional section produced using data from all available Argo profiles between 31 and 29°W. Waters fresher than 34.9 correspond to intermediate waters, on top we find the central waters and below the deep waters.

near the equator when present) and northern branches (nSEC, about 2 to 4°N), all merging into the NBC (Stramma and Schott, 1999).

The North Equatorial Counter Current (NECC), the major surface zonal jet in the tropical Atlantic, is characterized by a strong annual cycle related to the latitudinal displacements of the Inter Tropical Convergence Zone (ITCZ) (Garzoli et al., 1982; Merle and Arnault, 1985; Richardson and Walsh, 1986; Arnault, 1987; Richardson et al., 1993; Urbano et al., 2006, 2008). This current is found between the sea surface and depths of about 350 m; it is usually located between 4 and 8°N (with a northern branch reaching up to 10°N in fall), north of a zonal band of maximum positive sea

surface height values. Its transport ranges between non-significant winter values and summer-fall maxima in the western margin, close to 40 Sv (Carton and Katz, 1990). Several authors have reported the NECC to have a double-core structure in the western Atlantic, which is best defined in the western margin during summer and fall, at times when the current intensifies and is displaced north following the ITCZ (Richardson and McKee, 1984; Richardson and Reverdin, 1987; Didden and Schott, 1992; Polonsky and Artamonov, 1997; Bourlès et al., 1999; Urbano et al., 2006, 2008; Hormann, 2012).

Other major zonal currents are observed at subsurface levels, flowing east under the wind-driven westward SEC. These are the Equatorial Undercurrent (EUC), centered at the equator and 100 m depth, and the off-equatorial South/North Equatorial Under Current (SEUC/NEUC), centered at some 150 to 200 m and 4°N/4°S (e.g. Metcalf et al., 1962; Tsuchiya, 1986 ; Stramma and Schott, 1999). The EUC feeds from the retroflection of the NBC, typically as a very tight loop near the equator (Flagg et al., 1986, Schott et al., 1998; Hüttle-Kabus and Böning, 2008). The strenght of the EUC decreases as it flows east, with a maximum transport of about 20 Sv, while there are fewer reports on the spatial variation of the northern and southern branches (Gouriou and Reverdin, 1992; Bourles et al., 1999; Schott et al., 2002; Brandt et al., 2006; Hüttl-Kabus and Böning, 2008).

Several authors have shown that the zonal jets are also found far from the sea surface in the equatorial Atlantic (Gouriou et al., 1999, 2001; Richardson and Fratantoni, 1999; Bourlès et al., 2003; Schott et al., 2003; Brandt and Eden, 2005; Brandt et al., 2006). The circulation schemes by Stramma and Schott (1999), amended by Schmid et al. (2003) for intermediate waters, indeed emphasized the predominance of zonal jets at deep levels in the equatorial Atlantic region. Equatorial Deep Jets (EDJ), trapped between 2°S and 2°N, are found at depths between 300 and 2500 m. These jets have a meridional scale of only 1° and display alternating directions on vertical distances of 400 to 600 m, with maximum velocities about 0.2 m s^{-1}. Their vertical structure is quite consistent through one same season but changes with season. The EDJs are surrounded by eastward columns of Extra Equatorial Jets (EEJs), sometimes named subsurface countercurrents (after

Tsuchiya, 1986), located at about 2 or 3°S/N and extending from as shallow as 200 m down to near the sea floor. The EEJ velocity cores are found at the depth of the westward EDJs (about 500 m), suggesting elongated recirculation gyres as in the Pacific (Firing et al., 1998). Hüttle-Kabus and Böning (2008) argued the eastward EEJs feed on the subtropical cell via tropical instability waves from the EUC; these authors found that these flows are dominated by an annual and, to a lesser degree, a semiannual harmonic.

The introduction of Lagrangian buoys has substantially enhanced our skill to observe the horizontal coherence of the equatorial jets at several depths. Ollitrault et al. (2006) used acoustic drifter data near 800 m and profiling floats near 1000 m to describe the presence of a system of rather narrow zonal jets, changing direction about every 2° in latitude: westward South Equatorial Intermediate Current SEIC (4°S), eastward Southern Intermediate Counter Current SICC (2°S), Equatorial Intermediate Current EIC (0°), eastward Northern Intermediate Counter Current NICC (2°N), and westward North Equatorial Intermediate Current NEIC (4°N). According to Ollitrault et al. (2006), only the EIC reverses sign with season, westward in fall and eastward in winter.

Lankhorst et al. (2009) combined Argo float and acoustic drifter data within intermediate (600 to 1050 m) and upper-deep (1200 to 2050 m) layers to look at the interaction between boundary and zonal flows. At intermediate levels the northward flowing North Brazil Under Current (NBUC), which extends from under the surface mixed layer down to 1000 m (Stramma et al., 1995), appears to be one main source for the eastward NICC and SICC, possibly aided by the recirculation of the westward flowing NEIC and SEIC. At the upper-deep level the southward-flowing DWBC decreases in intensity as it interacts with the interior zonal flows (Lankhorst et al., 2009).

In November 2007 the Argo program achieved its goal: over 3000 simultaneous profiling floats in the Global Ocean that drift at several depths and perform over 100,000 profiles per year, with a mean resolution of about one profile per year in a 60 km × 60 km grid. Presently, the dataset is large enough to map mean velocity fields at several water depths and even to examine the seasonal variability at surface and intermediate layers. In this study we use the

equatorial and tropical Atlantic Argo data to describe the equatorial current system at four different levels (the sea surface and three additional drifting levels). The results confirm the existence of the zonal current system and give further insight into its spatial distribution, as well as its seasonal variation at the surface and intermediate levels.

4.3 Data set and methods

4.3.1 Argo-inferred velocities

Several studies have focused on obtaining an Argo-derived velocity data base (Ollitrault et al., 2006; Lebedev et al., 2007). Here we use a simple approach to produce our own data set, generating velocity fields at the surface and at several parking depths. Only data flagged as good in the trajectory data (both for POSITION_QC and JULD_QC) are considered and the parking pressure contained in the float's metadata file is used as the real drifting depth, neglecting possible differences (approximately 4% of the time) between the real parking depth and the parking depth given by the metadata file (Ollitrault et al., 2013). The procedure infers the surface and parking-depth velocities from the first and last transmission while a float remains at the sea surface. As a result we generate one surface and one deep velocity vector per cycle; in contrast, Ollitrault et al. (2013) generate two surface velocity vectors by using an intermediate position.

The surface velocity estimates are only limited by the accuracy in the positioning system errors. The subsurface velocity estimates, on the other hand, contain additional errors arising from (a) the drift experienced by the float during both ascend and descend profiling phases and (b) the time lag between the times when the float reaches (leaves) the sea surface and the next (last) transmission time.

Once we have the surface and parking-depth velocities, we may obtain simple estimates for both the drift and lag-time errors. The drift error is estimated as the difference in the float's displacement while moving at the parking depth and its actual displacement when experiencing a different velocity field during both ascend and descend phases. The error is calculated simply as an ascend-plus-descend time multiplied by the vector difference between surface and parking-depth (cell-mean) velocities. The assumption of a linear velocity change with depth,

from the sea surface to the parking depth, is a gross idealization, especially when the profilers, during their vertical migrations, cross flow structures independent from those observed at surface and parking depth. The errors related to the time lags between the surfacing/sinking and first/last transmitting times are estimated from a limited number of instances (about 10% of the cases) where the arrival and and departure times are available.

The estimated velocity errors are typically just a fraction of the velocity standard deviation, as calculated from all velocity vectors used to compute the mean values at each grid point, and one order of magnitude smaller than the parking depth mean velocities. These values are in good agreement with Lebedev et al. (2007), whom indicate that the relative mean velocity error at the parking pressure (error-to-velocity ratio) is only 3%, with 54% of the deep velocity data having relative errors less than 10% and nearly 98% of the data having absolute velocity errors smaller than the mean calculated velocity value. These results grant high confidence on the procedure used to determine the velocity fields.

The whole Argo dataset up to September 2013, between 20°S and 20°N, and 75W and 15°E is examined. Nine different parking depths are found in the equatorial Atlantic (200, 250, 300, 400, 1000, 1100, 1500, 1900 and 2000 dbar), but here we have ignored those depths with a relatively scarce number of floats (250, 300, 400 and 1100 dbar) or where floats are localized in some constrained region (floats at 1900 and 2000 dbar are mostly found near the African coast). Therefore, we use all floats to calculate the surface drift but choose only three parking depths to generate the sub-surface velocity fields, obtaining the following amount of velocity vectors: surface waters, all floats (SW, 57413 vectors); central waters, floats at 200 dbar (CW; 3314 vectors); intermediate waters, floats at 1000 dbar (AAIW, 44308 vectors); and upper North Atlantic Deep Water, floats at 1500 dbar (uNADW, 3449 vectors).

The Argo salinity and temperature data may be used to illustrate the principal near-surface and intermediate water masses in the tropical Atlantic. Figure 4.2 shows the salinity distribution on a meridional section from 15°S to 15°N, drawn using the data from all available Argo profiles between 31 and 29°W. The presence of AAIW in the tropical Atlantic, defined

as corresponding to waters of salinity less than 34.9 (Talley, 1996), clearly separates the upper-thermocline CW from the relatively deep uNADW. AAIW is located between about 400 and 1200 dbar with its core at some 800 dbar (Talley, 1996; Schmid et al., 2001, 2003). For this reason the floats at 1000 dbar do not sample the core of AAIW but rather its lower part.

The first step is to estimate individual velocity values for all available Argo data between 20°S and 20°N and between 75°W and 15°E. The next step is to remove those extremely high velocities, with a relatively high probability of being spurious values. Our analysis of the Argo-inferred velocities in the equatorial Atlantic Ocean shows the existence of potentially long tails in the PDFs related to real extreme events (chapter 3). Therefore, we have used a criterion of six standard deviations as a compromise between not removing a significant number of high-velocity events and the need of eliminating very high spurious values. This criterion approximately corresponds to velocities greater than 1.5 m s^{-1} and 0.5 m s^{-1} at the surface and 1000 dbar, repectively. It is a criterion less restrictive than the threshold values imposed by Ollitrault et al. (2006), 3 and 2 m s^{-1} respectively for the surface and 1000 dbar levels, and yet plenty satisfies the commonly used Chauvenet's criterion (Taylor, 1997).

Finally, once the individual velocities are obtained, in order to calculate the time-averaged velocities, we use a 0.5° latitude-longitude resolution grid and assign to each grid cell all velocity vectors contained in an ellipse with a zonal major axis of 400 km and a meridional minor axis of 200 km. This asymmetry is consistent with the larger zonal than latitudinal coherence of the flow field in the tropical Atlantic (Stramma and Schott, 1999). After removing the land cells, the 0.5° grid produces a total of 8660 cells at the sea surface and 8178 cells at 1000 dbar; the above procedure renders a spatial smoothed version, approximately over 4° in longitude and 2° in latitude, with a total number of velocity vectors for each cell ranging between about 100 and 300 (Fig. 4.3).

The available amount of data is excellent for calculating annual-mean values but, as over 64% of the data has been collected since 2008 (by September 2013), it is not adequate to examine spatial patterns of inter-annual variability. Nevertheless, the combination of data from all years does allow producing a climatological year

for each grid point at the surface and AAIW levels. We have explored using many different temporal intervals, e.g. a several-month running window, and have arrived to the conclusion that the available data is adequate to produce simple monthly velocity values. The mean number of velocity vectors per cell and month is 11.1 at the sea surface and 8.9 at 1000 dbar. This relatively large number of monthly velocity values is the result of the relatively large spatial integration. It allows focusing on the seasonal variability of basin-scale features but prevents from studying relatively fast processes, with time scales of the order of one month or less, or mesoscale process, with spatial scales of 100 km or less.

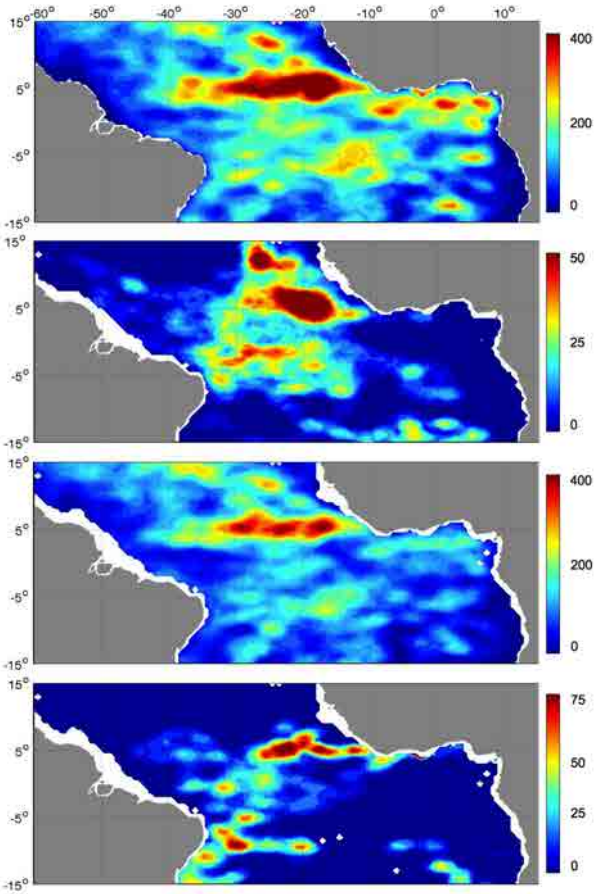

Figure 4.3: Number of velocity profiles assigned to each 0.5° latitude-longitude cell. From top to bottom: surface, CW (200 dbar), AAIW (1000 dbar), uNADW (1500 dbar).

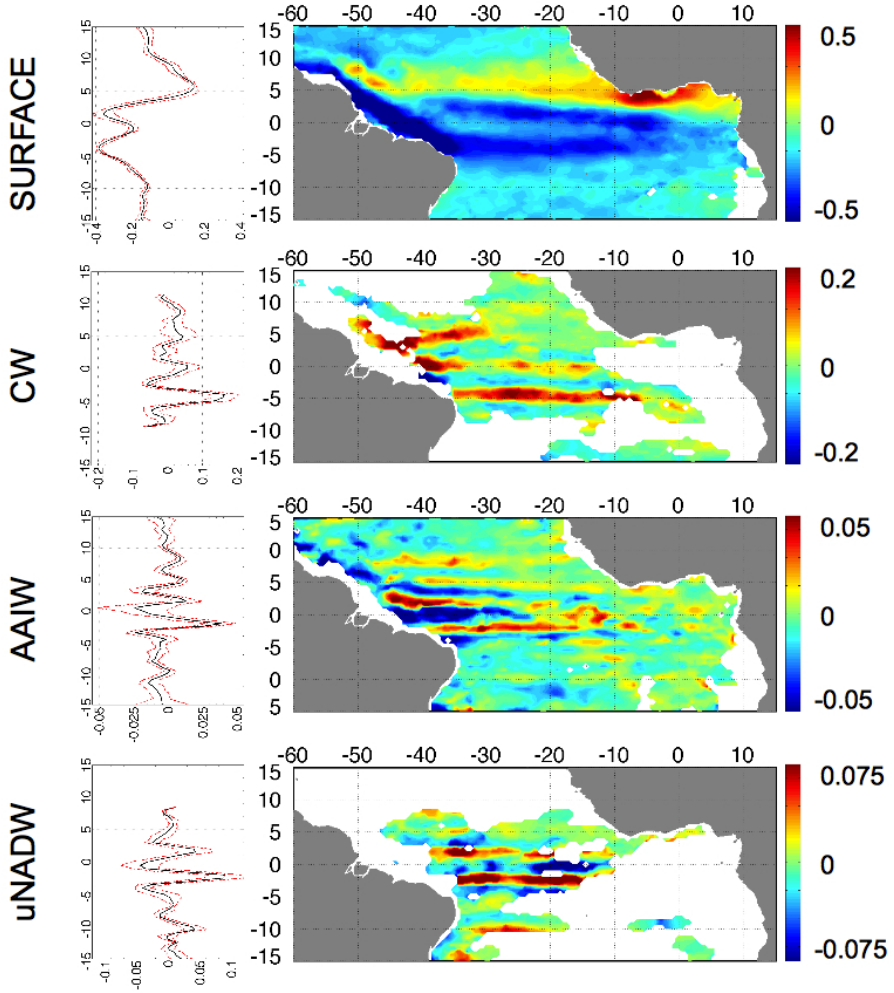

Figure 4.4: Contour maps for annual-mean zonal velocities (m s^{-1}) at surface (top), CW (second row), AAIW (third row) and uNADW (bottom) levels. Note the change in scale between the top and bottom panels. Each panel is accompanied by a box that shows the latitudinal distribution of the zonally-averaged (33 to 20°W) zonal velocity as a function of latitude (black line). The dashed red lines show one standard deviation as calculated using the cell-mean values (0.5° latitude grid) between 33 and 20°W.

4.3.2 Monthly wind fields

The sea-surface atmospheric circulation in the equatorial Atlantic is characterized from monthly WindSat products (www.remss.com/missions/windsat). The wind corresponds to a standard height of 10 m, obtained over a 2°latitude-longitude grid. A monthly climatology is obtained using data from 2005 to 2012, corresponding roughly to a time period when most of the Argo data was acquired. Separately, the monthly location of the ITCZ is digitized from the plots presented in Hastenreth and Merle (1987).

4.4 Mean velocity fields at four depth levels

Figure 4.4 presents annual-mean maps for the zonal velocity at all four depth levels. Aside each map we present boxes with the latitudinal distribution of the zonal velocities, calculated for each 1/2° latitude interval by averaging all cell-mean values between 33 and 20°W as in Ollitrault et al. (2006). The standard deviation shows to be substantially smaller than the mean values and renders the zonal coherence of the mean fields in the western Atlantic Ocean.

At all levels we find zonal jets which have zonal continuity over most of the Atlantic Ocean and alternate direction with latitude, corresponding to what is reported in the literature (Table 4.1). The annual-mean meridional velocities (not shown) have amplitudes substantially smaller than the zonal ones, particularly in the subsurface levels, and have little spatial coherence. The only major exception is the NBC which flows as a relatively narrow northwestward surface flow along the northern coast of Brazil, connecting waters from the southern and northern hemispheres. In the annual mean meridional velocity field also the meridional transport associated to the connection between the nSEC and the NECC is visible (Fig. 4.10).

The annual-mean fields reproduce all major known equatorial Atlantic Ocean currents at the different levels. At the surface, the annual-mean zonal flow is dominated by the northern and central branches of the westward SEC close to the equator and by the NECC further north (Fig. 4.4, Table 4.1). The signal of the NBC is also visible in the zonal velocity maps as an intense westward current. These surface currents are wide, about 4° in latitude, and permanent all

year long except the NECC which intensifies in summer.

In contrast to the relatively wide surface currents, the annual-mean and zonally-averaged (33 to 20°W) CW, AAIW and uNADW flows display a complex pattern of rather narrow currents and counter-currents (Fig. 4.4, Table 4.1). In particular, despite the differences in the amount of Argo data, the jets at AAIW compare reasonably well with the 33 to 20°W averaged zonal jet system reported by Ollitrault et al. (2006); however, the AAIW annual-mean jets display zonal continuity only in the western Atlantic, as the zonal pattern disappears east of about 23°W.

We will see in next section that this average field is an artefact resulting from the seasonal averaging, as the seasonal jets at the AAIW level are substantially wider and swifter than the annual-mean stream. On the other hand, at the CW and uNADW levels, the mean zonal flow is remarkably continuous across the whole Atlantic Ocean, with no significant changes in direction with longitude. It is possible that the CW and uNADW have indeed such a complex system of instantaneous zonal jets but we have no way to assure this from the available data.

4.5 Surface velocities

4.5.1 Seasonal variability

The monthly surface velocity fields illustrate the seasonal evolution of the northern, equatorial and southern branches of the SEC (Fig. 4.5). The core of the cSEC is located all year long near 4°S, with mean velocities of about 0.2-0.4 m s^{-1}. The maximum westward velocities occur in May-June and the minimum ones in October-November. The maps in Figure 4.5 show the existence of variations of about 0.2 m s^{-1}, associated to a 12-month period. The latitudinal location is rather constant all year long, centred near 4°S.

The eSEC and nSEC flow relatively close to the equator with characteristic speeds of 0.3-0.4 m s^{-1}. In the central part of the equatorial Atlantic (30°W-20°W), a minimum velocity (0.2 m s^{-1}) is observed in March and a maximum (0.6 m s^{-1}) in June, in phase with the northward displacement of the ITCZ. Similar minimum/maximum values occur about one month earlier near 5°W and one month later near 35°W.

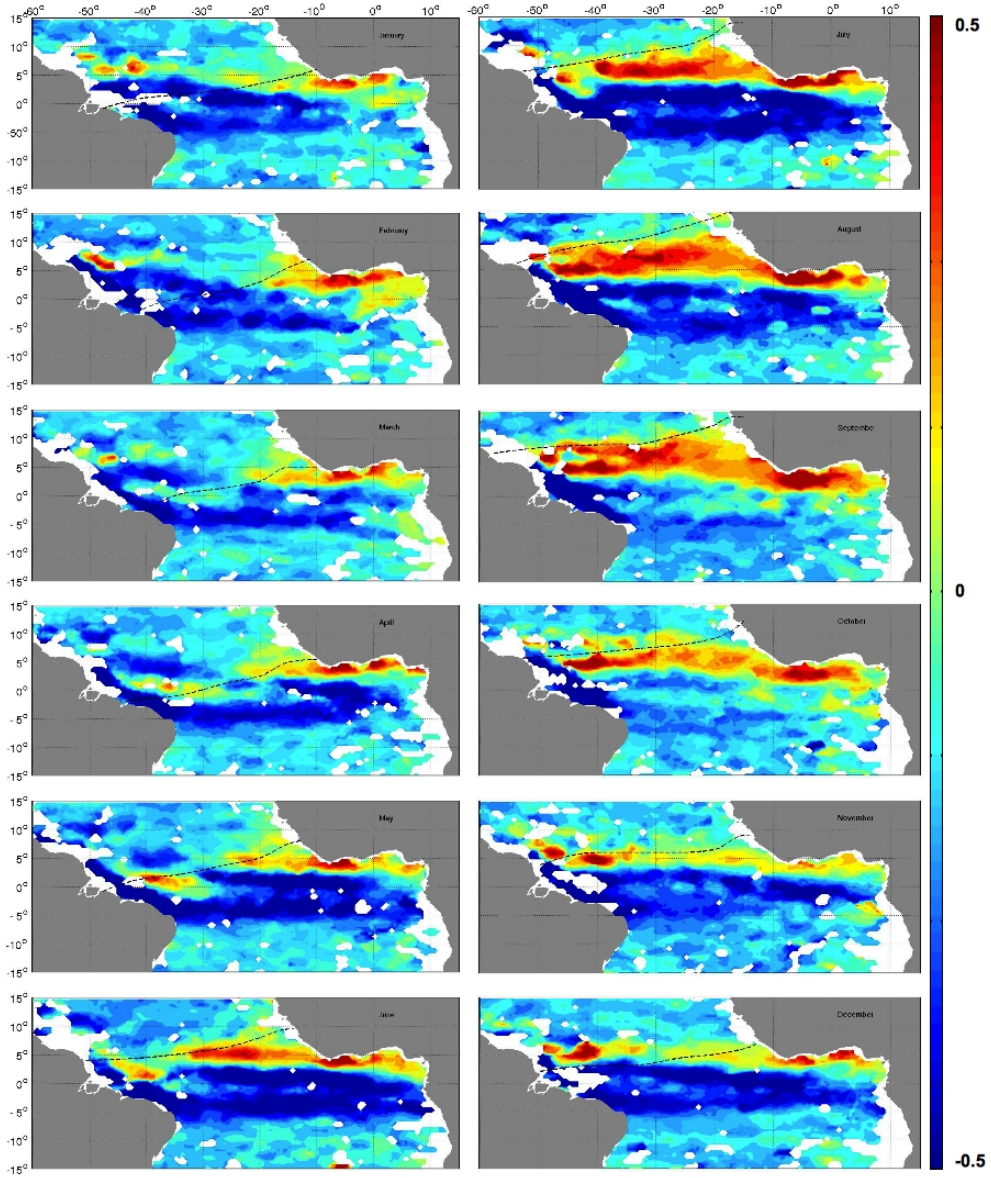

Figure 4.5: Contour maps for zonal velocities at the surface (m s^{-1}), calculated as 1-month averages.

In the eastern basin, the variation in intensity is accompanied by a latitudinal displacement of the flow core, typically located near 1°N but shifting to 1°S in November. In the western basin, the flow core is located near 1-2°N most of the year but is shifted to 4-5°N in April. It is interesting to note that this northern shift in the western basin is associated to the appearance of an eastward flow between 2°S and 3°N, typically associated to the surfacing of the EUC (Urbano et al., 2008). A secondary oscillation in the intensity of the nSEC is barely visible, corresponding to a minimum value in September-October and maximum one in December-January. Another major feature is the quasi-permanent eastward flow found east of 15°W and between 4 and 7°N, along the African coast: the Guinean Current. The monthly maps show that, in phase with the northward migration of the ITCZ and the intensification of the westward nSEC flow, the Guinean Current gradually extends northward and westward from May to September, forming the North Equatorial Counter Current (NECC) and ultimately connecting with the NBC retroflection (Fig. 4.5). With the progressive southward shift of the ITCZ, between October and February, the NECC gradually weakens and disappears in April, accompanied by a northward shift of the nSEC.

In order to assess the amplitude and phase of the annual and semi-annual periodicities, we have carried out a classical harmonic analysis of the zonal and meridional velocity components (appendix C). The analysis confirms a mean westward velocity of about 0.3 m s^{-1} (top panel of Fig. 4.4), with semi-annual variations close to 0.25-0.3 m s^{-1} in the central equatorial Atlantic (30°W-20°W) and substantially higher (as much as 0.5 m s^{-1}) in the western basin (Fig. 4.6). These high amplitudes of the seasonal signal, larger than the mean values, are consistent with the observed annual flow reversal (Fig. 4.5). The contribution of the semi-annual signal is smaller than the annual one everywhere except in a near-equatorial band, between about 2°S and 4°N and 5 and 30°W (bottom panels of Fig. 4.6); a secondary band of significant semi-annual amplitudes is centred between 6 and 8°N, west of 30°W.

The phase distribution suggests the existence of different latitudinal bands (center panels, Fig. 4.6). Consider first the northernmost band, roughlty between 4 and 10°N. The phase for the annual component is uniform across the

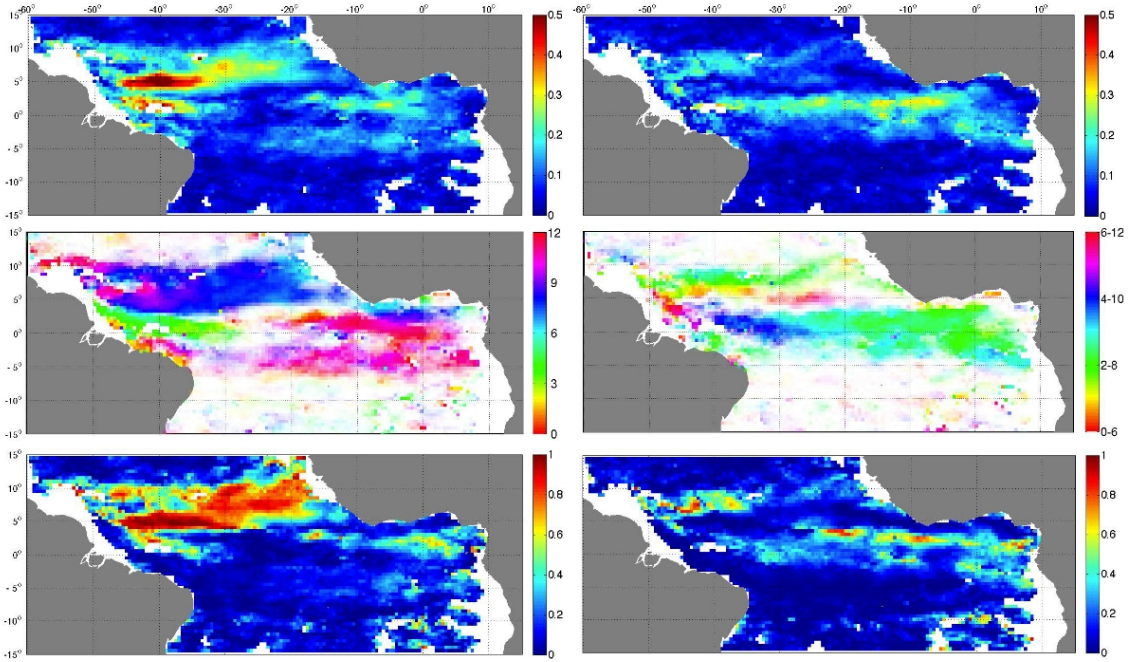

Figure 4.6: Amplitude (top) and phase (center) for the annual and semi-annual components of the zonal surface velocity (m s^{-1}); a transparency mask (quadratic proportion to amplitude) has been applied to the phase distributions in order to emphasize those areas with high amplitudes. The bottom panels illustrates the variance explained by either contribution.

whole tropical North Atlantic Ocean, with maximum eastward velocities in August. The phase for the semiannual component is also rather constant over the same tropical region, with maximum eastward velocities in February/August at about 8°N and June/December at about 5°N. The next band is roughly centered at 2°N, with the maximum annual and semiannual variability taking place at the western and eastern margins. In the western region the maximum eastward currents occur in April (annual) and in April/October (semiannual), while in the eastern region they correspond to November (annual) and February/August (semiannual). Fi-

nally, in the central and eastern portions of the southernmost band (roughly along 4°S) the annual contribution is most significant; the phase for the maximum eastward contribution (giving rise to the minimum westward velocity) corresponds to October-November.

The bottom panels of Figure 4.6 illustrate the variance explained by each contribution. The annual signal explains most of the variance in the region between the southernmost and northernmost positions of the ITCZ. In contrast, the explained variance for the semiannual signal is largest near the equator and has low relevance in the extra-equatorial dynamics. The semiannual signal clearly draws the two branches of the SEC (nSEC and cSEC).

4.5.2 Time-latitude variations at three selected longitudes

The results of the harmonic decomposition are consistent with the harmonic analysis of velocity data done by Richardson and Walsh (1986) using ship drifts and Lumpking and Garzoli (2005) using surface drifters. The high level of agreement between these two analyses, using data sets of different origin and spatial resolution, evidences the robustness of the annual and semi-annual changes. In order to better understand the mechanisms that bring out the annual and semi-annual oscillations, we will examine the changes of the surface winds and currents at three different longitudes: 5, 25 and 33°W.

Consider first the temporal changes in surface wind and ocean velocity at 25±1°W, in the central Atlantic (center panels in Fig. 4.7). The ITCZ shifts from 2°N in February-March to 12°N in August. As a result, the northeastern (southeastern) trade winds blow during the boreal winter (summer) between 2°N and 10°N, producing two wind speed maxima per year. This leads to the existence of a semi-annual wind forcing between 2°N and 10°N.

The response of the surface currents to the zonal band of semi-annual wind forcing (2 to 10°N) is quite different depending on the latitude. The most clear response appears at 2-3°N, near the southern limit of the semi-annual wind forcing. Further north, up to at least 10°N, the zonal currents are dominated by a annual, somewhat distorted, signal.

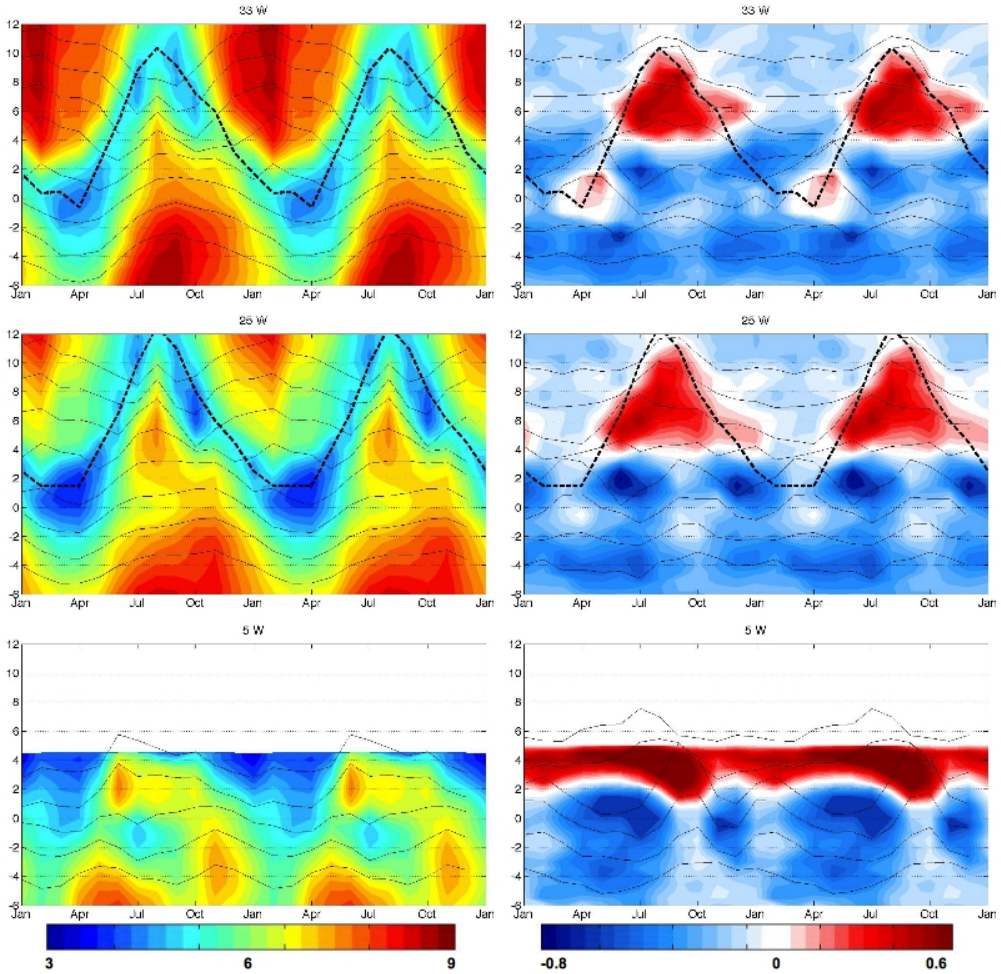

Figure 4.7: Time-latitude plots for (left panels) the magnitude of the surface winds (m s^{-1}) and (right panels) the zonal surface-ocean velocities (m s^{-1}). The results correspond to zonally-averaged (33 to 20°W) values at three longitudes, calculated using data within 1°: (top) 33±1°W, (center) 25±1°W, and (bottom) 5±1°W. The climatological latitudinal location of the ITCZ at each longitude, as calculated by Hastenrath and Lamb (1977), is shown as a thick dashed line. The thin dashed lines illustrate the temporal variation in the amplitude of the anomalies at the different latitudes (every 2°). In order to emphasize the predominant periodicities, two full climatological years are shown.

Between 4 and 10°N the eastward NECC appears at the time of the ITCZ northernmost extension, when the westward winds reach their minimum values (Fig. 4.7). The deformation of the annual wind cycle is the likely reason for the appearance of a weak, yet significant, semi-annual signal in the surface NECC (Fig. 4.6).

Strikingly, the semi-annual signal in the zonal surface currents extends until 2°S, well beyond the southernmost limit in the semi-annual forcing (2°N). The semi-annual sea-surface response in the equatorial band, between 2°S and 2°N, is characterized by the intensification of the westward currents in June and September, and its slowing (down to zero) in April and October. The April weakening of these equatorial westward currents is clearly related to the southernmost extension of the ITCZ and the associated decline in the westward winds (Fig. 4.7, left panels). The October weakening, however, is harder to explain as it occurs during a period of relatively intense winds.

The summer intensification of the NECC, up to a maximum in August and September, coincides with a decline in the intensity of the westward winds (the ITCZ moves to these latitudes) and a progressive decrease in the intensity of the nSEC (between about 0 and 4°N) (Figs. 4.5 and 4.7). It also points at the lagged, a couple of months later, decrease in the cSEC (between about 5°S and the equator). These changes coincide with the times of maximum westward winds just north (August) and south (November) of the equator (center left panel, Fig. 4.7).

The existence of a semi-annual surface current in the equatorial band (as far south as 2°S) together with the annual evolution of the nSEC-NECC system points at the potential importance of indirect wind forcing through meridional Ekman transports. We will come back to this issue in the next subsection.

Consider finally the surface winds and ocean velocities in the eastern (5±1°W) and western (33±1°W) Atlantic (Fig. 4.7). In the western basin the situation is similar to the one described for 25°W, although the semi-annual component in the equatorial band is substantially weaker (Fig. 4.7). In the eastern basin the predominant changes in the intensity of the nSEC are annual, yet a swift southward September-October migration of the Guinea Current locally enhances the eastward zonal velocity and leads to an increase of the semi-annual harmonic component amplitude in this region (Fig. 4.6).

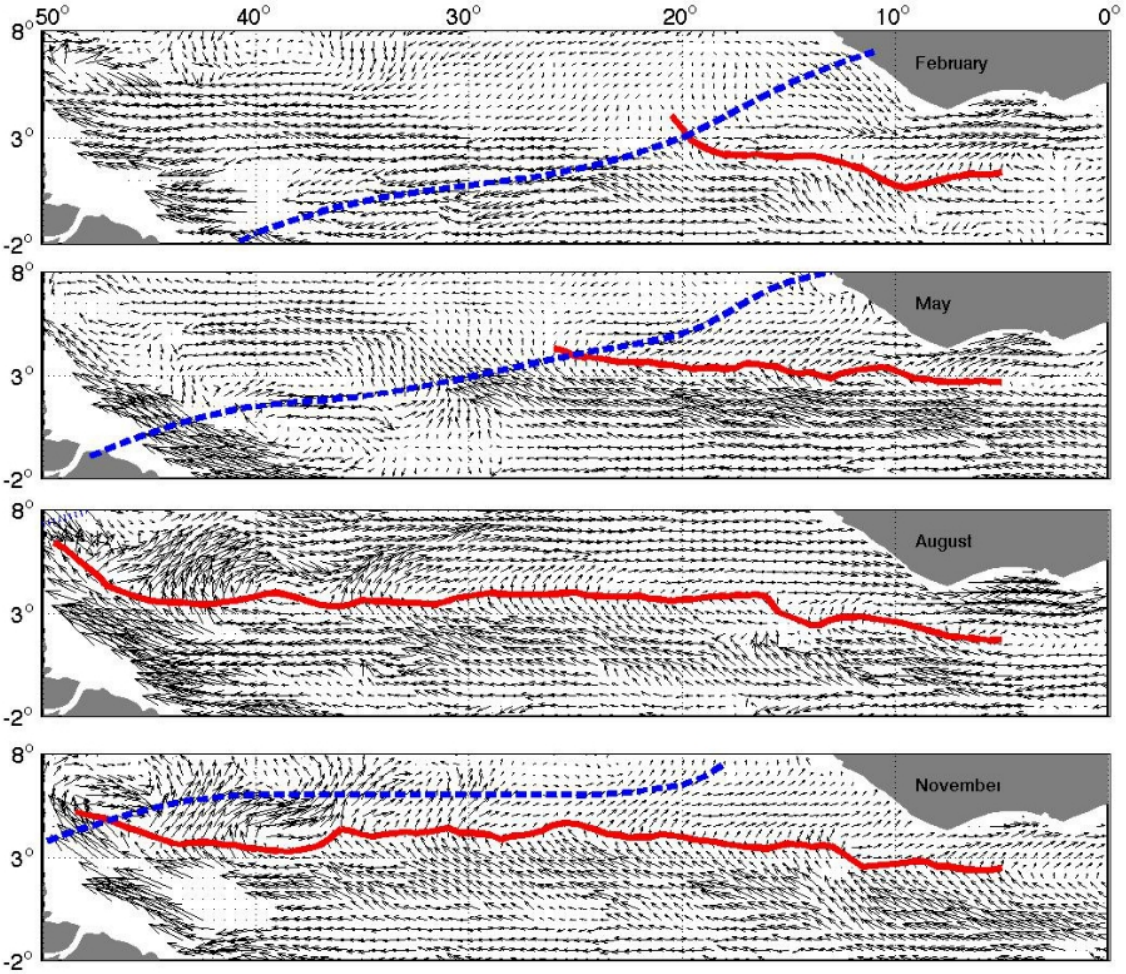

Figure 4.8: Surface velocity vectors for February, May, August and November, where the ITCZ is shown in blue and the position of the boundary between the NECC and the nSEC is shown in red.

4.5.3 Interaction NECC-nSEC and cSEC-NBC

The seasonal cycle is noteworthy, illustrating the existence of both direct and indirect responses of the surface equatorial-tropical ocean to wind forcing (Fig. 4.7). As explained above, wind forcing has a predominant annual cycle over most of the tropical and equatorial ocean although, between 2 and 10°N, there is also a semi-annual forcing; nevertheless, this semi-annual forcing dominates only in a relatively narrow zonal band, roughly between 2 and 4°N, where it does explain the concurrent semi-annual zonal currents.

Between 4 and 10°N, the predominant annual wind forcing is reflected by an annual response in zonal currents, yet the winds are always westwards but the currents revert direction (turning eastward when the winds weaken). Between 6°S and 2°N, the forcing winds have annual periodicity but the currents display a semi-annual response: A weakening of the westward currents occur at the time of minimum trade winds (centered in April) but a second reduction occurs centered in October, when the westward winds reach maximum

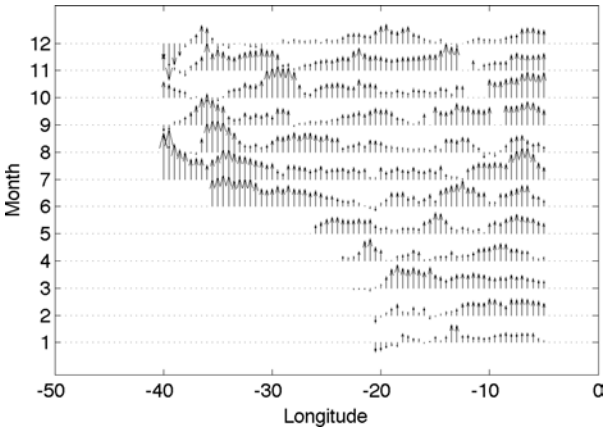

Figure 4.9: Meridional velocity component at the latitude corresponding to the boundary between the NECC and the nSeEC, drawn as a function of longitude (between 5 and 45°W) and time.

values. These apparent inconsistencies point at the existence of indirect feedback mechanisms in the equatorial and tropical surface ocean, to be discussed next.

Between July and September the westward nSEC (located in the north-equatorial band, roughly between 0 and 4°N) progressively weakens while the NECC attains its maximum expression, suggesting the existence of a possible transfer of water between the nSEC and the NECC.

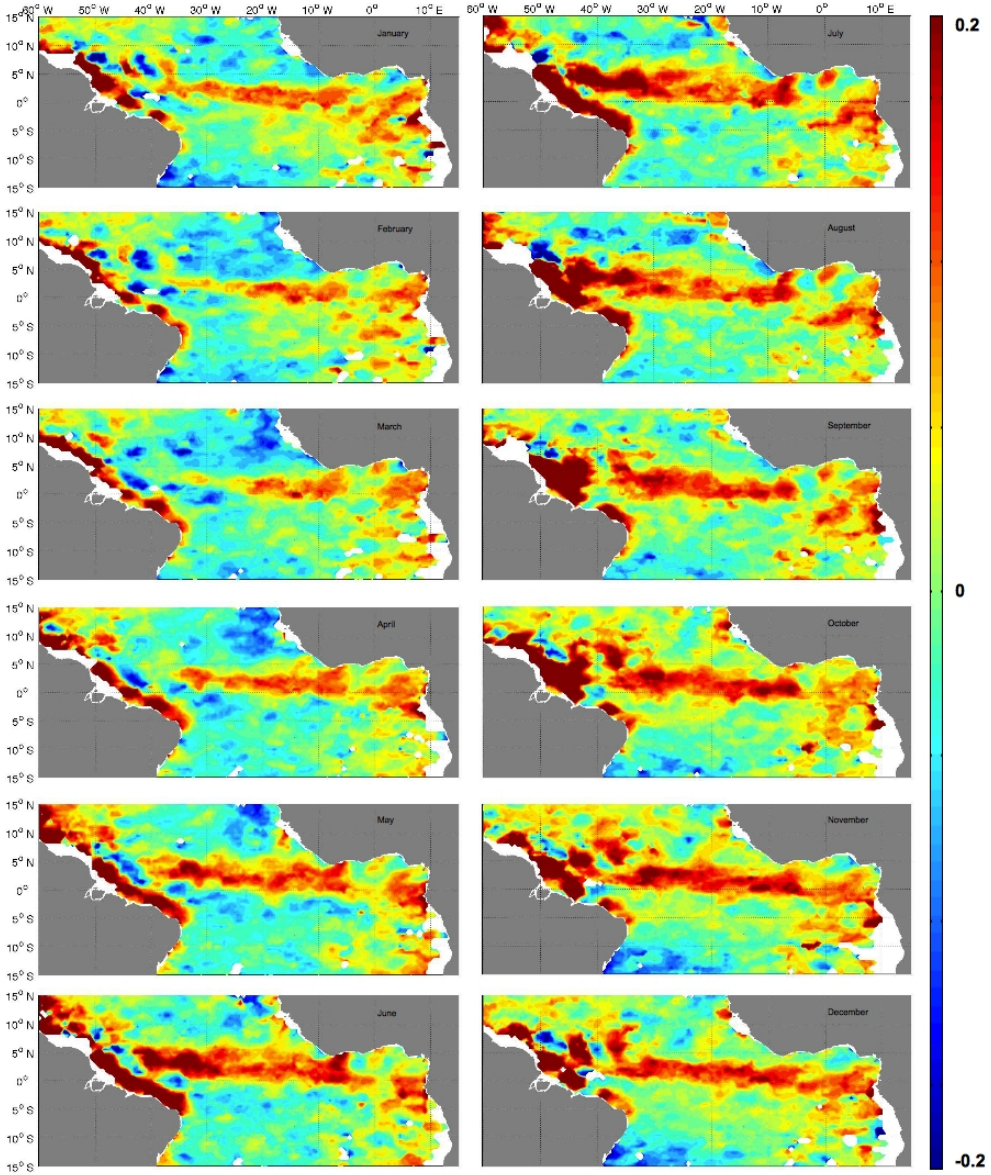

Figure 4.10: Contour maps for meridional velocities at the surface ($m\ s^{-1}$), calculated as 3-month averages.

In order to explore this connection, we define the boundary between both currents as the latitude, at any given longitude, where the zonal component changes from the nSEC negative values to the NECC positive ones. Using this definition, we can compute the location of the boundary every month, with the same 0.5° resolution of the velocity grid. Finally, we may compute the latitudinal component of the velocity vectors along this boundary.

One first remarkable result is the location of this boundary: in January and February this is located only in the eastern basin and extends progressively west, reaching the coast of South America in July (Fig. 4.8). The interpretation is now clear: the NECC feeds from the westward nSEC, in regions where the trade winds power the westward nSEC and its eastward recirculation as the NECC.

The location of the ITCZ represents a natural rupture in the westward current and, hence, sets the start of the NECC. When the boundary reaches America a connection between the interior zonal currents and the NBC is established: the NBC feeds from the westward nSEC and the retroflection of the NBC at 7-8°N now becomes the connection between the nSEC and the NECC.

The meridional velocity across the boundary between the nSEC and the NECC is drawn in Figure 4.9 as a function of latitude and time of the year. The flow at the boundary is permanently oriented north, endorsing the feeding of the NECC by the recirculating nSEC. To further support the evidence of a northward transport we show the monthly fields of the meridional velocity at surface (Fig. 4.10).

The sequence clearly shows the seasonal cycle of the meridional velocities associated to the interaction between the nSEC and the NECC. If we compare the meridional velocities (Fig. 4.10) with the zonal velocities (Fig. 4.5), we can observe how the beginning of the development of the NECC in May is anticipated by the growth of the meridional velocities in the boundary between the nSEC and the NECC. The meridional velocities achieve its maximum around June-July, and show a sustained presence until January, when the NECC is decayed and barely defined. The anticipation of the meridional velocities confirm the link between the nSEC and the NECC, and how the nSEC feeds the NECC throughout its development.

From January to April, the presence of the

northeastern trade winds in the central and western basins help inhibit the northward nSEC component and the eastward NECC. Along with the April-May northward ITZC migration, the trade winds weaken at the location of the nSEC-NECC boundary, the nSEC meridional component develops, and the NECC gets intensified. As a conclusion, the NECC is not controlled by the NBC retroflection, but rather by the westward extension of the northward nSEC bifurcation in phase with the seasonal ITCZ displacement; further, the NBC retroflection may be interpreted as the westernmost expression of this recirculating mechanism.

In the central and western basins and very near the equator (within 1°) a direct ocean response is at last found. Here the surface currents are dominated by the annual signal: The currents flow west all year long except for a short period near April, approximately coincident with the weakest winds, when the EUC surfaces (Lumpking and Garzoli, 2005). As the winds weaken, the eastward pressure force dominates the force balance and the EUC surfaces.

Finally, between the equator and 6°S, the predominant wind forcing has annual periodicity but the response has a significant semi-annual signal. Of particular significance is the weakening of the westward currents near October, coincident with the time of the strongest trade winds. The monthly sequence in Figure 4.5 illustrates the decline of this westward jet (6°S to 0°) between July and October, coinciding both with an intensification of the westward currents further west (NBC, one first pulse in August and a second one in November) and south (6 and 12°S, between September and December), illustrative of momentum transfer via either dowstream or latitudinal Ekman transports.

4.6 AAIW velocities

4.6.1 Seasonal variability

The intermediate zonal currents change drastically with season (Fig. 4.11). The AAIW zonal jets reverse direction throughout the year, with the maximum westward flow in the western margin between September and October and the maximum eastward flow in the central and eastern margin in December and January. As a consequence the annual-mean AAIW fields are clearly inadequate to represent the actual intermediate zonal currents at any time of the year.

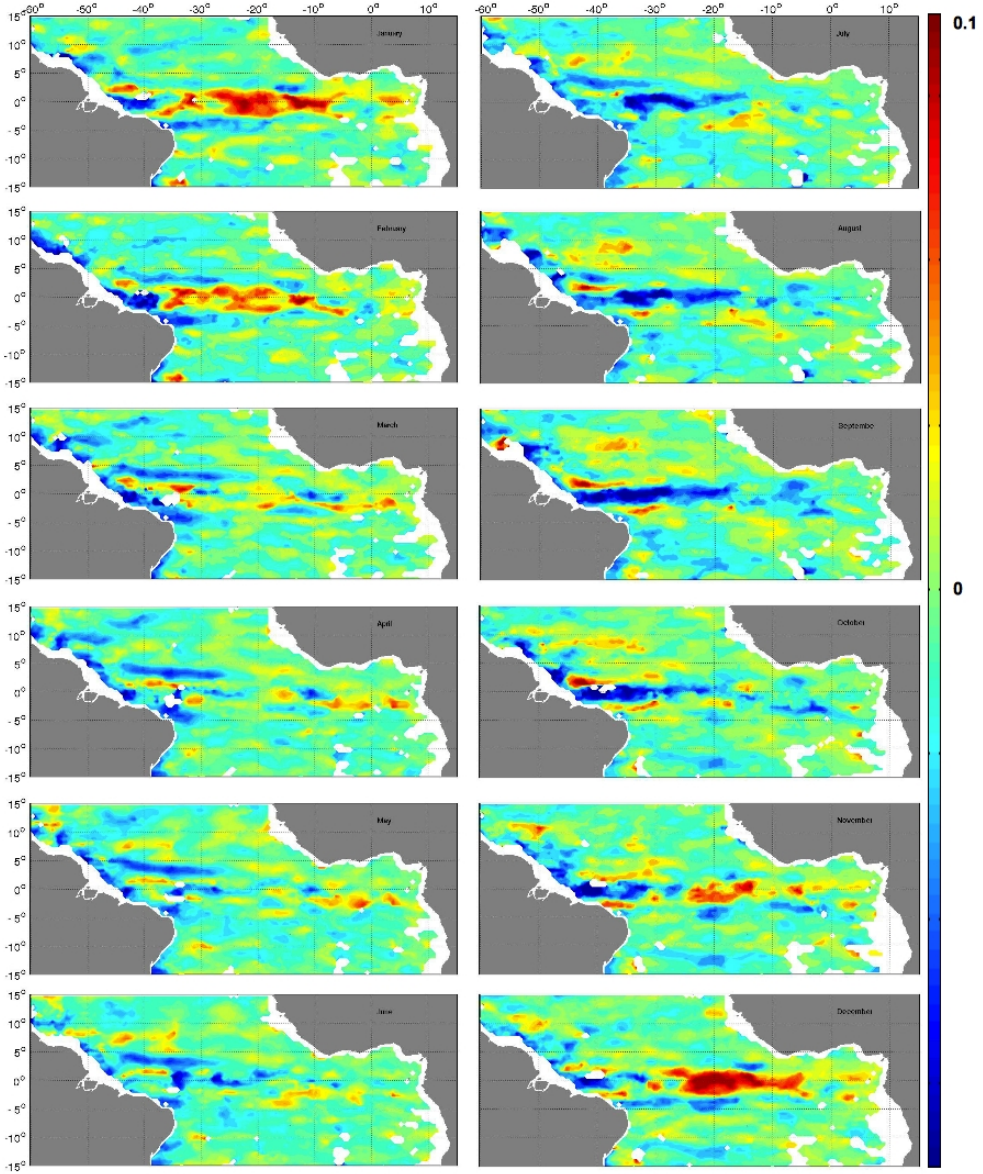

Figure 4.11: Contour maps for zonal velocities at 1000 dbar (m s^{-1}), calculated as 1-month averages.

The EIC, ubiquitously located along the equator, is substantially wider than the adjacent jets, whose location display some seasonal variability.

A remarkable feature is the alternation of direction between adjacent jets, i.e. the off-equatorial jets flow in opposition to the EIC, reversing its zonal velocity in time in the opposite way as the EIC does. The exact time of the maximum currents at any latitude, however, changes with longitude. The data shows the EIC reverses direction seasonally, flowing westward during the boreal summer and fall and eastward during the boreal winter and spring. This eastward flow, contrary to early reports on a westward flowing EIC (Ollitrault et al., 2006; Lankhorst et al., 2009), cannot arise as an error associated to an unaccounted surface drift, as the equatorial surface currents almost all year long towards the west. An important conclusion is that the five annual-mean jets found within 4° of the equator are an artifact of the time averaging (Fig. 4.5). The reality is that most often there are only three zonal jets; this is not always true as the jets do not switch direction simultaneously across the whole ocean, causing the existence of patches which difficult the identification of single, zonally-coherent, jets.

At AAIW levels, when the EIC is fully developed in the westward direction (September), the SEIC and the NEIC flow eastward on each side of the EIC. About four or five months later (January-February) the EIC reaches its maximum eastward velocity, simultaneous with the westward flow of the SEIC and followed by the NEIC (March-April). The northern and southern counter currents (NICC and SICC), previously reported by Ollitrault et al. (2006), do not show up in these representations. The seasonal pattern commonly displays three intermediate equatorial currents, with a central current on the equator and two adjacent currents flowing in opposite direction. This system of three currents shifts latitudinally throughout the year: whilst the EIC stays on the equator, the adjacent jets do not keep its latitudinal position, being closest to the equator when they flow eastward (boreal summer and fall) and reaching further away when they flow eastward (boreal winter and spring). One conclusion is that there is no clear distinction between NEIC and NICC or between SEIC and SICC, the appearance of counter flows being more a matter of a seasonal reversal in the flow direction at latitudes

Table 4.1: Major characteristics of the zonal jets in the equatorial Atlantic Ocean at the surface and intermediate water levels.

Level	Current	Core at	Flow seasonal cycle
Surface	North Equatorial Counter Current (NECC)	8°N	East with fall maximum
Surface	northern South Equatorial Current (nSEC)	2°N	West with summer-fall maximum
Surface	Equatorial Under Current (EUC)	2°	East at subsurface. Partially surfaces in spring and fall
Surface	central South Equatorial Current (cSEC)	4°S	West with spring-summer maximum
IW	North Equatorial Intermediate Current (NEIC)	3-4°N	West in spring. East in fall
IW	Equatorial Intermediate Current (EIC)	0°	West in summer. East in winter
IW	South Equatorial Intermediate Current (SEIC)	3-4°S	West in winter-spring. East in summer-fall

between 3 and 4° than a change in character with latitude. A brief summary of the predominant currents and their seasonal character is presented in Table 4.1.

The character of the seasonal varibility is clarified by the harmonic decomposition (Fig. 4.12). The amplitude of the annual signal reaches values as large as 0.07 m s^{-1} near the equator and 0.04 m s^{-1} at latitudes near 3-4°, both greater than the annual-mean values (nowhere more than 0.03 m s^{-1}; Fig. 4.4); even the semiannual amplitude at many locations along the equator exceeds the 0.03 m s^{-1} level. The phases display substantial variability, difficult to interpret, but yet some relevant features are apparent. The annual phases along the equator, between about 10°W and the coast of Brazil, increase as we move westwards, reflecting a westward propagating disturbance; something similar happens at about 3-4°N, between 15°W and the coast of Brazil, but now with a greater rate of change with distance. The semiannual phases along the equator, on the other hand, appear to have an approximately constant value.

In the lower part of Figure 4.12 we present the variance explained by both contributions. Over a large portion of the tropical ocean the annual signal explains more than 50% of the variance. The semiannual component typically explains much less variance, although often exceeds the 30% level.

4.6.2 Evidence of westward propagating waves at intermediate water levels

Figures 4.12 and 4.13 confirm the large seasonal variability at AAIW levels (Schmid et al., 2001; Ollitrault et al., 2006; Bunge et al., 2008). In particular, Figure 4.12 raises the possibility that some of the variability is related to westward propagating Rossby (plane-

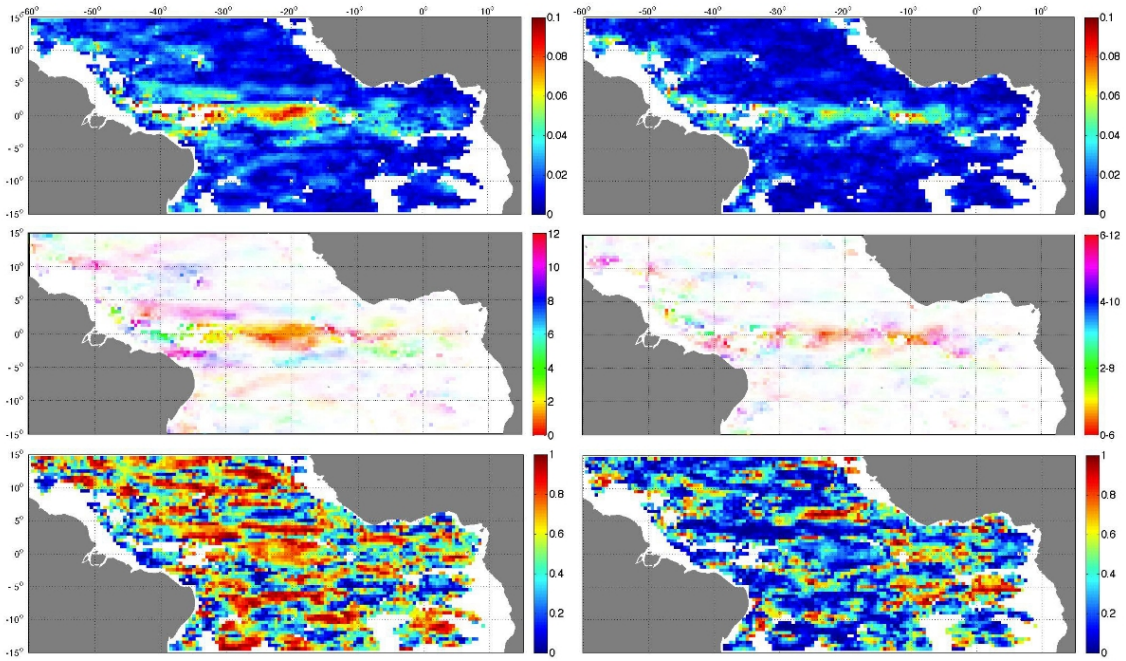

Figure 4.12: Amplitude (top) and phase (central) for the annual and semi-annual components of the zonal velocity at 1000 dbar (m s^{-1}); a transparency mask (quadratic proportion to amplitude) has been applied to the phase distributions in order to emphasize those areas with high amplitudes. The bottom panels illustrates the variance explained by either contribution.

tary) waves, as proposed by Brandt and Eden (2005) and Brandt et al. (2011). The underlying hypothesis is that the waves are generated every year at some selected latitudes in the central or eastern equatorial Atlantic Ocean, from where they propagate westwards.

We may explore this idea by looking at the zonal velocity anomaly with the help of time-distance plots; this anomaly is constructed by subtracting the annual-mean zonal velocity to the (2-month smoothed) monthly velocity values, so that a 12 point seasonal time-series is obtained per grid point.

Figure 4.13 shows the zonal velocity

anomaly plotted at the equator and four different latitudes as a function of longitude (between 45°W and 15°W) and time (in order to facilitate the visualization we plot two full years). Note we have carried out these plots every 1° between 20°S and 20°N but have chosen to plot the results at the five latitudes (7°S, 3°S, equator, 3°N and 7°N) where a propagating signal is best visible. This does not mean that a similar westward propagation does not occur at other latitudes, instead it possibly indicates there are some selected latitudes where the initial perturbation is more intense and the propagation is therefore easier to appreciate. In particular, this happens to occur at the locus of the predominant AAIW zonal currents (3°S, equator and 3°N).

The annual pattern propagates west, with maximum speeds at the equator and rapidly decreasing with latitude, as expected for planetary waves. At the equator the annual wavelike propagation is indeed clear, taking some 4 months to travel between 10 and 40°W, in gross agreement with simulations by Thierry et al. (2004). This propagating pattern also shows off clearly at 3°S, 3°N and 7°N; note that at 3 and 7°N the wave propagation appears to originate at about 15°W, or the longitude of a southward extension of the NW African coast. A linear fit to the maxima/minima annual propagating pattern gives zonal phase speeds of 0.32, 0.12 and 0.03 m s^{-1} at the equator, 3° and 7°, respectively; the values in both hemispheres are, to the second significant digit, identical.

Thierry et al. (2004) have shown that the zonal wind stress along the equatorial band results in Rossby waves propagating westward and vertically from the eastern margin, with the first meridional mode affecting the AAIW level. The wave energy rays may start at different depths and reach different longitudes at subsequent times, therefore resembling the westward propagating patterns at any given depth. Thierry et al. (2004) carried out simulations with realistic topography and winds and found that, at depths of about 1000 m, the annual amplitudes are larger than 0.04 m s^{-1} between 20 and 35°W, with maximum values of 0.06 m s^{-1}, while the maximum semiannual amplitudes exceed 0.04 m s^{-1} only between about 10 and 20°W. These results are in good agreement with our observations, both in location and magnitude (Figs. 4.12 and 4.13).

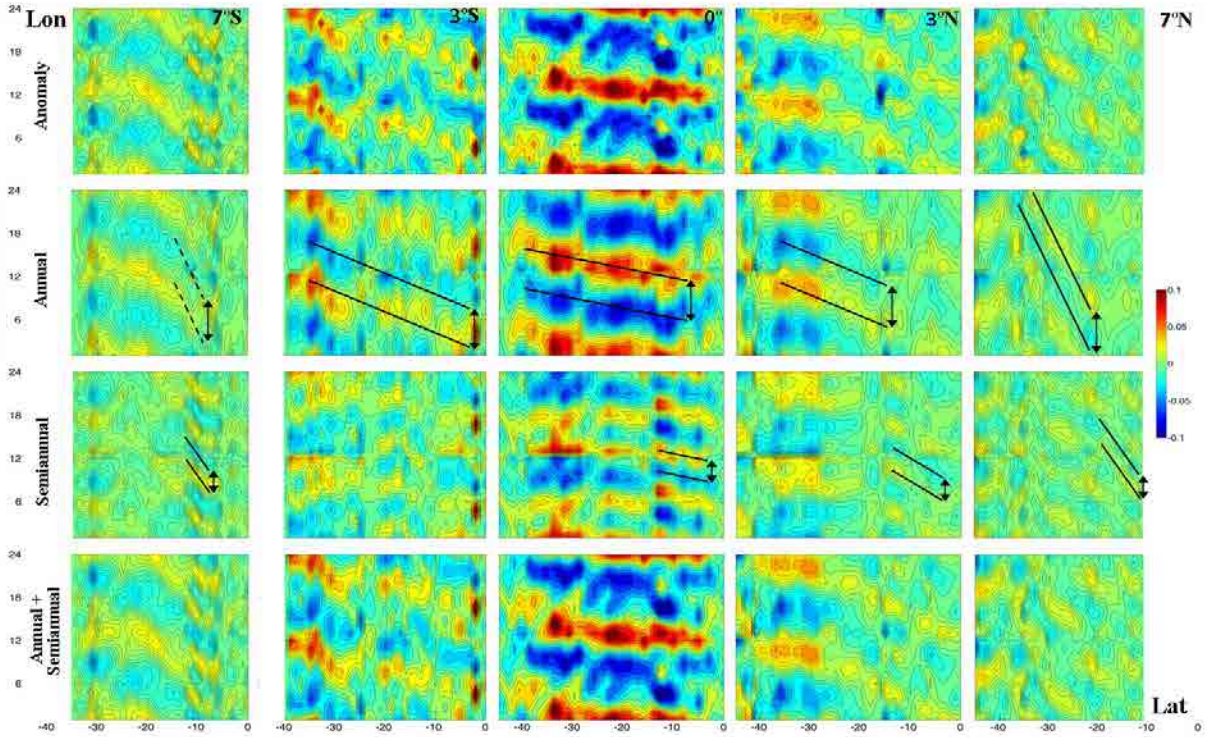

Figure 4.13: Time-longitude diagrams at different latitudes (from left to right: 7°S, 3°S, 0°, 3°N, 7°N): (first row) zonal velocity anomaly, (second row) reconstruction with the annual component, (third row) reconstruction with the semiannual component, (fourth row) reconstruction with the annual+semiannual components. The time axes display 24 months in order to provide a better view of the propagating waves; the color code gives the velocity in m s^{-1}. The lines in the second and third rows illustrate the wave progression, with maximum positive and negative velocity values respectively separated by six and three months (double-arrow lines); the dashed lines at 7°S are only suggestive of a possible path, with the same phase velocity as at 7°N.

4.7 Conclusions

Our study illustrates, for the tropical Atlantic Ocean, the potential of Argo data to investigate the velocity fields at the surface and the float parking depths. In this application we have examined three parking depths: central waters (200 m), deep intermediate waters (1000 m) and upper deep waters (1500 m). The Argo data set is large enough to produce annual-mean fields at all depths in the equatorial Atlantic Ocean. Further, the amount of data is sufficient to construct a canonical year at surface and deep intermediate waters (AAIW), susceptible to examine the seasonal changes. No attempt has been made to investigate the interannual variability as most of the available data for the region corresponds to the last few years.

The excellent spatial coverage confirms the predominance of the zonal jets in the equatorial Atlantic at all levels, as previously reported by several authors. At surface the jets intensify seasonally but do not change direction, except for the summer appearance of the North Equatorial Counter Current. At the intermediate level, on the contrary, the jets display significant inversions at different latitudinal bands, some 3°S, 0° and 3°N for de AAIW. The instantaneous intermediate jets are relatively wide (about 4°) and take place at 3-4°N (North Equatorial Intermediate Current), at the equator (Equatorial Intermediate Current), and 3-4°S (South Equatorial Intermediate Current), and no other prominent counter-currents have been identified. The annual-average of these seasonal intermediate jets leads to the appearance of numerous narrow jets, so that this mean field is a poor description of the system at any time. A similar artefact may indeed be happening at the central and deep levels but we have no way to validate this assertion from the limited amount of velocity data at these levels.

The reasonably good spatial resolution grants additional perspectives for the seasonal evolution of the flow both at the surface and AAIW levels. At the surface, for example, we find that the April intensification of the NECC starts in the eastern Atlantic through a northern diversion of the nSEC and progressively extending westwards, and we detect the presence of a double NECC core only near the western margin. A novel view of the retroflection of the NBC, as the westernmost limit of this recirculation between nSEC and NECC, arises. At the

AAIW we find there are only three equatorial jets, a central one at the equator and two adjacent opposite currents which change their latitudinal location and direction during the year.

The annual+semiannual harmonic analysis of the zonal velocity at the intermediate level confirms the predominance of annual and, to a lesser degree, semianual anomalies. The annual component typically explains up to 50% of the variance and the semiannual component up to another 30%. These analyses, together with the time-longitude representation of the zonal velocity anomalies at different latitudes, confirm that the seasonal variability is predominantly caused by the westward propagation of planetary waves at those latitudes which define the location of the AAIW zonal jets (3°S, 0°, 3°N). The size of these seasonal anomalies reaches values of about 0.1 m s-1, several times larger than the annually-averaged currents.

These results indeed give further support to the assertion that the seasonal variability at the AAIW level is caused, to a great degree, by the flow inversion associated to the passage of westward propagating long Rossby waves. The propagation is slow enough to be detected by our temporally-smoothed velocity data and, to a first degree, it may be simulated with a contribution of annual periodicity. This contrasts with the situation observed at the surface level, where the Rossby wave propagates too fast to be captured by our monthly velocity fields. Therefore, at the surface the observed seasonal variability does not reflect any transient wave but rather a succession of states that respond to an annual-changing atmospheric forcing.

Chapter 5

Tasman Leakage

In this chapter we use Argo float trajectories to infer the ocean current velocities and transports near Australia. The number of Argo float data is sufficient to determine the anual and seasonal velocity fields at both the sea surface and 1000 dbar. This allows us to carefully investigate one possible path for the returning limb of the Conveyor Belt, the one that transports Pacific Ocean waters around the southern part of Australia, into the Indian Ocean and, eventually, past Good Hope Cape and into the South Atlantic Ocean.

The East Australian Current (EAC) flows southwards along the east coast of Australia at both surface and intermediate levels but only the intermediate waters leak round the southern tip of Tasmania and cross the Great Australian Bight. From the Argo-inferred velocity fields, we will calculate the transport of Antarctic Intermediate Water (AAIW) between the southern Australian coast and the Antarctic Circumpolar Current (ACC) as the velocity at 1000 dbar times the layer thickness.

After introducing the state of the art in the first section we describe the methods in section 5.2. The third section focuses on the estimation of the error in our water transport estimation method. Section 5.4 is the actual section where the results are presented. We first consider the annual mean to later describe the seasonal cycle of the EAC and the TL, to finally give an estimation of the Tasman Leakage water transport at intermediate depth. We conclude the chapter in section 5, where the main achievements in the chapter are summarized.

Rosell-Fieschi, M., Rintoul, S.R., Gourrion, J., Pelegrí, J.L., 2013. Tasman Leakage of intermediate waters as inferred from Argo floats. Geophysical Research Letters 40, 5456–5460.

5.1 The Tasman Leakage and the Southern Ocean supergyre

The global overturning, or thermohaline, circulation, largely determines the capacity of the ocean to store and transport heat and carbon and thereby influence climate. Sinking of dense water in the North Atlantic and Southern Ocean is balanced by a return flow of lighter water in the upper ocean. The existence of such a global-scale overturning circulation depends on the exchange of water masses between basins, both in the deep and upper levels of the ocean. For the upper limb, most attention has been placed on two primary pathways: the cold route through Drake Passage (Rintoul, 1991) and the warm route following the Indonesian Throughflow and the Agulhas Current (Gordon, 1986).

A third route, the Tasman Leakage (TL), has been identified more recently (Speich and Blanke, 2001; Speich et al., 2002, 2007). Repetitions of section SR3, a World Ocean Circulation Experiment (WOCE) hydrographic section between Tasmania and Antarctica, have confirmed a westward subsurface flow south of Tasmania (Rintoul and Bullister, 1999; Rintoul and Sokolov, 2001) but say nothing about its pathway to the Indian Ocean. Model studies and observations suggest the TL provides a Pacific-to-Indian supply, a key link in a "supergyre" connecting the subtropical gyres of all southern hemisphere basins (Rintoul and Sokolov, 2001; Sloyan and Rintoul, 2001; Speich et al., 2002; Ridgway, 2007; Ridgway and Dunn, 2007).

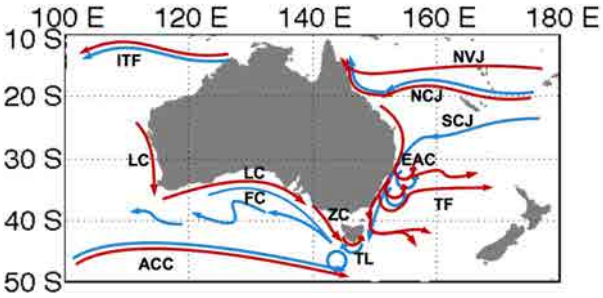

Figure 5.1: Schematic representation of the main surface (red lines) and subsurface (blue lines) currents near Australia. Acronyms are as follows: ACC for Antarctic Circumpolar Current; EAC for Eastern Australian Current; FC for Flinders Current; LC for Leuwin Current; NCJ for North Caledonia Jet; NVJ for North Vanuata Jet; SCJ for South Carolina Jet; TF for the jet associated to the Tasman Front; TL for Tasmania Leakage; ZC for Zeehan Current.

The westward flowing South Equatorial Current (SEC) reaches the western boundary of the Pacific Ocean and bifurcates between 15° and 20°S into northern (North Vanuatu and North Caledonia) and southern (South Caledonia) jets (Fig. 5.1). The North Caledonia (near surface)

and South Caledonia (at intermediate levels) jets turn south at the Australian coast to form the East Australian Current (EAC), the western boundary current of the South Pacific subtropical gyre (Godfrey et al., 1980; Ganachaud et al., 2008). In the near-surface layers, the EAC separates from the coast on its southward trip, either recirculating to form a double cell structure (Ridgway and Dunn, 2003) or turning offshore at the Tasman Front or near Tasmania. Surface waters of the EAC extend further south in summer but do not breach the southern tip of Tasmania (Ridgway and Godfrey, 1997). At intermediate depths, on the other hand, part of the EAC continues south along the coast and turns west, between Tasmania and the South Tasman Rise, as the TL (Fig. 5.1). The extension of the TL into the Great Australian Bight (GAB) is known as the Flinders Current (FC) (Middleton and Cirano, 2002); this subsurface current increases as it progresses west because a fraction of the water transported by the Antarctic Circumpolar Current (ACC) recirculates westward through a large anticyclonic loop located between about 139° and 146°E (Rintoul and Sokolov, 2001). Along the southern coast of Australia, an extension of the Leeuwin Current forms a weak eastward flow of surface waters extending from Western Australia to Tasmania (Ridgway and Condie, 2004).

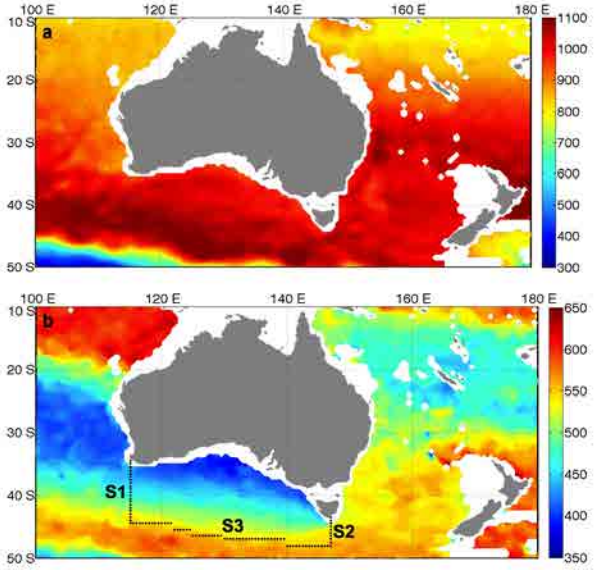

Figure 5.2: (a) Central level and (b) thickness of the AAIW layer (m), defined as having neutral densities between 27.125 and 27.6 kg m-3. The bottom panel also shows the sections used to estimate the error in the transport associated to the TL.

Previous studies of the EAC and the TL have relied on hydrographic data or model output. In this work we use Argo float data to infer the velocity at the sea surface and 1000 dbar (the parking pressure of most Argo floats) and to es-

timate the thickness of the Antarctic Intermediate Water (AAIW) layer. We then combine the velocity and thickness information to quantify the variability in water transport south of Tasmania and the mean transport reaching the Indian Ocean.

5.2 Data and methods

The method used to calculate the velocities is the same as we applied for the equatorial Atlantic Ocean, but with some slight differences, and a complementary methodology aimed to estimate the water transport.

Whilst the equatorial Ocean presents a much larger zonal correlation that the meridional one, justifying a gridding process according to this correlation, the situation for the currents involving the Tasman Leakage is different: despite being true that the actual Leakage is predominately zonal, the East Australian Current (EAC), which is at the origin of the Tasman Leakage, is strongly meridional. For this reason, we chose not to give any preference to the zonal, nor the meridional correlation.

Here we use all delayed-mode Argo data up to March 2013, with a quality control label of "good", downloaded from the Coriolis Operational Oceanography centre (www.coriolis.eu.org). We use Chauvenet's criterion (Taylor, 1997) to identify, and reject, spurious velocity vectors as those with either zonal or latitudinal components exceeding five standard deviations. This gives a total of 69115 velocity vectors for the surface and 58757 velocity vectors at 1000 dbar. The annual-mean velocity is interpolated on a $1/2^\circ \times 1/2^\circ$ grid, calculated from all data contained in a 100-km radius; similarly, the seasonal values are interpolated on a $1^\circ \times 1^\circ$ grid, using a 150-km search radius. This generates considerable overlap between adjacent cells but increases significantly the number of velocity vectors available in each cell.

The AAIW layer is defined to lie between neutral densities of 27.125 and 27.6 kg m^{-3} (Speich et al., 2002). The depths of the neutral surfaces, calculated from the salinity and temperature profiles of those same Argo cycles used to compute the velocity fields, are projected on a grid following the same procedure as for the annual-mean velocities. The results show that the central-depth point of the AAIW layer is reasonably constant and close to 1000 dbar for

the whole study area (Fig. 5.2a), confirming that floats parked near this depth level indeed track this water mass.

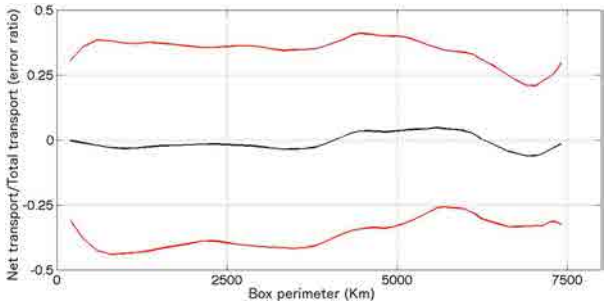

Figure 5.3: Mean value (black line) and standard deviation (red lines) of the ratio between net and total transports (relative error, RE) for sets of boxes of different size as a function of the perimeter of each individual box (in km). The smallest boxes, of side 0.5° in latitude and longitude, have a perimeter of about 200 km; the largest ones, with side 19° , have a perimeter close to 7500 km.

The Eulerian transport is estimated by multiplying the thickness of the AAIW layer (Fig. 5.2b) by the velocity at 1000 dbar. The numerical results of Cirano and Middleton (2004) endorse the assumption of a nearly constant velocity throughout the AAIW layer. We use the divergence of the inferred velocity field to estimate a potential error of 35% in our transport estimates. We also show that this error bar is large enough to take into account possible uncertainties associated with the vertical shear of horizontal velocity within the AAIW layer and the limited sampling of relatively narrow boundary currents.

5.3 Error estimation for the AAIW transport

Previous studies have imposed horizontal non-divergence as an additional constraint when mapping velocity fields derived from float trajectories (Davis, 2005). Here we use the divergence of the calculated velocity field to derive an error bar on the transport estimates. We divide the region into as many approximately squared boxes as possible, with side lengths varying from 0.5° to a maximum of 19° in latitude and longitude, at increasing intervals of 0.5°, adjusting their shape where necessary to account for continental boundaries; for this calculation we only use the region between 45° S - 20° S and 100° E - 180° E, in order to avoid the southern and northern areas where the mean AAIW depth departs considerably from 1000 dbar (Fig. 5.2a). We then compute the net and total AAIW transports into each box, with the total transport calculated as the sum of the absolute values of all

individual transports (per grid cell) into or out of the particular box, and calculate a relative rrror (RE) defined as the net transport divided by the total transport. Finally, we combine sets of boxes of equal perimeter and compute the RE mean and standard deviation as a function of box perimeter. The mean remains quite low, with maximum values always less than 0.1, and the standard deviation decreases with increasing size, from about 0.4 to 0.25 (Fig. 5.3).

Given RE as a function of box perimeter, in order to assess the transport uncertainty across any particular section we add additional sections until we form a closed box. If we wish to know the uncertainties through sections S1 (along 115° E) or S2 (along 147° E), we add S3 to produce a closed box whose northern boundary is the Australian continent (Fig. 5.2b) and calculate the RE for this particular box. Notice that S3 is chosen north of the ACC, so that the transport error is not related to the shallowing of AAIW. The RE calculated this way is small, 0.069, and confirms that the selected region is, to first order, non-divergent. The perimeter of the S1+S2+S3 box is 5163 km and its corresponding standard deviation is 0.35 (Fig. 5.3). The transport errors through either S1 or S2 are

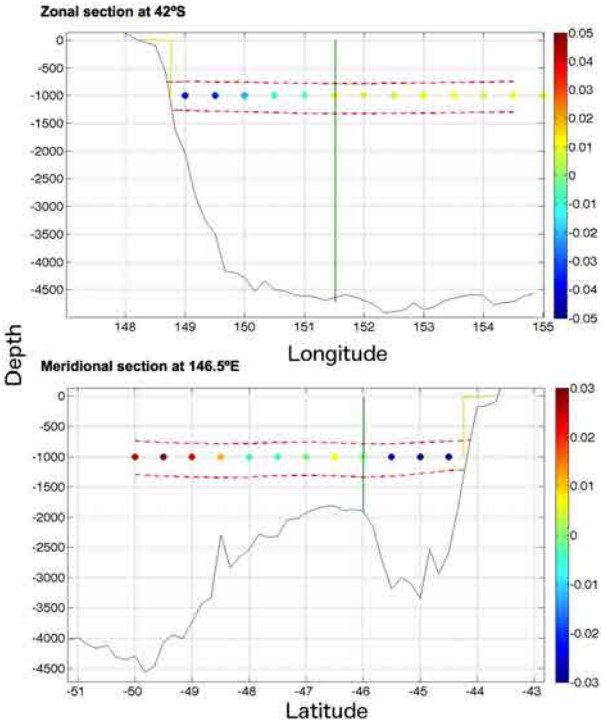

Figure 5.4: . (Top panel) Zonal section along 42° S, normal to the East coast of Australia, and (bottom panel) meridional section along 146.5° E, south of Tasmania. The 27.125 and 27.6 kg m^{-3} neutral surfaces (dashed red lines) are approximately equidistant above and below the parking depth. The dots show the velocities at 1000 m every half a degree (color-coded; negative values represent southward currents through 42° S and westward currents through 146.5° E). A green vertical line illustrates the limit of the southward EAC flow in the 42° S zonal section and the westward TL flow in the 146.5° E section.

therefore estimated to be 35% of the calculated transports.

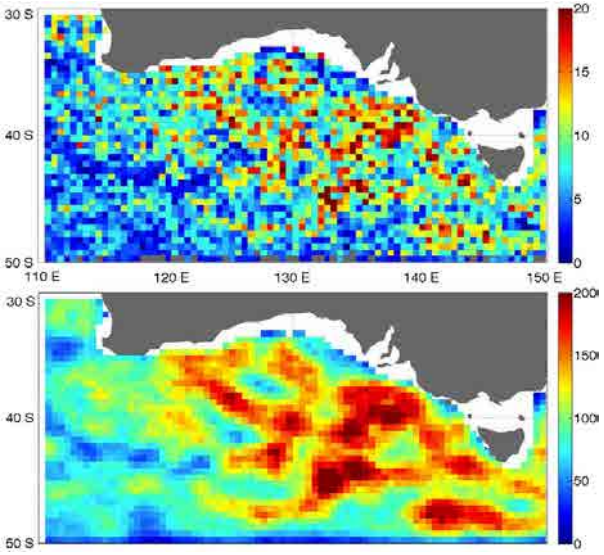

Figure 5.5: Number of AAIW velocity vectors in each 0.5° × 0.5° cell: (top panel) actual number of velocity vectors within each cell element, (bottom panel) after using a 100-km search radius. The white regions around the continents correspond to water depths less than 1000 m.

We want to make sure that this error bar satisfies two possible error sources, as discussed next. The first source of error is related to the possibility of a narrow boundary current which is under-sampled. We separate this error in two contributions. The first one is related to the sloping boundary, which may cause that portions of the AAIW with bottom depths less than 1000 m do not get sampled (Fig. 5.4). In general, however, this error will be largely compensated by transport overestimates in those portions of the AAIW with sea-bottom neutral density less than 27.6 kg m^{-3}. At most, for typical bottom slopes, this error will account for about 3% of the total transport.

The second contribution is related to the possibility that the transports get under or overestimated because of a relatively small or large fraction of floats located in the core of the boundary current. Such a situation could occur if we had a small number of floats that behaved as Lagrangian tracers. However, for the Argo floats, the alternation of deep and surface drifts causes that each single displacement is effectively independent from the previous one. With typical velocities of 0.5 m s^{-1} (0.05 m s^{-1}) for surface (intermediate) waters and time scales of half a day (10 days) it turns out that there is a lag distance of about 22 (43 km) between subsequent displacements. This is of the same size as the characteristic radius of high-latitude eddies (Herraiz-Borreguero and Rintoul, 2011) and confirms that successive individual trajectories

will often be unrelated: each velocity vector may be considered as a randomly-located Eulerian measurement. Therefore, provided that the number of velocity vectors is sufficiently large, the gridding and averaging process shall give robust (Eulerian) mean and standard deviation values at each grid point. Figure 5.5 indeed suggests a random distribution in the number of AAIW velocity vectors inside $0.5^\circ \times 0.5^\circ$ cells, both before and after using a search radius of 100 km. The number of vectors using a 100-km search radius is quite large, often more than 100 values per grid cell off the east coast and in the GAB; the actual number of velocity vectors within each cell element is substantially less but yet large enough to guarantee that we properly resolve the near-slope boundary currents.

The second error refers to the existence of vertical velocity shear within the AAIW layer. Several studies show that, except for the presence of mesoscalar changes, the slope of AAIW isopycnals is relatively constant south of Tasmania (Morrow et al., 2004; Herraiz-Borreguero and Rintoul, 2011). If the 1000 m horizon was at the center of the AAIW layer, we would expect that the excess transport on the top half of the AAIW would closely compensate the defect transport on the bottom half. However, the bottom half of the AAIW layer is in average about 50 m thicker than the top half. Considering the mean latitudinal density gradient within the AAIW layer (about 0.1 kg m^{-3} in 250 km) and assuming geostrophy, we estimate a vertical velocity gradient of 0.4×10^{-4} s^{-1}. Over a 50-m thick layer this represents a maximum speed change of 0.2 mm s^{-1}, a factor about 15 times smaller than the mean speeds of the TL at 1000 m. Clearly both error sources are well within the estimated 35% error bar.

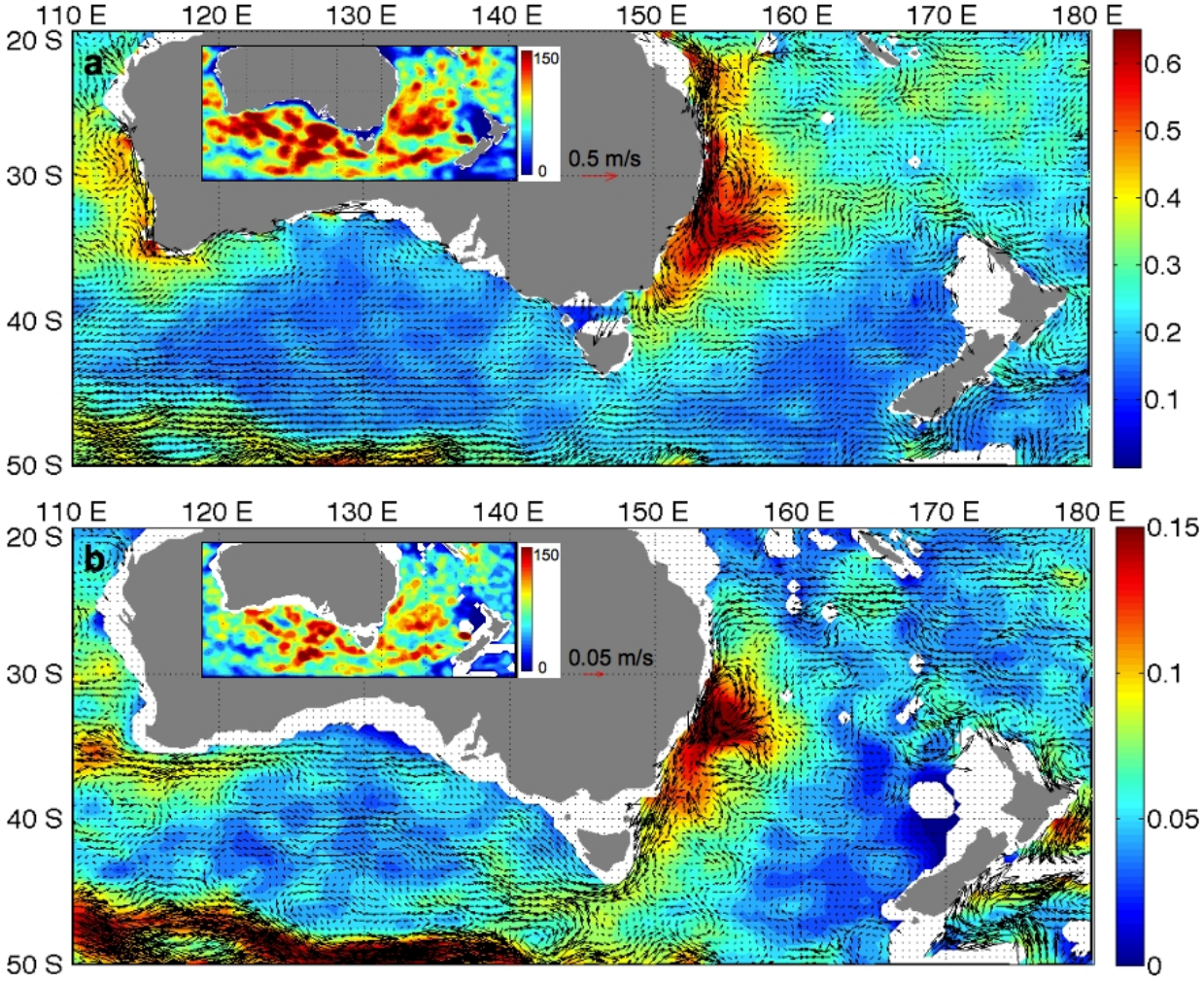

Figure 5.6: Mean current speed (colour-coded, m s^{-1}) and current velocity vectors near Australia, both at (a) the sea surface and (b) 1000 dbar. The inset illustrates the available number of data point for each 0.5° × 0.5° cell element.

5.4 Results

5.4.1 Annual mean

The annual-mean sea-surface velocity map (Fig. 5.6a) shows a double anticyclone associated with recirculations of the EAC, with a weak separation from the coast at about 32° S and a much stronger one at about 34° S, associated to the Tasman Front (Ridgway and Dunn, 2003). The ultimate offshore diversion of the surface flow, however, takes place at about 40° S, so that no flow goes round the southern tip of Tasmania. The annual-mean AAIW velocity map (Fig. 5.6b) also exhibits some partial retroflection at about 34° S but a major portion continues south and then turns west, between the Tasmania coast and the South Tasman Rise, as the TL (Rintoul and Sokolov, 2001; Ridgway and Dunn, 2007).

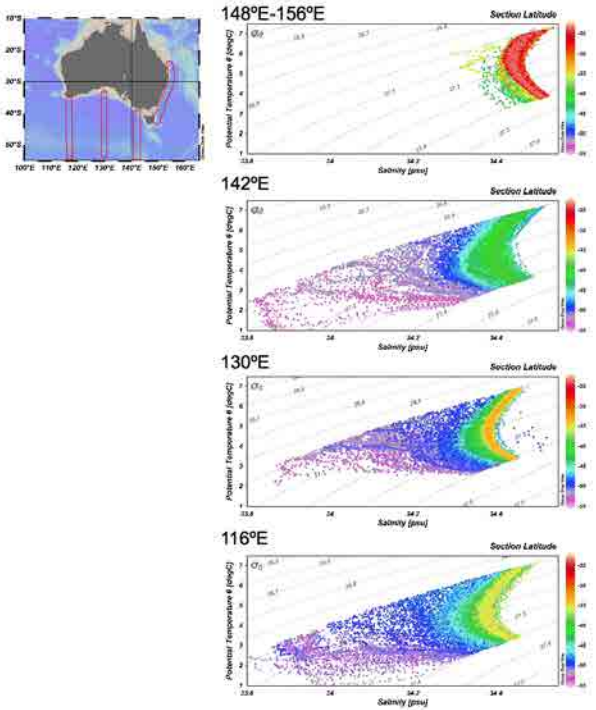

Figure 5.7: Potential temperature-salinity ($\theta - S$) diagrams for AAIW in 200-km wide selected bands. These bands, as shown in the right-top panel, are centered (a) along the east coast of Australia, and normal to the southern Australian coast approximately along (b) 142° E, (c) 130° E, and (d) 116.5° E. The data points in the $\theta - S$ diagrams are color-coded according to their latitude and the potential density isolines are shown as dotted gray lines.

5.4.2 Seasonal variation in the EAC and the TL

The surface EAC has seasonal variations greater than most mid-latitude western boundary currents (Ridgway and Godfrey, 1997),

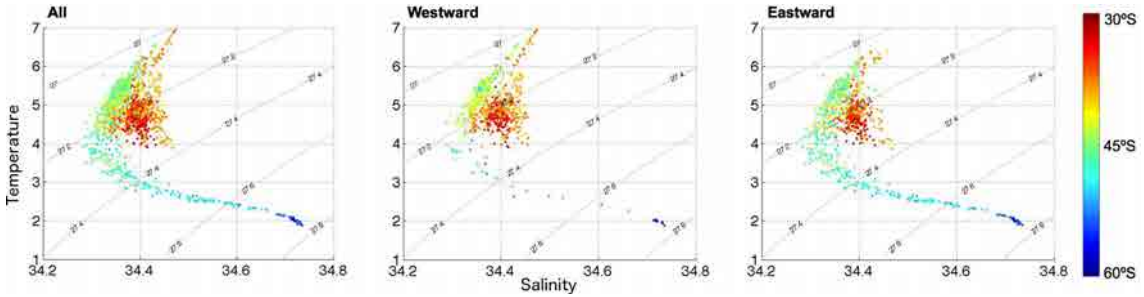

Figure 5.8: Potential temperature-salinity ($\theta - S$) diagrams for data points within 50 dbar of the 1000 dbar parking depth, in the region between the Australian coast and 60° S and between 115° E and 148° E. The left panel shows all data, the center panel presents only data for westward floats and the right panel shows only data for eastward floats. The data points are color-coded according to their latitude and the potential density isolines are shown as solid gray lines.

strengthening and extending further south during the austral summer and weakening in winter (Fig. 5.9). The greatest variability is associated with the northward offshore counter-current, to the extent that the annual-mean flow may be largely accomplished by eddies (Ridgway and Godfrey, 1997; Ridgway and Dunn, 2003). One cause for such variability may be the seasonal cycle of the impinging SEC, which feeds the EAC (Sokolov and Rintoul, 2000). Another reason may be the variable extension of the Leeuwin Current across the GAB (Ridgway and Godfrey, 1997): During the austral winter and spring this current rounds the southern tip of Tasmania and flows along its eastern coast as the northward extension of the Zeehan Current (ZC), possibly blocking the southward progression of the EAC.

In contrast to the strong seasonality of the surface flow, the EAC and its westward TL extension are remarkably steady at the AAIW level during all seasons (Fig. 5.9). Nevertheless, the subsurface EAC also experiences seasonal changes, as its northern portion strengthens during austral spring and autumn and the southern portion gains intensity during austral winter and summer.

South of Australia, the surface waters have a weak eastward flow while the AAIW stratum predominantly moves west. The AAIW contains two different water types: a cooler and fresher variety coming from the ACC and a warmer and saltier variety supplied by the EAC.

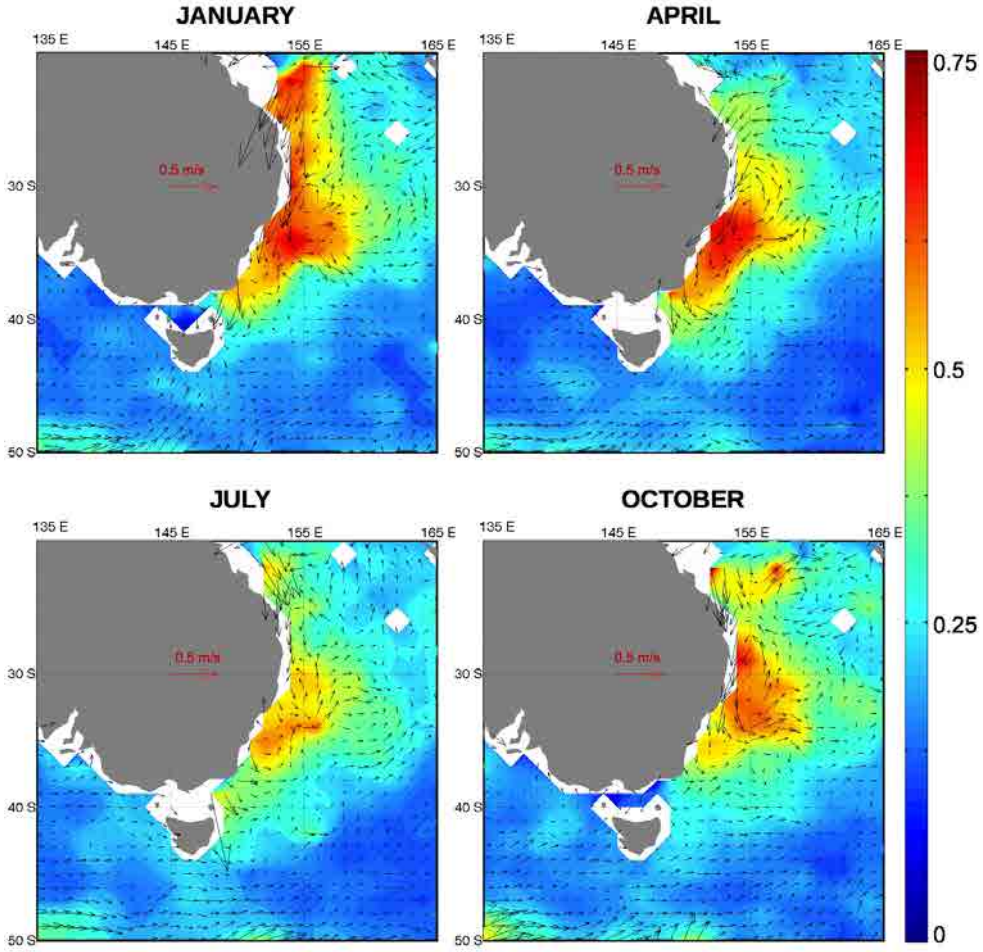

Figure 5.9: Surface seasonal variation of the current speed (colour coded, in m s^{-1}) and current velocity vectors for the region with the EAC and the Tasman Leakage. Each season is calculated as a three month average centred on the specified month. The top panels correspond to the sea-surface fields and the bottom panels display the 1000 dbar fields.

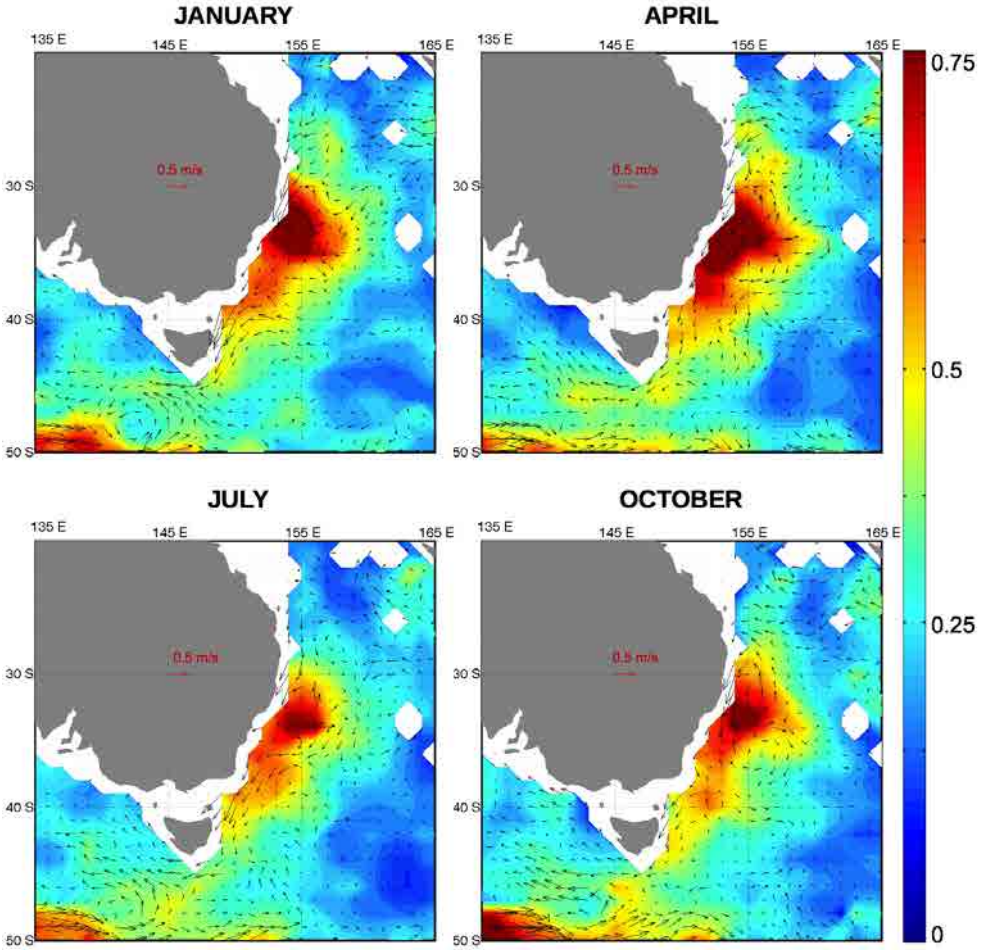

Figure 5.10: 1000 dbar seasonal variation of the current speed (colour coded, in m s^{-1}) and current velocity vectors for the region with the EAC and the Tasman Leakage. Each season is calculated as a three month average centered on the specified month. The top panels correspond to the sea-surface fields and the bottom panels display the 1000 dbar fields.

An analysis of temperature-salinity diagrams from the east and south coasts of Australia confirms the continuity of the EAC variety all the way from east to west Australia (Fig. 5.7).

It also confirms that part of the AAIW carried east by the ACC recirculates to the west at lower latitudes, as observed south of Tasmania by Rintoul and Sokolov (2001), thereby enhancing the westward AAIW flow in the northern GAB (Fig. 5.8).This may be related to the alternation in the intensity of those jets (North Vanuatu, North Caledonian and South Caledonian) feeding the EAC (Ganachaud et al., 2008).

5.4.3 Intermediate water-mass transport by the TL

There have been several attempts at estimating the magnitude of the TL. The first geostrophic calculations, from repeated transects of the SR3 WOCE section, gave a transport of 8 ± 13 Sv for the whole water column (Sokolov and Rintoul, 2001). Early results by Speich et al. (2002) quantified the TL as the result of 13 ± 3 Sv of Subantarctic Mode Water (SAMW) and 26 ± 4 Sv of AAIW; however, only a fraction of this transport, 3.7 ± 2.5 Sv of SAMW and 10 ± 3 Sv of AAIW, reached the Indian Ocean. Later model computations by Speich et al. (2007) found a Lagrangian mean transport of 3.2 Sv of intermediate waters all the way to the North Atlantic. Davis (2005), from a limited number of float trajectories near 1000 dbar and assuming an AAIW thickness of 500 m, estimated a leakage of 7.5 Sv from the Pacific to the Indian Ocean.

Here we estimate both the TL and ACC contributions to the intermediate water transport into the Indian Ocean. We limit our calculations to the region north of the ACC, as the AAIW layer shoals rapidly to the south (Fig. 5.2a). The accumulated annual-mean zonal transport is calculated every 0.5° between sections S1 (147° E) and S2 (115° E), i.e. along the whole GAB, integrating south from the Australian coast (Fig. 5.10a). These accumulated transports, equivalent to streamlines for the AAIW layer, reveal the path of the TL from the Pacific to the Indian Oceans and the appearance of contributions due to the recirculation of ACC. We find an Eulerian mean transport of 3.8 ± 1.3 Sv across 147° E.

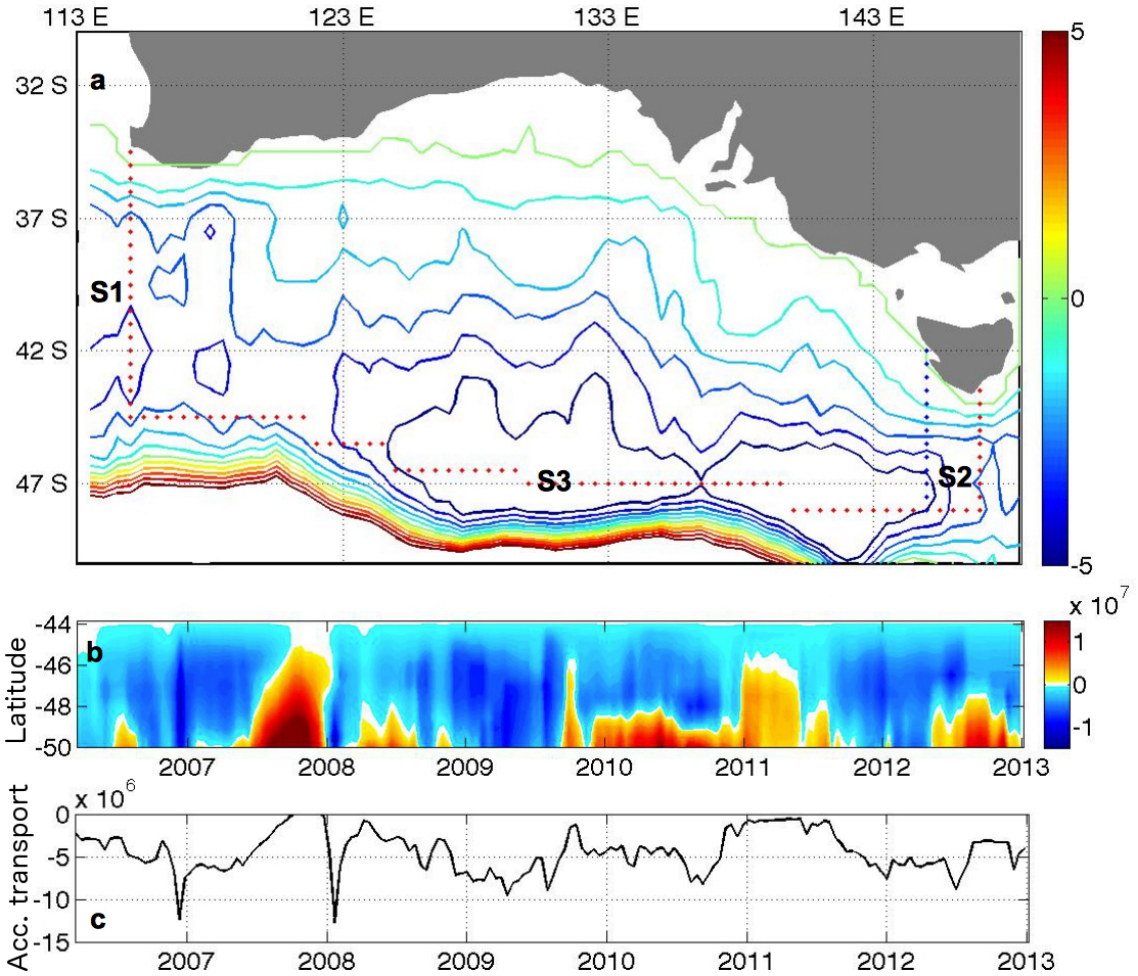

Figure 5.11: (a) Annual-mean AAIW streamlines south of Australia, zero is taken at the coast and increasing negative values represent westward transport (Sv). Sections S1 (117° E) and S3 (147° E) are shown as red dotted lines, the blue dotted lines coincide with 145° E, where Speich et al. (2007) did their transport calculations. (b) AAIW transport across 147° E (Sv), integrated south from Tasmania, as a function of time and latitude; values are obtained using a five-month running filter with a search radius of 150 km and gridding on 1° cells. (c) Time series of the maximum westward transports (negative values, Sv) in panel (b). Tick marks in (b) and (c) indicate the beginning of the calendar year.

A significant ACC input (1.2 Sv) occurs between 145 and 147° E, provided by the eastern limb of a large anticyclonic gyre which extends from about 123 to 146° E. The transport entering the Indian Ocean is estimated as 5.2 ± 1.8 Sv, being the result of three contributions: the TL through 147° E (3.8 Sv), water escaping westward from the anticyclone between 123 and 146°E (0.4 Sv), and water recirculating in the southwestern end of our domain (1.0 Sv).

The number of Argo floats south of Tasmania allows estimating changes in water transport through section 147° E, at temporal scales influenced by eddies. We calculate the accumulated transports south of Tasmania, every 15 days, between March 2006 and December 2013; for this calculation we use a running-interval of 150 days (five months) as a characteristic time scale for eddies in this region (Herraiz-Borreguero and Rintoul, 2011) (Fig. 5.10b). The negative values are a measure of the Eulerian TL transport at each time, which varies between 0 and -12.0 Sv, with a mean value of -4.4 Sv and a standard deviation of 2.8 Sv (Fig. 5.10c); this variability reflects the high eddy activity along 147° E, as suggested by van Sebille et al. (2012) from numerical models. Given the thickness h, width d, and speed u of the westward AAIW flowing waters, so that the cross-sectional transport area is $A = hd$, we may decompose the mean transport $\overline{Au} = -4.4$ Sv as contributions from the mean values and their fluctuations $\overline{Au} = \overline{A}\,\overline{u} + \overline{A'u'}$. Computing $\overline{A}\,\overline{u} = 2.7$ Sv, we estimate the eddy contribution to be $\overline{A'u'} = 1.7$ Sv, or 39% of the total transport.

5.5 Conclusions

Velocity data inferred from Argo float trajectories is used to characterize the currents near Australia at the sea surface and 1000 dbar levels. The inferred flow field agrees with the geostrophic circulation as estimated from a hydrographic climatology and a level of no motion (Ridgway and Dunn, 2003). The circulation off eastern Australia is dominated at both levels by the EAC. However, only the intermediate waters turn around the southern tip of Tasmania and flow west into the GAB. We find that the subsurface extension of the EAC supplies the TL and, ultimately, the Pacific-to-Indian link of the southern hemisphere supergyre.

These observations are the first direct measurements of the intermediate depth circulation

near Australia with adequate spatial resolution to resolve boundary currents and their recirculations, and sufficient temporal resolution to account for the seasonal cycle. The westward Eulerian transport south of Tasmania displays substantial variability, likely due to the presence of substantial eddy activity, between times of no leakage to maximum values of 14.5 Sv. We estimate the mean leakage of AAIW into the Indian Ocean to be 3.8 ± 1.3 Sv. Between 147 and 145° E the mean water transport increases to 5.0 ± 1.8 Sv because of the contribution from an anticyclonic gyre north of the ACC, and at 115° E the mean net westward transport is 5.2 ± 1.8 Sv.

Chapter 6

Conclusions and Future Work

6.1 Main conclusions

The velocity fields inferred from the trajectories of Argo floats have proven to be a valuable tool for observing the major ocean currents. The velocity fields can be used to examine statistical properties at regional and global scales, and to describe regional and global circulation patterns at temporal scales that range from months to years.

One initial achievement of the present work is the development of software that may be used to obtain velocity fields from Argo data, allowing a continuous update of the velocity data set and full control in the Argo data retrieval and selection procedure. This practical tool has then been used for several applications: to study the statistics of the velocity field, to examine the velocity fields at several depths in the equatorial Atlantic Ocean, and to quantify the transport of intermediate waters in the Tasman Leakage.

The first application has been the statistical study of ocean velocities, in particular the analysis of the Gaussian character of the velocity PDFs (chapter 3). The Argo-inferred velocities show to be adequate for this analysis as the inferred PDFs are comparable to previous results in the literature. Therefore, the very large amount of velocity data in the Argo data base shows to be highly valuable for these applications. We observe a deviation of the PDFs from Gaussianity, but yet we find no conclusive arguments to state that these PDFs are not Gaussian at a local scale. Our results emphasize the dependence of the resulting PDFs on the selection of both temporal and spatial sampling intervals which likely depend on the regional dynamics. In order to integrate relatively large temporal and spatial regions, a proper local normalization is previously required. This is a difficult process which, if incorrectly done, may lead to residual lateral and temporal inhomogeneities. We end up

developing a simple model that shows to be quite useful at reproducing the velocity PDFs.

The second application is an exhaustive study of the circulation of the equatorial Atlantic Ocean at several depths. It shows the great potential of the methodology, both to obtain the annual-mean ocean currents at several depths and to unveil the seasonal variations at the sea surface and 1000 dbar. In particular, we calculate monthly velocity fields which are quite different from the annual averaged fields.

We have examined the intricate coupling of the surface winds and the surface currents, sometimes in a direct fashion but often in an indirect manner. The intensity of the surface easterlies is associated to the annual latitudinal displacement of the ITCZ, in most of the Atlantic taking place between about 2°N and 10°N. As a result, at most latitudes the predominant forcing is annual but there is a latitudinal range where the semi-annual forcing may become important, e.g. at 25°W this occurs between 2 and 4°N. The surprise comes when we see that this semi-annaul patterns is visible at many latitudes, either as a result of the instability of the nSEC and its recirculation as the NECC, or as the meridional transport of westward cSEC momentum. The way the NECC grows in intensity across the Atlantic, from east to west, and the novel view of the NBC retroflection as the westernmost path for the recirculating nSEC, are two remarkable outputs.

The five jets that appear in the annual-mean velocity field at 1000 dbar are the result of the composition of three alternating jets that reverse through the year while changing their latitudinal position. We observe the EIC to reach an eastward maximum in January and a westward maximum in September. Two extra-equatorial jets, the NIEC and the SIEC, develop on both sides and flow opposite to the EIC. The peak velocities of the EIC do not coincide with the maximum extra-equatorial jets. The NIEC starts its westward development in January, when the EIC peaks (0.07 m s^{-1}), reaches the maximum around April (-0.04 m s^{-1}) and persists until July, before decaying. In August the eastward NIEC begins to develop and peaks in October; the eastward mode of the NIEC remains closer to South America and for a shorter period of time. The temporal evolution of the SIEC is analogous but

restricted in extension because of the presence of the American continent. We have shown that some of these inversions are likely the result of westward propagating waves.

The third, and final, application dealt with the surface and intermediate currents around Australia, both the annual-mean and seasonal cycle. The velocity data is complemented with the CTD data contained in the profiles and a novel method is developed to estimate the water transport in the intermediate layer. Our results confirm the existence of westward transport south of Tasmania and along the Great Australian Bight, from the Pacific Ocean to the Indian Ocean, through the Tasman Leakage. We obtain the first actual measurements of water transport, in rough agreement with previous model estimates: 3.8 ± 1.3 Sv with 39% contribution through eddy transport. We also show the existence of substantial mesoscale variability, from times of zero transport to a maximum value of 12.0 Sv. This represents a confirmation of the existence of the Southern Ocean Supergyre, previously suggested by models and hypothesized from oceanographic cruise data.

The dissertation is complemented with several Appendices. In appendix A we propose that ocean velocities have a Gaussian distribution which maximizes entropy. The maximization of entropy is the result of oceans dissipating energy input as fast as possible, tending to the homogenization of momentum and energy. Appendix B presents some thoughts on the scientific method, which arose during the investigation process. The collection of large amounts of data and their progressive analysis represents an approximation to science that differs from the classical hypothetico-deductive method. It does not aim at being a deep critical review but rather to rise and share some questions that transcend the scientific process itself. Finally, appendix C presents the basics of the harmonic analysis used in chapter 4.

6.2 Future research

The calculation of a global ocean velocity dataset opens the door to the study of many different ocean regions from a novel perspective. There are many regional oceans yet to be explored with the Argo-inferred velocities. Other research groups are developing similar

tools, venturing a great potential for the utilization of Argo-inferred velocity data. The future success of this tool, however, will largely depend on the continuous release of Argo floats. If the actual data acquisition rate is maintained (about 120.000 velocity vector per year), more consistent annual and seasonal maps will become available, with better temporal and spatial resolution, and the study of inter-anual changes will become a reality.

This dissertation has not included a number of relevant questions that arose throughout its preparation. We would like now to briefly comment on some aspects that might be developed in a future, complementing what is presented in this thesis. It does not aim at being a complete recollection of ideas but rather a reflection on some of the most interesting or promising issues.

The modification of the floats' communication technologies (substitution of Argos transmission by Iridium) may difficult the calculation of the surface velocities but will likely lead to a better estimation of the deep displacements, typically much harder to obtain. What improvement represents the Iridium transmission system in estimating of deep velocities? Is it possible to estimate the surface velocity from a short surface transmission time? What is the minimum surface time needed to estimate the surface velocity? Would it be worth to artificially increase the time at surface in order to be able to infer the surface ocean velocities from the surface positioning? All these questions need to be addressed if we wish to keep the Argo-inferred velocities as a valuable analyses tool.

The ANDRO 2013 dataset splits the surface displacement in two, doubling the available number of surface vectors. During the surface time, approximately 10 positions are transmitted, so many different pairs of vectors could be used (55 values for 10 positions). Do we have resolution enough to extract information from all the positions? Could we calculate all the possible combinations and study the statistics of the displacements at surface? Could we use this information to obtain information on the inertial and tidal oscillations, or even the Stokes drift? Park et al. (2004) proposed a method to correct for the inertial oscillations. Could the information contained in the surface positions improve the method? Work is yet to be done to assess the errors associated to positioning delays and horizontal displacements during vertical migra-

tion. EM-Apex floats (Sanford, 1978; Sanford et al., 2007), capable of estimating the shear velocity between consecutive layers, would lead to information of the complete velocity profile during the vertical migration that should allow correcting the associated drift. Because there are still very few EM-Apex floats, it is not a solution to be extensively implemented for all floats, but it should give a proper quantification of the error.

Exploring the PDFs of the velocity fields from the perspective of the maximum entropy concept is another pending task. We are aware it is not an easy task, as it involves "slippery" concepts. Nevertheless, we think that it could represent a new window for a better understanding of the distribution of properties in the ocean.

The Argo program is expected to continue in the future, therefore asking for improved techniques for calculating ocean velocities from the Argo positions and opening the possibility for many further applications, from global and regional descriptions to the analyses of ocean processes. We plan to continue our work in this direction. Our next objective, depending on funding availability, is to make the output velocity fields available in a user-friendly Internet environment. Any comment or suggestion is most welcome.

Appendices

A. Gaussian PDFs and Entropy

In chapter 3 we discussed the difficulties to arrive to conclusions about whether the ocean velocities are Gaussian or not. Here we attempt to explore, beyond the data itself, a possible explanation for the Gaussian (or quasi-Gaussian) behaviour of the velocities PDFs.

We found no attempt in the literature to provide for an explanation to the near Gaussian behaviour. One possibility, to be explored next, is that Gaussian PDFs are the distributions that give a higher entropy for a finite domain and a certain standard deviation (Conrad, 2004; Lyon, 2013). We do not pretend to prove it but rather to open a question to be explored in a future work. Quoting Lyon: "My goal is not to argue that maximum entropy (ME from now on) explanations are the correct explanations for why particular distributions are normal/log-normal/etc., or why normal distributions are common in nature. I only intend to point out that developing ME–explanations in detail may be a promising alternative explanatory strategy."

Entropy is a slippery concept (Lyon, 2013) and care must be taken when applying it. It is not totally appropriate to talk about the absolute entropy of a system, but rather of its entropy variation, or its entropy as compared to another system. The second principle of thermodynamics states that every natural system tends to naturally increase its entropy, releasing internal energy, which is often "degraded" as heat, as a way to tend towards a more stable equilibrium.

The ocean is a system forced by many external agents, mostly in the form of wind pulses and pressure gradients, which represent a continuous input of kinetic energy. All this energy enters the ocean non-homogeneously, generating anisotropic motions. The ocean reacts to homogenize these energy inputs: Two water parcels in contact tend to exchange properties until an equilibrium is achieved. Temperature, salinity, dissolved gases and nutrients, among others, are exchanged through diffusion, largely increased by turbulent flows. Momentum is also exchanged, with viscosity as the momentum diffusion, leading to the cascade of energy that ends with energy dissipation and degradation as heat. In this process the entropy of the system

increases, reaching a maximum when an equilibrium with the environment is achieved.

The distribution of the flow velocities should reflect the optimization in this process of energy distribution, i.e. a maximization in the rate of homogenization or the rate of gain of entropy. The ocean velocities are Gaussian because this is the way the gain of entropy and homogenization are maximized. If the energy entrances in the ocean would be locked, the Gaussian distribution of the velocities would give the shortest time for the ocean to be homogeneous.

The observed deviations from Gaussian behaviour may be caused by the spatial and temporal inhomohenities in the selected boxes (chapter 3) but it is also possible that they are caused by the continuous input from energetic events that bring the distributions away from those that would lead to an idealized energy (and entropy) transfer from one single energetic input.

The spatial scale at which lateral inhomogenities can be neglected depends on the local rate of the Earth's rotation; in particular, the rotation of the Earth gives rise to the possibility of self-sustained perturbations, such as eddies and filaments which interact laterally but barely mix together, something that does not happen in the absence of rotation. This is what allows the export of Mediterranean water as deep meddies or coastal organic matter as surface filaments generated at upwelling coastal zones. These structures, of different size depending on rotation and stratification, may display intense gradients with the surrounding waters, promoting the presence of strong and very localized lateral inhomogeneities. Further, this may change with depth, typically with an increase in the natural size of the deep structures, therefore leading to the observed increase in kurtosis.

We hypothesize that all coherent ocean structures are highly Gaussian at a local (meso or submeso) scale, and that the high kurtosis observed is due to the overlap in time, and the spacial inhomogenities.

B. Inductive Feedback

B.1 Beyond research

Being part of a long-term scientific research gives rise to some questions that are more related to the scientific process itself than to the actual research topic: How does knowledge in this topic advances? How do I formulate a hypothesis? How do I validate my results? Or, set in other terms, what is my scientific method? And does it agree with prevalent standards of scientific research?

These lines pretend to be a personal reflection on how I perceive my research process and how I understand the scientific method – or its absence –. They are motivated by my thinking on science and knowledge as transcending the mere achievement of results, being the materialization of human curiosity, the engine of human intelligence.

I do not pretend to carry on an exhaustive and rigorous study about the scientific method, but I will refer to different authors who accompanied me on this meta-research.

B.2 The scientific method

Karl Popper made very clear that we must distinct between the process of having an idea and the process of testing it (Popper, 1934, pages 8-9):

"...I shall distinguish very sharply between the process of conceiving an idea, and the methods and results of examining it logically."

"But the question is: what, precisely, do we want to reconstruct? If it is the process involved in the stimulation and release of an inspiration which are to be reconstructed, then I should refuse to take it as the task of the logic of knowledge. Such processes are the concern of empirical psychology, but hardly of logic. It is another matter if we want to reconstruct rationally the subsequent tests whereby the inspiration may be discovered to be a discovery, or become known to be knowledge."

"...there is no such thing as a logical method of having new ideas, or a logical reconstruction of this process... "

"...every discovery contains an *irrational element*, or a *creative intuition*."

"From a new idea, put up tentatively, and not yet justified in any way –an anticipation, a hypothesis, a theoretical system, or what you will- conclusions are drawn by means of logical deduction."

This clear difference, between the overcoming of an idea and the process of transforming it into knowledge, allows for the establishment of a rational structure of knowledge development. This is, the Hypothetico-Deductive scientific method. Keeping it simple, this method states that, after the intuitive creation process, an idea needs to be formulated in such a way that allows, not verifiability, but rather its falsifiability. This is called by Popper the demarcation criterion of falsifiability: "it must be possible for an empirical scientific system to be refuted by experience."

Once we have a formulation susceptible for testing we proceed with the empirical tests. If the tests contradict the hypothesis then we consider it as false, but if the experience agrees with our hypothesis then we can affirm that there is no reason (until experience shows the opposite) to not consider that our hypothesis is true.

Again, quoting Popper (1934, page 20): "According to my proposal, what characterizes the empirical method is its manner of exposing to falsification, in every conceivable way, the system to be tested. Its aim is not to save the lives of untenable systems but, on the contrary, to select the one which is by comparison the fittest, by exposing them all to the fiercest struggle of survival."

B.3 Automatic data collection: On the availability of non-target data

Despite the Hypothetico-Deductive method is applicable to some scientific research, where the creative process and the empirical testing go separately, I question that all scientific progress can be seen under this perspective.

The overcome of computers in all scientific fields has increased the amount of available data and has drastically changed the data acquisition process. At the time when Karl Popper wrote "The logic of scientific discovery", obtaining data to study certain phenomenon required a specific survey or experiment, aimed to obtain results for a particular topic. Remote sensing, computer simulations, data logs, among other, allow nowadays for the acquisition and storage of huge amounts of data. Sometimes, the data are stored just because there is the chance to do

so, and not for any particular experiment.

The data collection has become a human obsession, and every possible variable of piece of information susceptible of being analysed is now logged and processed. There are terabytes of all sort of data stored in hard disks and servers waiting for a researcher to milk them, including Internet navigation, the number of vehicles that use a particular road, the budget of a country or the stocks market, among a neverending list of issues. Almost everything nowadays is quantifiable, and this quantification is stored and often analysed.

How does this fact affect the scientific approach? What is its effect in the progres of knowledge and in the scientific methodology? We don't need any more to design an experiment to collect the data, we can just download it from internet and transform it into graphical material to be interpreted.

The present work is a clear example of this situation: the Argo floats were originally designed to monitor the temperature and salinity of the upper global ocean, and to introduce the data in weather forecast models. However, it was soon realized though the float positions could give valuable information about the ocean velocities if correctly processed. The studies here presented show the information extracted from the trajectory files of the Argo floats in order to obtain the ocean velocities, applied to two ocean regions: the equatorial Atlantic Ocean and the Tasman Leakage. Despite being true that the statistical study relates to the global dataset, it is also true that there is a lot of information in the Argo trajectory data to be explored and tested. There is a large amount of knowledge yet to be built.

This can be afforded in two ways. The Argo data can be used, on one hand, to test different previous theories about the ocean currents, processing the data in order to verify or falsify early hypothesis. On the other hand, the data may be plotted aimless, just to explore what the information stored in all these floats has to tell us. We can plot a map of zonal velocity of an ocean region unknown to us, and observe the graphical information, trying to comprehend what we see, on the basis of our previous knowledge. It is like carrying an experiment without a previous hypothesis, and asking ourselves what question could the data we are obtaining be the answer for.

We are not saying this is how science works,

neither it is how it should work. We are just mentioning the fact that nowadays we have the results of hundreds of thousands of experiments that have been aimless performed, and that the order of the steps of the scientific method proposed by Popper are somehow inverted.

Despite total ignorance will probably not be the case when approaching a new ocean region, or any dataset in general, it is true that we can, from a basic knowledge of a certain question, explore a related dataset in order to extract more information susceptible for being be latter contrasted with what others said before. This is the path to deepen in our knowledge, facing data against new perspectives, that should lead us to a better comprehension of phenomena, through the combination of intuition (which builds on previous knowledge) and the information extracted from data.

There is another question related to the need of verifying or falsifying a hypothesis: many questions in science are not about true or false, but rather about accurateness in the descriptions. Descriptive oceanography would be a good example, since we are not necessarily saying weather the existence of a current is true or false but rather describing the current, its mass, heat and salt transport, it effects on the global climate. So what method would apply in these cases?

These considerations about research and data analysis contrast with the hypothetico-deductive scientific method, in the sense that we do not always need a previous hypothesis to face a problem, and we can just say: "Let's see what I can get from these data!"

Paul Feyerabend, in his book "Against the Method" (Feyerabend, 1975) does a drastic allegation in favour of an anarchist science, deeply contrasting with the hypothetico-deductive method. Feyerabend goes far beyond a formal criticism of the adequateness of the hypothetico-deductive method, questioning also how rational criticism may lead to the loss of freedom, to a degeneration of the human essence. He presents the hypothetico-deductive method as the dehumanization of science, and quoting Kierkegaard, states: "Could it be possible that my activity as an objective (rationally criticist) nature observer weakens my strength as human being?"

Feyerabend's arguments also point to the fact that the scientific method does not respond for lots of the discoveries that have been made,

nor for many scientific approaches that brought knowledge beyond. Feyerabend does not defend pure inductivism in the terms Francis Bacon proposed it in 1620, pointing to the role of experience beyond the contrast of previous hypotheses, and makes relevant the role of observation in the formulations of newer (possibly partial) hypotheses, that will complement the actual knowledge once tested and verified (or not falsified).

B.4 Inductive feedback

To describe the scientific method used in my Argo-based research, I would not use the term hypothetico-deductive, nor inductive, neither counterinductive. There clearly is an initial hypothesis formulation, and a data contrast; but it often happens that the information extracted from the data modifies the hypothesis, bringing new perspectives, and so on, in a cycle that I would call inductive feedback.

Despite there usually is an underlying hypothesis in the data exploration, unexpected features or information may appear during the data exploration that may rise newer hypothesis, or modify the previously chosen ones. Again, the method proposed by Popper does not adequately describe the reconstruction of the "illustration" process.

Serendipity may often be invoked when lokking at previously unexplored data, aimless collected. But can it be considered serendipity? Or it is rather a part itself of the scientific method?

As Feyerabend defends, the hypothetico-deductive method could be desirable in terms of systematization of the knowledge acquisition process, but it does not usually describe the real steps followed to develop ongoing research. This is especially true when it comes to the knowledge acquired from the modern big databases. Furhter, the hypothesis formulation does not always correspond to Popper's method: sometimes the information extracted from the data affects the underlying hypothesis.

In modern science, it is rare that a specific research project brings to theoretical conclusive results. What usually happens is that a research project builds a piece of knowledge that is added to the state of the art. Successive projects build up a collective knowledge that may, in the future, lead to conlusive results about the inicial hypothesis.

Perhaps the need of a different method for reconstructing the scientific process will arise from a newer perspective of science itself. The knowledge system is not seen anymore as a scheme of systematic laws but rather as a huge wall of small knowledge bricks that has to be filled. Some bricks may go to a wrong place at the beginning, but the acquisition and processing of fresh data may help to solve previous blanks, and replace wrong bricks.

An approach to describe the research process when big database are involved could be:

1. Formulation of the initial hypothesis

The research starts from an idea, from previous knowledge to be complemented, or from an intuition.

2. Literature review

Popper itself expresses the importance of referring our research to the established knowledge.

3. Data analysis

We extract the information we need to test our hypothesis, and explore new perspectives.

4. Literature revision

We contrast the new information with the state of the art, and reformulate the initial hypothesis if necessary.

5. Data reanalysis

We go back to the data and process it under a different perspective to extract information. New questions may also arise in the comprehension process that will need complementary data. These last steps can be repeated as many times as needed to refine the answer we want to give to a certain question.

6. Formulation of the "brick of knowledge"

The final form of a research is a communication of the achieved progress to the scientific community. The "knowledge brick" so produced enters the "knowledge wall", and it will be criticized and complemented by future researches, that will produce their "knowledge building".

The inductive feedback method differs from the hypothetico-deductive in two main aspects. First, we may have an initial hypothesis, but we can also explore the data looking for unexpected patterns that may lead to a hypothesis to be tested. Second, the elaboration of a hypothesis and the transformation of previous knowledge are not two separate processes. During the data interpretation the hypothesis may be re-elaborated or changed, and this process may take place many times.

C. Harmonic Analysis

In order to help analyse the mean annual variations of the observed zonal velocity fields, an harmonical analysis of the canonical Eulerian time series is performed at each grid point (chapter 4). The mean fields and trends, as well as the annual and semi-annual components, are obtained through a classical linear least square adjustment procedure to a model such as

$$U_m(t) = U_0 + U_t(t - t_m) + U_a \cos(\frac{2\pi}{T_a}(t - t_a)) +$$

$$+U_s \cos(\frac{2\pi}{T_s}(t - t_s)) + R(t)$$

where t is the time expressed in month (t=1,2,...12), t_m is the center of the canonical time interval with value 6.5, T_a is the annual period with value 12, T_s is the semi-annual period with value 6, and R is the fitting residual. For each grid point, six parameters are obtained: U_0 is the time-independent contribution; U_t is the linear tendency in the time series; U_a and t_a are the amplitude and phase of the annual component; and U_s and t_s are the amplitude and phase of the semi-annual component. As defined, the phase t_a and t_s correspond to the time when maximum positive (eastward) contributions occur. The explained variance at each point is simply calculated as the variance associated to the corresponding contribution divided by the observed variance, calculated from the original time series $U_t - U_0$, and multiplied by 100. In order to avoid spurious contribution to the tendency, expected to be null for a canonical year, the adjustment is performed over N-repeatitions of the 12 points time series, here choosing N=5 for a total of 60 samples.

In order to investigate the impact of a non-perfectly sinusoidal annual contribution to the semi-annual component, a modified decomposition could be performed. In this case the semi-annual component is split in two parts, one locked in phase with the annual component and the other with independent phase. The in-phase component has an amplitude that is a fraction Q of the annual component amplitude, allowing the maximum (or minimum, depending on the Q sign) to be sharper and the minimum (or maximum) to be flattened. Setting $Q < 0.25$ prevents introduction of an

additional extreme. In a first step, a non-linear minimization procedure is carried out, where U_s is forced to 0 in order to get an approximate value for Q. Setting this Q value the minimization procedure is run in order to get all other parameters, including the modified semi-annual amplitude U_S. This procedure has been carried out in chapter 4, and the results have confirmed some of the ideas there proposed. The results, however, are not further discussed.

References

1. Arnault, S., 1987. Tropical Atlantic geostrophic currents and ship drifts. J. Geophys. Res. Ocean. 92, 5076–5088.

2. Boebel, O., Rossby, T., Lutjeharms, J., Zenk, W., Barron, C., 2003. Path and variability of the Agulhas Return Current. Deep Sea Res. II 50, 35–56.

3. Bourlès, B., Andrié, C., Gouriou, Y., Eldin, G., du Penhoat, Y., Freudenthal, S., Dewitte, B., Gallois, F., Chuchla, R., Baurand, F., Aman, A., Kouadio, G., 2003. The deep currents in the Eastern equatorial Atlantic Ocean. Geophys. Res. Lett. 30, 8002.

4. Bourlès, B., Gouriou, Y., Chuchla, R., 1999. On the circulation in the upper layer of the western equatorial Atlantic. J. Geophys. Res. 104, 21151–21170.

5. Bracco, A., LaCasce, J.H., Provenzale, A., 2000. Velocity probability density functions for oceanic floats. J. Phys. Oceanogr. 30, 461–474.

6. Brandt, P., Caniaux, G., Bourlès, B., Lazar, A., Dengler, M., Funk, A., Hormann, V., Giordani, H., Marin, F., 2011. Equatorial upper-ocean dynamics and their interaction with the West African monsoon. Atmos. Sci. Lett. 12, 24–30.

7. Brandt, P., Eden, C., 2005. Annual cycle and interannual variability of the mid-depth tropical Atlantic Ocean. Deep. Res. I 52, 199–219.

8. Brandt, P., Schott, F.A., Provost, C., Kartavtseff, A., Hormann, V., Bourlès, B., Fischer, J., 2006. Circulation in the central equatorial Atlantic: Mean and intraseasonal to seasonal

variability. Geophys. Res. Lett. 33, L07609.

9. Broecker, W.S., 1991. The Great Ocean Conveyor. Oceanography 4, 79–89.

10. Bunge, L., Provost, C., Hua, B.L., Kartavtseff, A., 2008. Variability at intermediate depths at the Equator in the Atlantic Ocean in 2000–06: Annual cycle, Equatorial Deep Jets, and intraseasonal meridional velocity vluctuations. J. Phys. Oceanogr. 38, 1794–1806.

11. Bunge, L., Provost, C., Lilly, J.M., D'Orgeville, M., Kartavtseff, A., Melice, J.-L., 2006. Variability of the horizontal velocity structure in the upper 1600 m of the water column on the equator at 10°W 1287–1304.

12. Carton, J.A., Katz, E.J., 1990. Estimates of the zonal slope and seasonal transport of the Atlantic North Equatorial Countercurrent. J. Geophys. Res. 95, 3091–3100.

13. Castellanos, P., Pelegrí, J.L., Campos, E.D., Rosell-Fieschi, M., Gasser, M., 2014. Response of the surface tropical Atlantic Ocean to wind forcing. Submitted to Progr. Oceanogr.

14. Chu, P.C., Ivanov, L.M., Melnichenko, O. V., Wells, N.C., 2007. On long baroclinic Rossby waves in the tropical North Atlantic observed from profiling floats. J. Geophys. Res. 112, C05032.

15. Conrad, K., 2004. Probability distributions and maximum entropy. Entropy 6, 1–27.

16. Davis, R.E., 1998. Preliminary results from directly measuring middepth circulation in the tropical and South Pacific. J. Anim. Ecol. 103, 24619–24639.

17. Davis, R.E., 2005. Intermediate-depth circulation of the Indian and South Pacific Oceans measured by autonomous floats. J. Phys. Oceanogr. 35, 683–707.

18. DeCarlo, L.T., 1997. On the meaning and use of kurtosis. Psychol. Methods 2, 292–307.

19. Didden, N., Schott, F., 1992. Seasonal variations in the western tropical Atlantic: Surface circulation from Geosat altimetry and WOCE model results. J. Geophys. Res. 97, 3529–3541.

20. Dong, S., Sprintall, J., Gille, S.T., Talley, L., 2008. Southern Ocean mixed-layer depth from Argo float profiles. J. Geophys. Res. 113, C06013.

21. Eriksen, C.C., 1981. Deep Currents and Their Interpretation as equatorial Waves in the Western Pacific Ocean. J. Phys. Oceanogr. 11, 48–70.

22. Eriksen, C.C., 1982. Equatorial wave vertical modes observed in a Western Pacific island array. J. Phys. Oceanogr. 12, 1206–1227.

23. Feyerabend, P. K., 1975. Against the method: An outline of an anarchistic theory of perception. NLB, London.

24. Firing, E., Wijffels, S.E., Hacker, P., 1998. Equatorial subthermocline currents across the Pacific. J. Geophys. Res. 103, 21413–21423.

25. Flagg C. N., Gordon R. L., McDowell S., 1986. Hydrographic and current observations on the continental slope and shelf of the western equatorial Atlantic. Journal of Physical Oceanography 16, 1412-1429.

26. Fratantoni, D.M., Richardson, P.L., 1999. SOFAR Float observations of an intermediate-depth eastern boundary current and mesoscale variability in the eastern tropical Atlantic Ocean. J. Phys. Oceanogr. 29, 1265–1278.

27. Ganachaud, A., Gourdeau, L., Kessler, W., 2008. Bifurcation of the Subtropical South Equatorial Current against New Caledonia in December 2004 from a hydrographic inverse

box model. J. Phys. Oceanogr. 38, 2072–2084.

28. Garzoli, S.L., Katz, E.J., Panitz, H.J., Speth, P., 1982. In situ wind measurements in the equatorial Atlantic during 1979. Oceanol. Acta 5, 281–288.

29. Gille, S.T., Llewellyn Smith, S.G., 2000. Velocity probability density functions from altimetry. J. Phys. Oceanogr. 30, 125–136.

30. Godfrey, J.S., 1989. A sverdrup model of the depth-integrated flow for the world ocean allowing for island circulations. Geophys. Astrophys. Fluid Dyn. 45, 89–112.

31. Gordon, A.L., 1985. Indian-Atlantic transfer of thermocline water at the Agulhas Retroflection. Science 227, 1030–1033.

32. Gouriou, Y., Andrié, C., Bourlès, B., Freudenthal, S., Arnault, S., Aman, A., Eldin, G., du Penhoat, Y., Baurand, F., Gallois, F., Chuchla, R., 2001. Deep circulation in the equatorial Atlantic Ocean. Geophys. Res. Lett. 28, 819–822.

33. Gouriou, Y., Bourlès, B., Mercier, H., Chuchla, R., 1999. Deep Jets in the equatorial Atlantic Ocean. J. Geophys. Res. 104, 21217–21226.

34. Gouriou, Y., Reverdin, G., 1992. Isopycnal and diapycnal circulation of the upper equatorial Atlantic Ocean in 1983–1984. J. Geophys. Res. 97, 3543.

35. Gulev, S. K., Grigorieva, V., Ster, A., 2011. Global atlas of ocean waves based on VOS. Available at http://www.sail.msk.ru/atlas/.

36. Hasternath, S., Lamb, P., 1977. Some aspects of the circulation and climate over the eastern equatorial Atlantic. Mon. Weather Rev. 105, 1019–1023.

37. Hayes, S.P., Milburn, H.B., 1980. On the vertical structure of velocity in the eastern equatorial Pacific. J. Phys. Oceanogr. 10, 633–635.

38. Herraiz-Borreguero, L., Rintoul, S.R., 2011. Regional circulation and its impact on upper ocean variability south of Tasmania. Deep Sea Res. II 58, 2071–2081.

39. Hormann, V., Lumpkin, R., Foltz, G.R., 2012. Interannual North Equatorial Countercurrent variability and its relation to tropical Atlantic climate modes. J. Geophys. Res. 117, C04035.

40. Hüttl-Kabus, S., Böning, C.W., 2008. Pathways and variability of the off-equatorial undercurrents in the Atlantic Ocean. J. Geophys. Res. 113, 1–14.

41. Jordi, I.-F., Garcia-Ladona, E., Font, J., García-Olivares, A., 2006. Non-Gaussian velocity probability density functions : An altimetric perspective of the Mediterranean Sea. J. Phys. Oceanogr. 36, 2153–2164.

42. Lankhorst, M., Fratantoni, D., Ollitrault, M., Richardson, P., Send, U., Zenk, W., 2009. The mid-depth circulation of the northwestern tropical Atlantic observed by floats. Deep Sea Res. I 56, 1615–1632.

43. Lebedev, K. V, Yoshinari, H., Maximenko, N.A., Hacker, P.W., 2007. YoMaHa'05: Velocity data derived from trajectories of Argo floats. IPRC Technical Note No. 4 (2). June 12, 2007.

44. Lilly, D.K., 1969. Numerical simulation of developing and decaying two-dimensional turbulence. J. Fluid Mech. 45 II, 395-415.

45. Llewellyn Smith, S.G., Gille, S.T., 1998. probability density functions of large-scale turbulence in the ocean. Phys. Rev. Lett. 81, 5249–5252.

46. Lumpkin, R., Garzoli, S.L., 2005. Near-surface circulation in the tropical Atlantic Ocean. Deap Sea Res. 52, 495–518.

47. Lumpkin, R., Speer, K., 2007. Global Ocean Meridional Overturning. J. Phys. Oceanogr. 37, 2550–2562.

48. Luyten, J. R., Swallow, J.C., 1976. Equatorial Undercurrents. Deap Sea Res. 23, 999–1001.

49. Lyon, A., 2013. Why are normal distributions Normal? Br. J. Philos. Sci. 1–25.

50. Machín, F., Pelegrí, J.L., 2009. Northward penetration of Antarctic Intermediate Water off Northwest Africa. J. Phys. Oceanogr. 512–535.

51. Merle, J., Arnault, S., 1985. Seasonal variability of the surface dynamic topography in the tropical Atlantic Ocean. J. Mar. Res. 43, 267–288.

52. Middleton, J.F., Cirano, M., 2002. A northern boundary current along Australia's southern shelves: The Flinders Current. J. Geophys. Res. 107, 3129.

53. Molinari, R.L., Garzoli, S.L., Katz, J., Harrison, E., Richardson, P.L., 1986. A synthesis of the first GARP global experiment (FGGE) in the equatorial Atlantic Ocean. Prog. Oceanogr. 16, 91–112.

54. Morrow, R., 2004. Divergent pathways of cyclonic and anti-cyclonic ocean eddies. Geophys. Res. Lett. 31, L24311.

55. Niiler, P.P., Davis, R.E., J., W.H., 1987. Water-following characteristics of a mixed layer drift. Deap-Sea Res. 34, 1867–1881.

56. Ollitrault, M., Lankhorst, M., Fratantoni, D., Richardson, P., Zenk, W., 2006. Zonal intermediate currents in the equatorial Atlantic Ocean zonal intermediate currents in the equatorial Atlantic Ocean. Geophys. Res. Lett. 33, L05605.

57. Ollitrault, M., Rannou, J.-P., 2013. ANDRO: An Argo-based deep displacement dataset. J. Atmos. Ocean. Technol. 30, 759–788.

58. Park, J.J., Kim, K., King, B.A., Riser, S.C., 2005. An advanced method to estimate deep currents from profiling floats. J. Atmos. Ocean. Technol. 22.

59. Philander, S.G.H., Pacanowski, R.C., 1986. A model of the seasonal cycle in the tropical Atlantic Ocean. J. Geophys. Res. 91, 14192.

60. Polonsky, A.B., Artamonov, Y. V., 1997. North Equatorial Counter Current in the tropical Atlantic: Multi- jet structure and seasonal variability. Dtsch. Hydrogr. Zeitschrift 49, 477–495.

61. Ponte, R.M., Luyten, J., Richardson, P.L., 1990. Equatorial Deep Jets in the Atlantic Ocean. Deap Sea Res. 37, 711–713.

62. Popper, K., 1934. The logic of scientific discovery. Routledge (2005).

63. Rahmstorf, S., 2002. Ocean circulation and climate during the past 120,000 years. Nature 419, 207–14.

64. Rascle, N., Ardhuin, F., 2009. Drift and mixing under the ocean surface revisited: Stratified conditions and model-data comparisons. J. Geophys. Res. 114, C02016.

65. Rascle, N., Ardhuin, F., Terray, E. a., 2006. Drift and mixing under the ocean surface: A coherent one-dimensional description with application to unstratified conditions. J. Geophys.

Res. 111, C03016.

66. Richardson, P., Arnault, S., Garzoli, S., Bruce, J. G., 1992. Annual cycle of the Atlantic North Equatorial Countercurrent. Deep Sea Research I 39, 997–1014.

67. Richardson, P.L., 2008. On the history of Meridional Overturning Circulation schematic diagrams. Prog. Oceanogr. 76, 466–486.

68. Richardson, P.L., Lutjeharms, J.R.E., Boebel, O., 2003. Introduction to the Inter-ocean exchange around southern Africa. Deep Sea. 50, 1–12.

69. Richardson, P.L., McKee, T.K., 1984. Average seasonal variation of the Atlantic equatorial Currents from historical ship drifts. J. Phys. Oceanogr. 14, 1226–1238.

70. Richardson, P.L., Reverdin, G., 1987. Seasonal cycle of velocity in the Atlantic North Equatorial Countercurrent as measured by surface drifters, current meters, and ship drifts. J. Geophys. Res. Ocean. 92, 3691–3708.

71. Richardson, P.L., Schmitz, W.J., 1993. Deep cross-equatorial flow in the Atlantic measured with SOFAR floats. J. Geophys. Res. Ocean. 98, 8371–8387.

72. Richardson, P.L., Walsh, D., 1986. Mapping climatological seasonal variations of surface currents in the rropical Atlantic using ship drifts. J. Geophys. Res. 91, 10,537–10,550.

73. Ridgway, K., Dunn, J.R., 2003. Mesoscale structure of the mean East Australian Current System and its relationship with topography. Prog. Oceanogr. 56, 189–222.

74. Ridgway, K.R., 2007. Seasonal circulation around Tasmania: An interface between eastern and western boundary dynamics. J. Geophys. Res. 112, C10016.

75. Ridgway, K.R., Condie, S.A., 2004. The 5500-km-long boundary flow off western and southern Australia. J. Geophys. Res. 109, C04017

76. Ridgway, K.R., Dunn, J.R., 2007. Observational evidence for a Southern Hemisphere oceanic supergyre. Geophys. Res. Lett. 34, L13612.

77. Ridgway, K.R., Godfrey, J.S., 1997. Seasonal cycle of the East Australian Current. J. Geophys. Res. 102, 22921–22936.

78. Rintoul, S., Bullister, J., 1999. A late winter hydrographic section from Tasmania to Antarctica. Deep Sea Res. Part I Oceanogr. Res. Pap. 46, 1417–1454.

79. Rintoul, S.R., 1991. South Atlantic interbasin exchange. J. Geophys. Res. 96, 2675–2692.

80. Rintoul, S., Sokolov, S., 2001. Baroclinic transport variability of the Antarctic Circumpolar Current south of Australia (WOCE repeat section SR3). J. Geophys. Res. 106, 2815–2832.

81. Roemmich, D., Gilson, J., 2009. The 2004–2008 mean and annual cycle of temperature, salinity, and steric height in the global ocean from the Argo Program. Prog. Oceanogr. 82, 81–100.

82. Rosell-Fieschi, M., Rintoul, S.R., Gourrion, J., Pelegrí, J.L., 2013. Tasman Leakage of intermediate waters as inferred from Argo floats. Geophys. Res. Lett. 40, 5456–5460.

83. Sanford, T.B., Drever, R.G., Dunlap, J., 1978. Instruments and methods: A velocity profiler based on the principles of geomagnetic induction. Deap Sea Res. 25, 183–210.

84. Sanford, T.B., Price, J.F., Girton, J.B., Webb, D.C., 2007. Highly resolved observations and simulations of the ocean response to a hurricane. Geophys. Res. Lett. 34, L13604.

85. Schmid, C., Garraffo, Z., Johns, E., Garzoli, S.L., 2003. Pathways and variability at intermediate depths in the tropical Atlantic. Interhemispheric water Exch. Atl. Ocean 68, 233–268.

86. Schmid, C., Molinari, R.L., Garzoli, S.L., 2001. New observations of the intermediate depth circulation in the tropical Atlantic. Deep. Res. 59, 281–312.

87. Schmitz, W.J., 1995. On the interbasin-scale thermohaline circulation. Rev. Geophys. 33, 151–173.

88. Schott, F.A., Brandt, P., Hamann, M., 2002. On the boundary flow off Brazil at 5 – 10 ° S and its connection to the interior tropical Atlantic. Geophys. Res. Lett. 29, 1840.

89. Schott, F.A., Dengler, M., Brandt, P., Affler, K., Fischer, J., Bourlès, B., Gouriou, Y., Molinari, R.L., Rhein, M., 2003. The zonal currents and transports at 35°W in the tropical Atlantic. Geophys. Res. Lett. 30, 1349.

90. Schott, F. A., Fischer, J., Stramma, L., 1998. Transports and pathways of the upper-layer circulation in the western tropical Atlantic. Journal of Physical Oceanography 28, 1904-1928.

91. Send, U., Eden, C., Schott, F., 2002. Atlantic Equatorial Deep Jets : space – time structure and cross-equatorial fluxes. J. Phys. Oceanogr. 32, 891–902.

92. Sloyan, B., Rintoul, S., 2001. The southern ocean limb of the Global Deep Overturning Circulation. J. Phys. Oceanogr. 31, 143–173.

93. Sokolov, S., Rintoul, S., 2000. Circulation and water masses of the southwest Pacific : WOCE section P11 , Papua New Guinea to Tasmania. J. Mar. Res. 58, 223–268.

94. Souza, J.M. a. C., de Boyer Montégut, C., Cabanes, C., Klein, P., 2011. Estimation of the Agulhas ring impacts on meridional heat fluxes and transport using ARGO floats and satellite

data. Geophys. Res. Lett. 38, L21602.

95. Speich, S., Blanke, B., 2001. Warm and cold water routes of an O.G.C.M. thermohaline Conveyor Belt. Geophys. Res. Lett. 28, 311–314.

96. Speich, S., Blanke, B., Cai, W., 2007. The Global Ocean Conveyor Belt and the Southern Hemisphere Supergyre. Geophys. Res. Lett. 34, L23614.

97. Speich, S., Blanke, B., Vries, P. De, Drijfhout, S., Ganachaud, A., Marsh, R., 2002. Tasman leakage : A new route in the global ocean conveyor belt. Geophys. Res. Lett. 29, 1–4.

98. Stammer, D., 1997. Global characteristics of ocean variability estimated from regional TOPEX / POSEIDON altimeter measurements. J. Phys. Oceanogr. 27, 1743–1769.

99. Stramma, L., Fischer, J., Reppin, J., 1995. The North Brazil Undercurrent. Deep Sea Research I 42, 773-795.

100. Stramma, L., Schott, F., 1999. The mean flow field of the tropical Atlantic Ocean. Atlantic 46, 279–303.

101. Swenson, M.S., Pearn, P.N., 1996. Statistical analysis of the surface circulation of the California Current. J. Geophys. Res. 101, 22,631–22,645.
Talley, L D. 1996. Antarctic Intermediate Water in the South Atlantic. In "The South Atlantic: present and past circulation", G. Wefer, W. H. Berger, G. Siedler, D. Webb, Eds., p. 219-238, Berlin, Springer.

102. Talley, L.D., 2013. Closure of the Global Overturning Circulation through the Indian, Pacific and Southern Oceans: schematics and transports. Oceanography 26, 80–97.

103. Taylor, J.R., 1997. An introduction to error analysis (The study of uncertainties in physical measurements), 2nd ed. Univ. Sci. Books, Sausalito, Calif.

104. Thierry, V., Treguier, A., 2004. Numerical study of the annual and semi-annual fluctuations in the deep equatorial Atlantic Ocean. Ocean Model. 6, 1–30.

105. Tsuchiya, M., 1986. Thermostads and circulation in the upper layer of the Atlantic Ocean. Prog. Oceanogr. 16, 235–267.

106. Urbano, D.F., De Almeida, R. a. F., Nobre, P., 2008. Equatorial Undercurrent and North Equatorial Countercurrent at 38°W: A new perspective from direct velocity data. J. Geophys. Res. 113, C04041.

107. Urbano, D.F., Jochum, M., da Silveira, I.C., 2006. Rediscovering the second core of the Atlantic NECC. Ocean Model. 12, 1–15.

108. Van Sebille, E., England, M.H., Zika, J.D., Sloyan, B.M., 2012. Tasman leakage in a fine-resolution ocean model. Geophys. Res. Lett. 39, L06601.

Aknowledgments

The task that Josep Lluís Pelegrí has performed throughout my years as a PhD student has overcome by far the mere advisor role. His patience and comprehension have been essential in some critical moments. Josep Lluís has been an academic guide, but also a living example, a support; he always found the way to encourage me, and to push me beyond some tipping points. I was given the freedom to explore side roads in the data that brought nowhere but helped to understand the overall process. I was given the chance (and the responsibility) of taking my own decisions, making my learning process stronger. Thanks for these marvellous years.

When I arrived to the Institut de Ciències del Mar, I was thrown in a small office, where I met Jerôme. Without having anything to do with me, Jerôme introduced me in MatLab and the Argo velocities world. Step by step, he became a reference for programming and statistical consulting. Finally, he became a key piece in the puzzle, being involved in all the data process. His precision and exigence have risen the quality of the work I was doing, and his comments and suggestions made it more consistent and robust. It is been a pleasure to work with you Jerôme, and to discover that we both like MatLabbing at night!

Studying at Hobart for 4 months was awesome, and the trip to Antarctica was an exceptional occasion that I shall never forget. Steve Rintoul opened his doors for me, and guided me through the exploration of the currents around Australia. Together we developed the transport calculation method and its error estimation that allowed the study of the Tasman Leakage and the confirmation of the existence of the Southern Ocean Supergyre. Doing all this on board of the Aurora Australis, surrounded by ice, was a dream come true.

My dad, without being a scientist, is accounted responsible for my obstinacy and perseverance -sometimes not enough for him though- that have played a key role in going forward in tough moments. I would also like to thank him for making me aware from an early age that there are answers that science may not be able to give, and questions that might not need an answer.

Mum has often been the mirror for the philo-

sophical questions, and the person with whom understand the human process complementary to the research itself. I had the chance to doubt if what I was doing was what I wanted to do, finding in the doubt the strength to finish what I started with emotion, developed with passion, and finished with tenacity.

Nonno was probably at the origin, when cycling in the cold winter at dusk meant to talk about the distance to the moon, the age of the Universe, or how much water does a bathtub carry. He revealed science to be the playground of my childhood curiosity, and an aim to be achieved in an adult future.

Then there is a lot of people that has participated and sometimes suffered my PhD. I would like to remember all the late night conversations about floats, currents and climate change, all those mates who I met on board the different cruises that brought me around the world exploring the ocean currents, the days at land when the work stays on board, the good friends that the ocean brought to me. I also want to mention my house mates, who have been a testimony and a company during the late nights of coffee and MatLab, and those who shared with me the good and the evil of being a PhD student.

Funding for this work comes from the Spanish Ministerio de Ciencia e Innovación through project “Tipping Corners in the Meridional Overturning Circulation” (TIC-MOC, reference CTM2011-28867), and ”Memòria Oceànica del Clima” (MOC2, reference CTM2008-06438. Miquel Rosell-Fieschi would also like to acknowledge the Ministerio de Ciencia e Innovación for funding through a FPU grant.

Autobiographical Statement

My first memories related to science are cycling with my grandfather. I could not tell the exact age, probably many bike tours are overlapped in my memory forming a whole continuous line time where I grow as the scientific discussions get more complex. How far is the moon? What is the rain? How much water does a bathtub fit? What is the energy? Or how do the matter organize? What is radioactivity? Do you get wetter in a motorbike if you ride faster? The world was offered to me as an exploration field to be quantified and understood. The underlying scientific laws were a game to better understand what i could see.

My mum says that she only deliberately lied once to me: I must have been 4 or 5 years old when I asked my grandfather if we all would die. As a man of science, he gave the correct answer, and I ran to my mum crying, asking if that was true, and if she would ever die. I could not stand the idea of my mum being mortal, so she lied to me. I discovered at an early age that scientific answers are not always a source of joy, nor of peace. My mother has always been my strongest moral support, and a mirror that reflected an image of myself that helped me to grow and deal with myself.

SPURS cruise, Sarmiento de Gamboa, March 2013

The idea of a world that could be understood by numbers and equations, the perception of the power of comprehension, made me have a clear goal: I wanted to be a researcher! So I tried hard all my life to get here where I am.

Dad was not much at home when I was a kid, so the possibility of a connection and an exchange appeared only when being with each-

other was more about the quality than about the quantity of the time spent together. Before going to university I felt lost, because the answers that I were finding in science did not match the questions rising in my inside. Last two years at college I had a terrible Biology professor, and an even worse Math teacher (and we all know that the interest for a particular subject is more related to how is taught than to the subject itself). Fortunately, my Philosophy professor was one of the greatest instructors I had in my years at school. I did my final essay on history of science, and discovered the kind of answers given by Philosophy, less precise, less concrete, but often more useful when the questions are more related to oneself.

I remember a night when my mother was not home for dinner, so my father took me out. I can't really remember the development of the conversation, but the fact is that after that supper I decided not to study science at University, but to ingress the Philosophy faculty. I would never had expect that my dad, usually a strict person, always worried about my professional future, would push me into studying Philosophy. It was the best decision I could have taken.

I only followed one year of Philosophy courses, then changed into the Physics faculty and, after two years, again into Oceanography. Yes, I went back to Science, but I had the chance to approach another way of answering questions that often turned really useful when considering scientific problems.

It was my grandfather again who throw me in the ocean to swim at every possible occasion. It did not matter what was the weather: cold or hot, raining or sun shining, it was always good weather for a swim! Nowadays, after graduating in Oceanography at the Universidad de Las Palmas de Gran Canaria in 2008, and followed the joint masters program in Marine Sciences by the Universitat de Barcelona and the Universitat Politècnica de Catalunya, I present my Thesis. It has been a long process that constitutes my formation as a researcher, but that has also made me grow through discovery. Science has been the playground of my curiosity for the last five years, and here I present the results.

I hope the reader will find the content of my Thesis to be interesting, and enjoy the knowledge presented as much as I enjoyed studying the Ocean Currents.

It is now time to turn off the computer, and watch the ocean beyond the screen.

Published works

Talone, M., Meloni, M., Pelegrí, J. L., Rosell-Fieschi, M., Flobergaghen, R., 2014. Geoids evolution in the recent years and its impact on Oceanography. Scientia Marina, in press.

Rosell-Fieschi, M., Rintoul, S.R., Gourrion, J., Pelegrí, J.L., 2013. Tasman Leakage of intermediate waters as inferred from Argo floats. Geophys. Res. Lett. 40, 5456–5460.

Castellanos, P., Pelegrí, J. L., Campos, E. D., Rosell-Fieschi, M., Gasser, M., 2014. Response of the surface tropical Atlantic Ocean to wind forcing. Submitted to Progress in Oceanography.

Rosell-Fieschi, M., Pelegrí, J.L., Gourrion, J., 2013. Zonal Jets in the equatorial Atlantic Ocean. Submitted to Progress in Oceanography.

Rosell-Fieschi, M., Gourrion, J., Pelegrí, J.L., 2013. Ocean velocities PDFs from Argo's inferred velocities. Submitted to Ocean Modelling.

Contact: miquel.rofi@gmail.com